Copyright Warning & Restrictions

The copyright law of the United States (Title 17, United States Code) governs the making of photocopies or other reproductions of copyrighted material.

Under certain conditions specified in the law, libraries and archives are authorized to furnish a photocopy or other reproduction. One of these specified conditions is that the photocopy or reproduction is not to be "used for any purpose other than private study, scholarship, or research." If a, user makes a request for, or later uses, a photocopy or reproduction for purposes in excess of "fair use" that user may be liable for copyright infringement,

This institution reserves the right to refuse to accept a copying order if, in its judgment, fulfillment of the order would involve violation of copyright law.

Please Note: The author retains the copyright while the New Jersey Institute of Technology reserves the right to distribute this thesis or dissertation

Printing note: If you do not wish to print this page, then select "Pages from: first page # to: last page #" on the print dialog screen

NJIT New Jersey's Science & Technology University

The Van Houten library has removed some of the personal information and all signatures from the approval page and biographical sketches of theses and dissertations in order to protect the identity of NJIT graduates and faculty.

ABSTRACT

INTERACTIONS OF AMYLOID PEPTIDES WITH LIPID MEMBRANES

by
Yanxing Yang

The aggregation of amyloid proteins into fibrils is a hallmark of several diseases including Alzheimer's (AD), Parkinson's, and Type II diabetes. This aggregation process involves the formation of small size oligomers preceding the formation of insoluble fibrils. Recent studies have shown that these oligomers are more likely to be responsible for cell toxicity than fibrils. A possible mechanism of toxicity involves the interaction of oligomers with the cell membrane compromising its integrity. In particular, oligomers may form pore-like structures in the cell membrane affecting its permeability or they may induce lipid loss via a detergent-like effect. This dissertation aims to provide insights into these mechanisms of toxicity, which are poorly understood at the atomic level.

This dissertation kicks off with a molecular dynamics study of the interaction of individual amyloid-like peptides with lipid bilayers. It is found that both electrostatic and hydrophobic interactions contribute to peptide-membrane binding. In particular, the attraction of peptide to lipid bilayer is dominated by electrostatic interactions and hydrophobicity drives the burial of non-polar side chains into the interior of the bilayer. By changing the peptide sequence, positive net charges are shown to significantly strengthen peptide-membrane binding, whereas negative charges reduce their affinity drastically. Moreover, peptide-membrane binding can also be regulated by the position of positive residues in the peptide sequence which alters the exposure of positive side chains to the solvent. These results provide insights into the mechanism accounting for cell toxicity of amyloid proteins and the designing of antimicrobial peptides.

In this study, the first all-atom simulations are performed in which membrane-bound amphipathic peptides self-assemble into β-sheets that subsequently either form stable pores inside the bilayer or drag lipids out of the membrane surface. An analysis of these simulations shows that the acyl tails of lipids interact strongly with non-polar side chains of peptides deposited on the membrane. These strong interactions enable lipids to be dragged out of the bilayer by oligomeric structures accounting for detergent-like damage. Moreover, they disturb the orientation of lipid tails that are close to peptides. These distortions in lipid orientation are reduced close to pores contributing to stabilize these structures. These simulations also show that naturally twisted β-sheets are intermediate structures on pathway to poration. They enable water to partially penetrate the membrane triggering β-sheets to tilt and penetrate the membrane. The latter reduces interactions of solvent molecules with non-polar moieties of lipids. In addition, our simulations show that fibril-like structures produce little damage to lipid membranes as non-polar side chains in these structures are unavailable to interact with the acyl tail of lipids.

INTERACTIONS OF AMYLOID PEPTIDES WITH LIPID MEMBRANES

by
Yanxing Yang

A Dissertation
Submitted to the Faculty of
New Jersey Institute of Technology and
Rutgers, The State University of New Jersey – Newark
in Partial Fulfillment of the Requirements for the Degree of
Doctor of Philosophy in Applied Physics

Department of Physics

December 2022

Copyright © 2022 by Yanxing Yang
ALL RIGHTS RESERVED

APPROVAL PAGE

INTERACTIONS OF AMYLOID PEPTIDES WITH LIPID MEMBRANES

Yanxing Yang

Dr. Cristiano L. Dias, Dissertation Advisor — Date
Associate Professor of Physics, NJIT

Dr. Tao Zhou, Committee Member — Date
Associate Professor of Physics, NJIT

Dr. Hao Chen, Committee Member — Date
Professor of Chemistry and Environmental Science, NJIT

Dr. Ian Gatley, Committee Member — Date
Distinguished Professor of Physics, NJIT

Dr. Andres Jerez, Committee Member — Date
Senior University Lecturer of Physics, NJIT

Dr. Yong-Ick Kim, Committee Member — Date
Assistant Professor of Chemistry and Environmental Science, NJIT

Dr. Mikko P. Haataja, Committee Member — Date
Professor of Mechanical and Aerospace Engineering, Princeton University

BIOGRAPHICAL SKETCH

Author: Yanxing Yang

Degree: Doctor of Philosophy

Date: December 2022

Undergraduate and Graduate Education:

- Doctor of Philosophy in Applied Physics
  New Jersey Institute of Technology, Newark, NJ, 2022
- Doctor of Science in Condensed Matter Physics,
  Wuhan University, Wuhan, China, 2015
- Bachelor of Science in Physics,
  Wuhan University, Wuhan, China, 2009

Major: Applied Physics

Presentations and Publications:

Y. Yang, S. Jalali, and C. L. Dias. Effects of sequence mutation on binding of peptides to zwitterionic lipid bilayer. *The Journal of Physical Chemistry B*, 2022 (Submitted).

Y. Yang, H. Distaffen, S. Jalali, A. J. Nieuwkoop, B. L. Nilsson, and C. L. Dias. Atomic insights into amyloid-induced membrane damage. *ACS Chemical Neuroscience*, 13(18):2766–2777, 2022.

S. Jalali, Y. Yang, F. Mahmoudinobara, S. M. Singh, B. L. Nilsson, and C. L. Dias. Using all-atom simulations in explicit solvent to study aggregation of amphipathic peptides into amyloid-like fibrils. *Journal of Molecular Liquids*, 347:118283, 2022.

Y. Yang, S. Jalali, B L. Nilsson, and C. L. Dias. Binding mechanisms of amyloid-like peptides of lipid bilayers and effects of divalent cations. *ACS Chemical Neuroscience*, 12(11):2027-2035, 2021.

C. L. Dias, S. Jalali, Y. Yang, and L. Cruz. Role of cholesterol on binding of amyloid fibrils to lipid bilayers. *The Journal of Physical Chemistry B*, 124(15):3036-3042, 2020.

Y. Yang, American Physical Society (APS) March Meeting, Chicago, IL, 2022 (Oral Presentation)

Y. Yang, 35th Gibbs Conference on Biological Thermodynamics, Online, 2021 (Poster)

Y. Yang, Amecican Physical Society (APS) Mid-Atlantic Section Fall Meeting, Online, 2020 (Oral Presentation)

Y. Yang, 34th Gibbs Conference on Biological Thermodynamics, Online, 2020 (Poster)

Dedicated to my wife, Hewei Zhang and son, Kubo Yang

ACKNOWLEDGMENT

I would like to express my deepest gratitude to my advisor, Dr. Cristiano L. Dias, for his help, encouragement and support throughout my graduate studies. He not only offered me this opportunity to work on the fascinating project, but also taught me how to be a researcher, with his insightful guidance and tremendous patience. He has always been there to help whenever I had a question or trouble, and I have always been inspired by his expertise and enthusiasm for science. The experience of working with him has changed my way of thinking and working, which will always be precious to me.

I would like to thank the members of my committee: Tao Zhou, Hao Chen, Ian Gatley, Andres Jerez, Yong-Ick Kim and Mikko P. Haataja, for taking the time to read my dissertation, attending my defense, and providing valuable comments.

This work was supported by the National Science Foundation under Grant Nos. CHE-1904364 and CHE-1904528. Computational resources were provided by the Academic and Research Computing System (ARCS) at New Jersey Institute of Technology and by the Pittsburgh Supercomputing Center (PSC). Anton 2 at PSC is supported by the National Instituted of General Medical Sciences of the National Institute of Health under Award Number R01GM116961. The Anton 2 machine at PSC was generously made available by D. E. Shaw Research.

I thank my group members, Sharareh Jalali and Liyan Cheung for their help and companionship. I thank Dr. Haimin Wang for his help to me and my family. I thank my friends, Haizheng Zhuang and Huize Xue for their help and companionship.

Last but not least, I thank my parents, Xuande Yang and Chunying Li for their everlasting love. A great thanks go to my wife, Hewei Zhang, for her supporting to my family and everlasting love.

TABLE OF CONTENTS

TABLE OF CONTENTS
(Continued)

Chapter **Page**

LIST OF TABLES

Table **Page**

LIST OF FIGURES

LIST OF FIGURES
(Continued)

Figure **Page**

LIST OF FIGURES
(Continued)

Figure **Page**

LIST OF FIGURES
(Continued)

Figure **Page**

LIST OF FIGURES
(Continued)

Figure **Page**

LIST OF FIGURES
(Continued)

Figure **Page**

CHAPTER 1

INTRODUCTION

Amyloid diseases, which include Alzheimer's (AD), Parkinson's and Type II diabetes are characterized by the aggregation of peptides into soluble oligomers and fibrils. Interactions of these aggregates with the cell membrane account for an important mechanism of cell toxicity wherein annular shaped oligomers can form pores in lipid bilayers and amyloid fibrils can induce lipid loss through a detergent-like mechanism [4–9] — see Figure 1.1. These types of damages increase the vulnerability of neurons and they can lead to cell death [10,11]. Several factors have been shown to affect toxicity by amyloid peptides including lipid composition of the membrane and the presence of ions in the solution [12–25]. Currently, the molecular mechanisms accounting for amyloid-membrane interactions remain poorly understood as well as how these mechanisms are affected by lipid composition, ions, and pH. This fundamental knowledge is critical to better understand cell toxicity and it may enable rational designs of new therapeutics to treat amyloid diseases.

The aim of this dissertation is to provide insights into amyloid-membrane interactions using all-atom molecular dynamics simulation. This will allow us to address important open questions including: 1.What is the molecular forces driving the attraction of amyloid peptides to the cell membrane? 2. How is this attraction affected by the lipid composition and the presence of ions in the solution? 3. How is the attraction of individual peptides to the membrane affected by the amino acid sequence? 4. How is the lipid membrane disrupted during amyloid aggregation accounting for cell toxicity?

To address the different questions listed above, we have studied variations of three different systems. First, we simulated the interaction of the amphipathic

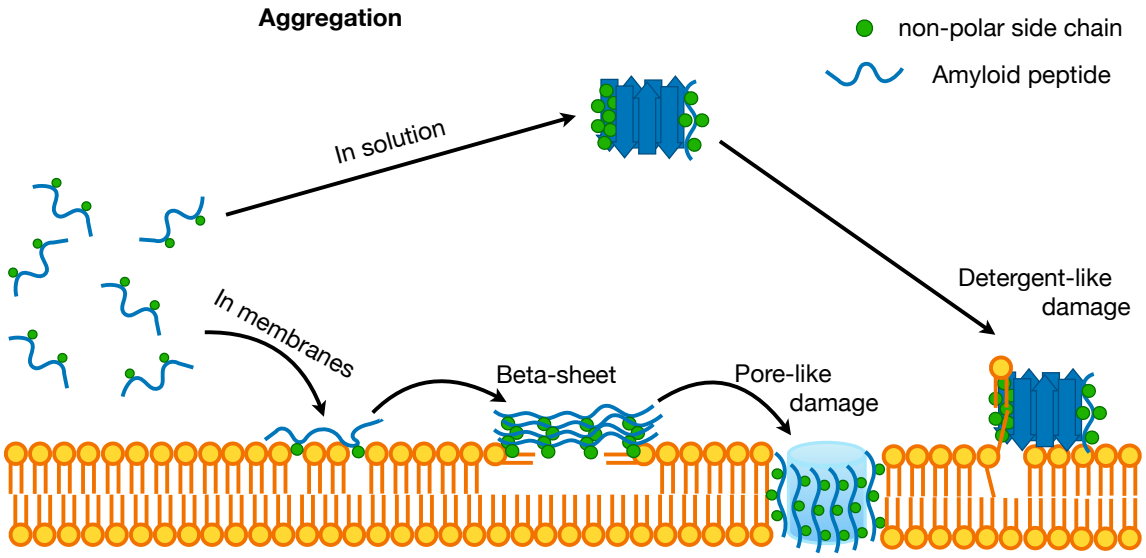

Figure 1.1 Schematic representation of the membrane damage as well as the aggregation of amyloid proteins in membranous environment.

peptide Ac-$(FKFE)_2$-NH_2 with lipid bilayers. We used membranes with different lipid compositions in the presence and absence of ions. Details and results from these simulations are provided in Chapter 3. Second, we performed a number of simulations using different peptide sequences. The latter are variants of the Ac-$(FKFE)_2$-NH_2 peptide to which we added net charges or altered the amino acid order. Details and results from these simulations are provided in Chapter 4. Third, we simulated the interaction of different amyloid aggregates, e.g., monomers, oligomers and fibrils, with lipid bilayers. Substantial damages by monomers and oligomers were observed in the simulations, whereas fibrils are relatively less toxic. Details and analysis of these simulations are provided in Chapter 5. In Chapter 2, we provide some background information to understand this thesis including a discussion about proteins, their aggregation into amyloid fibrils, and the molecular dynamics methodology.

CHAPTER 2

BACKGROUND

2.1 Protein

Proteins are biomolecules that use amino acids as their building blocks. They are widely present in living systems accounting for 50–70% of the dry mass of cells. Enzyme, actin, myosin and tubulin, are all examples of proteins. Most of the function in cells are performed by these biomolecules including signal transduction, catalysis, and cell adhesion. In the same vein, antibodies, which are responsible for conferring immunity to humans, are made of proteins. Another case in point is the cytoskeleton of the cell that is constituted primarily of proteins accounting for their mechanical properties and shape. Protein function is determined by its three-dimensional structure, so that obtaining the structure of a protein is crucial to understand its biological function. In this chapter, I provide a brief introduction about proteins for physicists and how they are modeled using all-atom molecular dynamics. This is the main tool used my thesis to address important fundamental questions regarding peptide-membrane interactions.

Amino acids. Amino acids are the building blocks of proteins. They are comprised of three chemical groups, i.e., amino (-NH_2), carboxyl (-COOH) and side chain (R) connected by a central carbon atom (C_α)— see Figure 2.1a. Twenty standard amino acids identified from proteins can be classified into three categories according to the charge in their side chains: non-polar, polar and charged. Physically, non-polar side chains known as hydrophobes are seemingly repelled from water molecules. Hence, they are prone to attract each other to form an hydrophobic core. In this core, the solvent accessible area of hydrophobic molecules is reduced. We will discuss this hydrophobic effect subsequently due to its importance in the folding of

proteins into their functional conformations. Besides, all the amino acids except for glycine can exist in L-form (Figure 2.1b) and D-form (Figure 2.1c) corresponding to left-handed and right-handed symmetries, respectively. Interestingly, some unknown type of "symmetry breaking" took place in early biological systems such that today only L-form amino acids are being used in living systems.

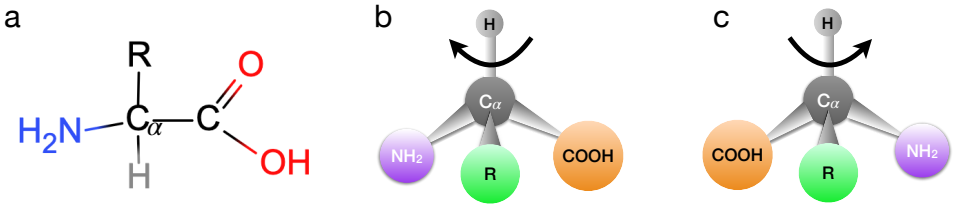

Figure 2.1 (a) Chemical structure of amino acid. Schematics of (b) L-form amino acid and (c) D-form amino acid.

Primary structure. In cells, proteins are synthesized by ribosomes through dehydration reaction between the amino group of one amino acid and the carboxyl group of another— see Figure 2.2. In this reaction a water is eliminated from carboxyl and amino groups with carbon and nitrogen atoms forming a peptide bond. When this chemical reaction occurs consecutively among many amino acids, a linear sequence comprised of amino acid residues (defined as in the red dotted box in Figure 2.2) is formed. This sequence of residues is known as the primary structure of the protein. The amino and carboxyl groups at the two ends of the sequence referred to as N-terminus and C-terminus, respectively, remain unneutralized. These termini can usually attract ligand with opposite charges leading to the ligand binding.

Hydrogen bond. Before the discussion of secondary structure for proteins, it is worth casting a glance at hydrogen bond that acts as a glue to stabilize the secondary structure. Hydrogen bond is formed between a hydrogen atom that is covalently bound to a strongly electronegative atom or group referred to as the hydrogen bond donor, and another electronegative atom referred to as the hydrogen bond acceptor through electrostatic force. Nitrogen and oxygen atoms are the most common donor or acceptor of hydrogen bond, e.g., O—H:::O, N—H:::O and N—H:::N, whereas carbon

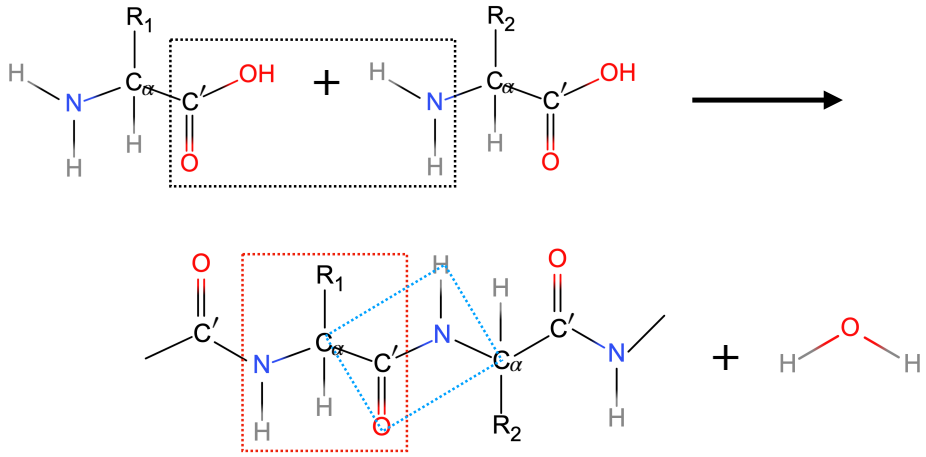

Figure 2.2 Dehydration reaction between two amino acids. Black dotted box highlight the chemical groups involved in the reaction. Red dotted box includes an amino acid residue and blue dotted box represents the peptide unit.

atom can not act as the donor due to its weak electronegativity. Hydrogen bond is ubiquitous in aqueous environment. For example, water exhibits anomalously high melting and boiling temperatures compared with other molecules which even have a bigger mass. This anomaly can be explained by the hydrogen bond that provides a strong intermolecular attraction between water molecules. Likewise, the C′O group and NH group in the backbone of protein are potent hydrogen bond acceptor and donor, respectively.

Secondary structure. For the convenience of discussing three dimensional structure of proteins, we adopt another repeating unit, i.e., peptide unit instead of amino acid residue— see the blue dotted box in Figure 2.2. In this unit, each C_α atom belongs to both adjacent two peptide units and C_α, carbonylic carbon (C′), N, O and H atoms in the same peptide unit are coplanar, because the mutually perpendicular p_z and sp^2 hybrid orbitals of C′ and N atoms lock down the rotation of C′-N bond. Figure 2.3 illustrates this coplannarity. Based on the frame above, there are only two degrees of freedom between two adjacent peptide unit planes, i.e., ψ and ϕ— see Figure 2.3. Sequentially, a polypeptide with N amino acid residues

has $2 \times (N-1)$ degrees of freedom. Since the steric collision between side chains and main chain, ϕ and ψ can not adopt any arbitrary values. Ramachandran plot shows the allowed combinations of the angles ψ and ϕ [26]–see Figure 2.4. Within these allowed regions, linear sequences comprised of amino acid residues fold to form their secondary structures.

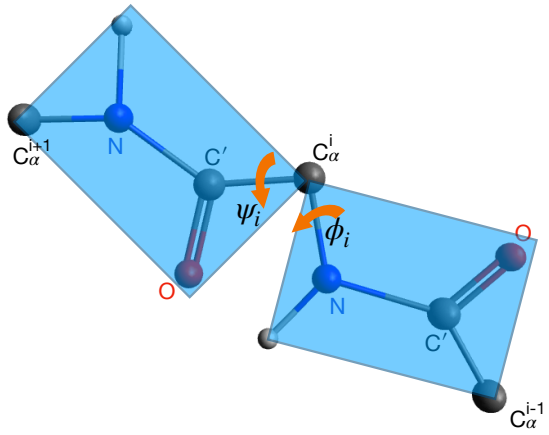

Figure 2.3 Schematic of two adjacent peptide units. Blue transparent boxes represent the peptide unit planes wherein the spatial conformation varies through the change of two angles (ψ and ϕ).

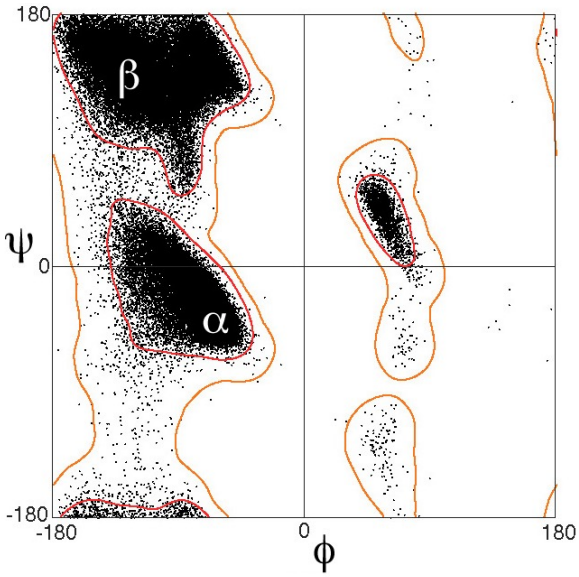

Figure 2.4 Ramachandran plot for the general case. Data from Lovell 2003. *Source: [1]*

The typical elements of secondary structure could be α helix and β sheet that are widely adopted by proteins. An example of protein structured by α helix and β sheet is shown in Figure 2.5a [2]. Specifically, in α helix, all the ϕ and ψ angle pairs involving the consecutive residues are approximately -60° and -50°, wherein hydrogen bonds formed between C′O of residue n and NH of residue $n+4$ resulting in a helix of 3.6 residues per turn— see Figure 2.5b. In addition, right-handed α helix is more favorable energetically compared with left-handed one. Besides the most common α helix, proteins can also adopt π helix and 3_{10} helix with hydrogen bonds to residue $n+5$ and $n+3$, respectively. On the contrary, the other major

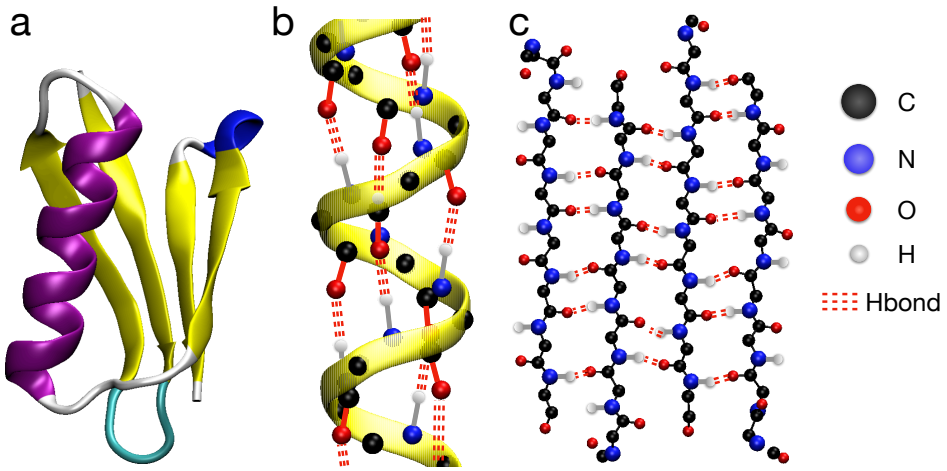

Figure 2.5 (a) Crystal structure of GB1 (PDB: 4WH4). β sheet and α helix are highlighted in yellow and purple, respectively. Loop regions are presented by white, cyan and blue. Schematics of (b) α helix and (c) Anti-parallel β sheet.
Source: [2]

secondary structure element β sheet shows a more straight forward picture. It is built up by several β strands aligned adjacent to each other such that hydrogen bonds can form between C′O groups of one β strand and NH groups of an adjacent β strand— see Figure 2.5c. A β sheet with all the β strands aligned in a same direction, i.e., N-terminus to C-terminus, is referred to as parallel, whereas anti-parallel is defined as the adjacent β strands aligned in opposite directions. The secondary structures of proteins are usually the combinations of α helices and β sheets connected by

loop regions— see Figure 2.5a, in which charged groups, i.e., C′O and NH, without neutralizing by hydrogen bonds usually constitute the surface of proteins, such that water molecules can form hydrogen bonds with these groups. As described above, the most striking feature of the secondary structure is the periodicity of backbone conformation, although their side chains' conformation varies from each other.

Protein folding. A single polypeptide chain with one or more secondary structures will folds to form a tertiary structure, a number of which may fold into a quaternary structure. Protein folds to form certain three-dimensional (3D) structure during or closely following its biological synthesis *in vivo*. Nevertheless, it is worth mentioning that this process doesn't have to be with biological synthesis. Anfinsen discovered that an unfolded protein is able to refold spontaneously *in vitro* [27], indicating that the amino acid sequence determines 3D structure of protein under proper temperature and pH, which is referred to as self-organization. Meanwhile, 3D structure also determines the function of protein.

Protein folding reaction can be completed within a few microseconds [28], implying that polypeptide would not undergo all the possible conformations to reach the most stable one, considering the enormous possible conformations even for a short sequence. A possible explanation is that the folding reaction proceeds along one or a limited number of paths. Hence, it is possible that amino acid sequence also determines the folding path and dynamics as well as the native conformation of protein.

Native conformation is likely to be the most stable one for the vast majority of proteins, although there is no big difference in energy between folded and unfolded states. Hydrogen bond plays an important role in the protein folding due to its critical contribution to the system. The loss of only several hydrogen bonds can damage the whole protein structure. Meanwhile, hydrophobic interaction is also indispensable

in the protein folding, wherein hydrophobic (non-polar) groups are inclined to be embedded inside to form a hydrophobic core.

Hydrophobic interaction. Since the importance of hydrophobic interaction in protein folding as well as many biological processes, it is worth introducing more on that. All the non-polar molecules, e.g., noble gases, hydrogen and pure hydrocarbons are hydrophobic. Many amino acid residues in protein have hydrocarbon side chains inducing the forming of hydrophobic core to reduce the exposure of hydrophobic side chains to water.

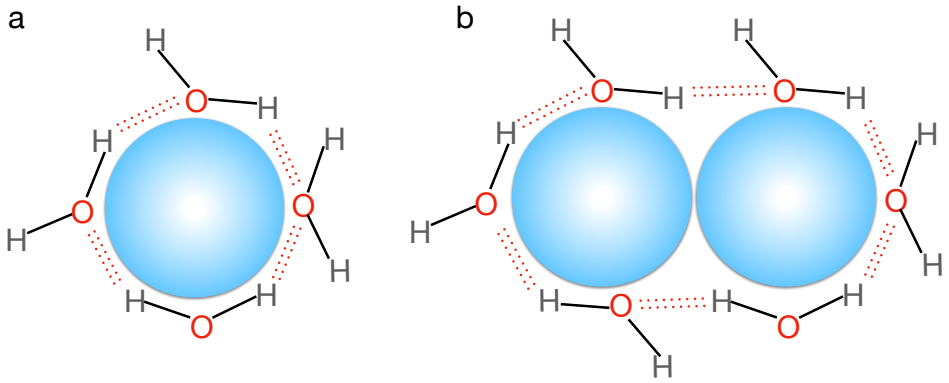

Figure 2.6 (a) Schematics of water molecules with hydrogen bonds around a non-polar molecule and (b) a pair of the identical molecules.

Experimentally, the study of vapor-liquid equilibrium of non-polar molecules with water indicate that the concentration of non-polar molecules in vapor are much higher than that in water. Noticing that vapor can be seen as vacuum, non-polar molecules evidently prefer to stay in a non-polar environment rather than water. Specifically, the equilibrium concentrations of methane in vapor and water at 283.89 K and 5 MPa are 1.34×10^3 mol/L and 0.298×10^3 mol/L, respectively [29]. The free energy change due to the transportation of molecules from vapor to water can be estimated as $\Delta G = -RTln(x_{water}/x_{vapor})$, where x_{water} is the equilibrium concentration in water and x_{vapor} in vapor. Hence, moving methane from vapor to water will result in an increase in free energy of $\Delta G = +\ 0.846$ kcal/mol. It is known that free energy is determined by energy and entropy ($\Delta G = \Delta H - T\Delta S$), whereas

ΔH is believed to decrease due to the entering of non-polar molecules into water. Hence, the hydrophobic effect is believed to be related to the change of entropy. As a kind of polar molecule, water molecules are bound together through hydrogen bonds to lower the energy. A polar molecule can also form hydrogen bonds with water, nevertheless the intruding of a non-polar molecule will sequester water molecules breaking hydrogen bonds between them. In order to compensate the increase of energy caused by the loss of hydrogen bonds, water molecules surrounding the non-polar molecule must freeze to adopt certain orientations to form hydrogen bonds with each other— see Figure 2.6a, leading to the decrease of entropy. Apparently, the proximity of non-polar molecules can decrease the area of hydrophobic surface lowering the decrease of entropy— see Figure 2.6b. Consequently, non-polar molecules tend to bind together to form hydrophobic bonds. On the other hand, noticing the second term pertaining to entropy in free energy $-T\Delta S$, hydrophobic effect strongly depends on temperature. Intuitively, hydrophobic effect seems to get stronger with temperature due to the entropy related term $-T\Delta S$ being proportional to T. However, that is only the case at low temperature. Hydrogen bonds can be broken by thermal motion resulting in a weakening of hydrophobic effect at high temperature.

2.2 Amyloid and Alzheimer's Disease

Most proteins must fold properly to implement their function. In contrast, amyloid proteins are intrinsically disordered and prone to aggregating into insoluble extracellular fibrils. The deposition of amyloid fibrils are related to approximately 50 human diseases [30], e.g., Alzheimer's by amyloid-β, Parkinson's by α-synuclein, Huntington's by Huntingtin and type II diabetes by amylin.

In particular, Alzheimer's (AD) is a neurodegenerative disease that causes over 60% of cases of dementia, symptomized by short-term memory impairment, disorientation, language problems, etc. Tens of millions of people suffered from AD

worldwide resulting in a large financial burden to society. Nevertheless, there is not any therapeutics to either stop or reverse the progress of AD. Amyloid plaques are extracellular deposits of amyloid-β (Aβ) fibrils detected mainly in the grey matter of patients' brain [31], which is a hallmark of AD. The relation between Aβ and Alzheimer's has been determined by genetic studies. In particular, individuals carrying three copies of the gene encoding for Aβ (e.g., Down syndrome) almost prevalently show the early stage symptoms of AD by 40 years of age [32].

Amyloid fibril exhibit a cross-β diffraction pattern (Figure 2.7), which was first discovered by Astbury [33] through exposing a poached egg white under X-rays. In fibril, β-strands stack along the fibril axis forming β sheets that are parallel to each other— see Figure 2.7. The diffraction peaks along the equator correspond to the stacking of β sheets with a space of $\sim$10 Å and meridian peaks reflect the stacking of β strands along the fibril axis spaced 4.8 Å apart— see Figure 2.7.

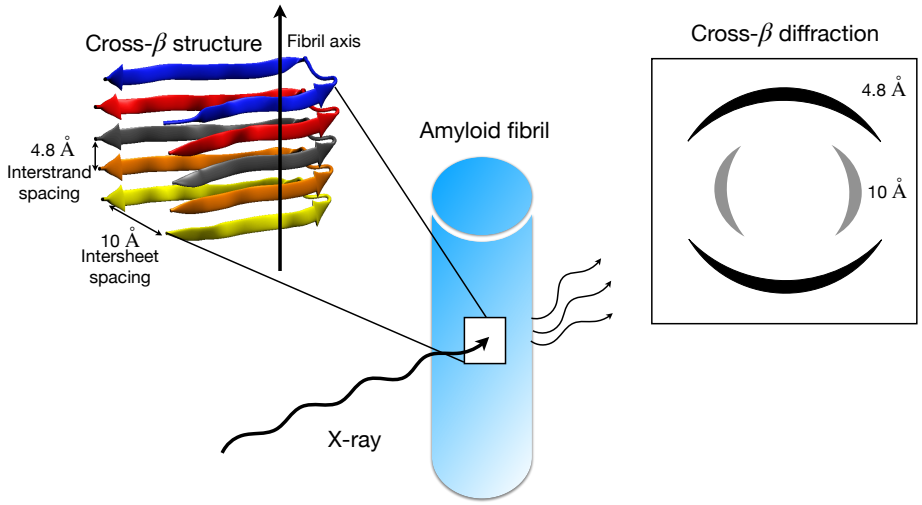

Figure 2.7 A characteristic cross-β diffraction pattern. The diffraction peaks along the equator (gray) show that the peptides are organized into β sheets spaced $\sim$10 Å apart. The meridian peaks (black) reflect a space of 4.8 Å between β strands along fibril axis. The left image is the structure of Aβ(1-42) fibril (PDB: 2BEG) as an example that peptides stack into fibril wherein fibril axis, interstrand and intersheet spaces are highlighted.
Source: [3]

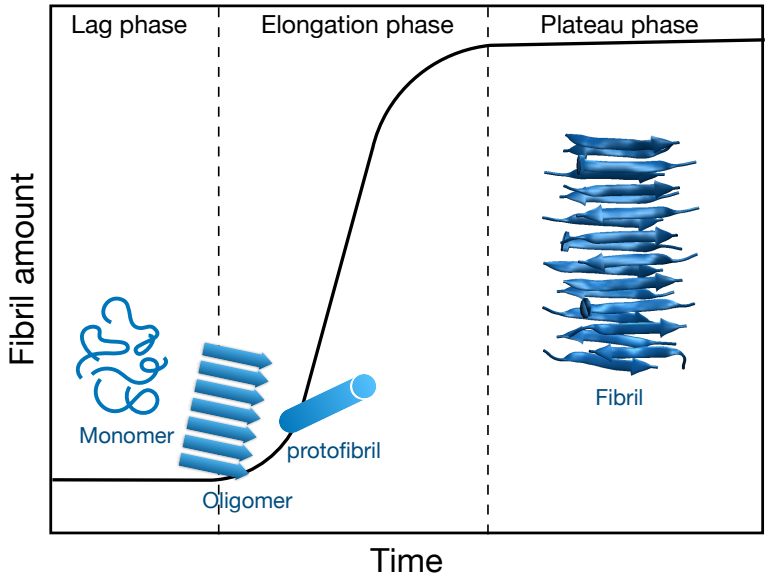

Figure 2.8 Aggregation of amyloid peptides into fibrils, wherein three phases are identified: lag phase, elongation phase and plateau phase. Conformation of protein corresponding to each phase is highlighted in blue cartoon. The fibril on the right is a fibril assembled *in silico* from modeled peptides by our group.

The aggregation of proteins can follow several different paths, wherein "off-pathway" aggregation results in amorphous deposits [34]. A typical "on-pathway" aggregation initiates from monomers undergoing lag phase and fast elongation phase— see Figure 2.8. Specifically, in the lag phase, monomers undergoes a conformational change to misfold into a structure with aggregation propensity, followed by oligomerization forming nuclei, which is the slowest process in the whole aggregation. The aggregation will come into a fast-growth procedure after the formation of nuclei in the lag phase, wherein small fibrils elongate fast until saturation [35]. It should be noticed that different aggregation paths may generate different intermediates leading to different morphologies of fibril for the same sequence [36]. Extensive studies show that amyloid fibrils may not be the primary toxic species causing amyloid disease. It is found that the concentration of Aβ fibrils does not have a correlation with different stages of AD [37]. There are a large number of evidences that the soluble intermediates of Aβ aggregation, i.e., oligomers, are more accountable for the toxicity to neurons [38, 39].

2.3 Cell Membrane

Cell membrane (known as plasma membrane) is a double layered structure (known as bilayer) that separates the interior of cells from external environment to maintain the intracelluar homeostasis. This structure is also referred to as lipid bilayer which comprises various types of lipids. Besides, membrane proteins and sugars also play important roles in the membrane functioning.

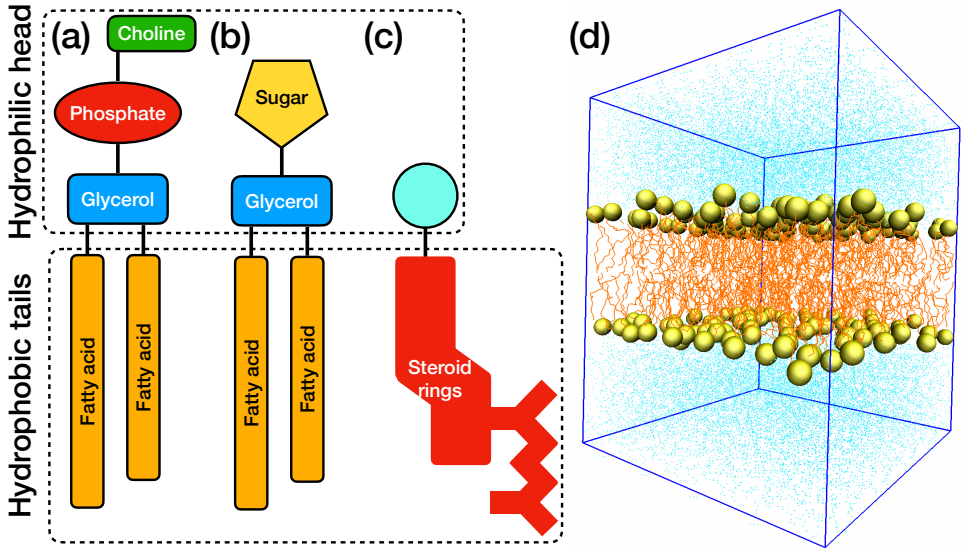

Figure 2.9 Schematic representation of a (a) phospholipid, (b) glycolipid and (c) sterol. (d) A snapshot of lipid bilayer in water box.

Three types of lipids, i.e., phospholipid, glycolipid and sterol can be found in all kinds of cells. Phospholipid has two fatty acid chains linked to glycerol and phosphate group through covalent bonds. These phospholipids containing glycerol are also referred to as glycerolphospholipid. A widely found glycerolphospholipid in cell membrane is phosphatidylcholine (PC), which has a choline bond to the phosphate group—see Figure 2.9a. Glycerolphospholipids containing serine and ethanolamine instead of choline are called phosphotidylserine (PS) and phosphotidylethanolamine (PE), respectively. Phospolipids containing sphingosine instead of glycerol in this position are sphingophospholipids which are usually found in membranous myelin sheath around neuron axons. Glycolipids always have a sugar such as glucose

replacing the phosphate group in phospholipids—see Figure 2.9b. In glycolipids, glycerol can also be sphingosine. Sterol is an important component of animal and plant membranes, but absent from bacteria. Typical sterol found in animal membrane is cholesterol. Cholesterol comprises a hydroxyl group, four steroid rings and a hydrocarbon side chain—see Figure 2.9c.

All lipids contain both hydrophobic and hydrophilic regions. This amphipathic nature makes them form stable bilayers in aqueous environment, wherein the hydrophilic head groups point outward towards the solution-bilayer interface and the hydrophobic tails are embedded forming a dry core—see Figure 2.9d. The dynamic and fluid nature of cell membrane are important for its functioning. In particular, lipids can diffuse laterally through the leaflets as well as diffuse more quickly in the leaflet. Lipids can also spin around their head-to-tail axis. The lipid tails are very flexible in *liquid phase*. Lipid bilayer can undergo phase transition upon cooling down, wherein the fluidity of lipids is dramatically reduced and lipid tails become highly ordered, i.e., *gel phase*. Deuterium order parameter has been widely used to characterize the order of lipid tails [40]. This quantity can be measured by ^{2}H NMR experiments and computed from simulation trajectories. Researchers usually assess their simulation model by comparing this parameter with experimentally measured one. We will also capitalize on this parameter in our study. More details about the order parameter will be discussed later on.

2.4 Methodology

In order to get insights into amyloid-membrane interaction at atomic level, we are going to use molecular dynamics (MD) simulation that allows us to obtain trajectories containing molecular information *in silico*.

2.4.1 Molecular dynamics simulation

Molecular dynamic simulation is a widely used method to acquire the evolution of conformation through numerically solving Newton's equations of motion for a system of interacting particles. Practically, MD simulation adopt an algorithm of finite difference with a finite step time Δt to replace the infinitesimal dt, followed by the numerical integration. The definition of Δt depends on the motion of atom nuclei, whose oscillation time scale is $\sim 10^{-14}$ s, and accordingly the Δt in MD simulations for normal compounds is always adopted to be the scale of $\sim 10^{-15}$ s (fs).

Verlet algorithm is a numerical method that was firstly carried out by Loup Verlet in 1967 [41] and frequently used to integrate Newton's equations of motion in MD simulations. Verlet algorithm starts with the Taylor series expansions of particle coordinate $\mathbf{r}(t)$:

$$\mathbf{r}(+\delta t) = \mathbf{r} + \frac{d\mathbf{r}}{dt}\delta t + \frac{1}{2!}\frac{d^2\mathbf{r}}{dt^2}\delta t^2 + \cdots \tag{2.1}$$

$$\mathbf{r}(-\delta t) = \mathbf{r} - \frac{d\mathbf{r}}{dt}\delta t + \frac{1}{2!}\frac{d^2\mathbf{r}}{dt^2}\delta t^2 - \cdots \tag{2.2}$$

Adding Equation (2.1) and (2.2) results in:

$$\mathbf{r}(t+\delta t) = 2\mathbf{r}(t) - \mathbf{r}(t-\delta t) + \frac{d^2\mathbf{r}}{dt^2}\delta t^2 \tag{2.3}$$

The displacement of molecule can be calculated without involving its velocity from Equation (2.3), whereas velocity is required to calculate the kinetic energy of system by simply subtracting Equation (2.1) and (2.2):

$$\mathbf{v}(t) = \frac{d\mathbf{r}}{dt} = \frac{1}{2\delta t}[\mathbf{r}(r+\delta t) - \mathbf{r}(t-\delta t)] \tag{2.4}$$

Verlet algorithm is one of the most popular method used in MD simulations due to its easy implementation in computer program. Moreover, Verlet algorithm provides advantages that are crucial for physical systems such as time reversibility

and preservation of the symplectic structure of phase space. A downside of Verlet algorithm is the lack of coordinate information for $t - \delta t$ when simulation launches, such that it has to estimate $\mathbf{r}(t - \delta t)$ for $t = 0$. Nevertheless, the evolution of system will be independent on the initial condition as the simulation proceeds long enough such that the system goes into equilibrium. Another shortcoming of Verlet algorithm is the mismatch in synchronicity when calculates the velocity. Specifically, $\mathbf{v}(t)$ (Equation (2.4)) and $\mathbf{r}(t + \delta t)$ (Equation (2.3)) are calculated simultaneously such that the velocity saved in each step is actually the one when particle at the coordinate in the last step. The memory needs to save coordinates and accelerations of the current step and coordinates of the last step. Subsequently, a series of methods emerged to improve Verlet algorithm.

Leapfrog Verlet algorithm is an improved method to Verlet algorithm raised by Hockney in 1970 [42], wherein it handles the velocity by a half step $\frac{1}{2}\delta t$:

$$\mathbf{r}(t + \delta t) = \mathbf{r}(t) + \mathbf{v}(t + \frac{1}{2}\delta t)\delta t \tag{2.5}$$

$$\mathbf{v}(r + \frac{1}{2}\delta t) = \mathbf{v}(t - \frac{1}{2}\delta t) + \mathbf{a}(t)\delta t, \tag{2.6}$$

such that $\mathbf{v}(t)$ can be calculated by

$$\mathbf{v}(t) = \frac{1}{2}[\mathbf{v}(t + \frac{1}{2}\delta t) + \mathbf{v}(t - \frac{1}{2}\delta t)]. \tag{2.7}$$

Consequently, only $\mathbf{v}(t - \frac{1}{2}\delta t)$ and $\mathbf{r}(t)$ occupy the memory saving a lot of computational resources. Leapfrog Verlet method is frequently used in MD simulations for its simplicity, accuracy and stability. Leapfrog Verlet method calculates the coordinates and velocities with smaller errors than the original Verlet method, nevertheless the synchronicity problem still exist.

Speed Verlet algorithm was proposed by Swope in 1982 [43] to improve the calculation of speed:

$$\mathbf{r}(t+\delta t) = \mathbf{r} + \mathbf{v}(t)\delta t + \frac{1}{2}\mathbf{a}(t)\delta t^2 \tag{2.8}$$

$$\mathbf{v}(t+\frac{1}{2}\delta t) = \mathbf{v}(t) + \frac{1}{2}\mathbf{a}(t)\delta t \tag{2.9}$$

$$\mathbf{v}(t+\delta t) = \mathbf{v}(t+\frac{1}{2}\delta t) + \frac{1}{2}\mathbf{a}(t+\delta t)\delta t, \tag{2.10}$$

wherein coordinates at $t+\delta t$ and velocities at $t+\frac{1}{2}\delta t$ are calculated by Equation (2.8) and (2.9). Then accelerations at $t+\delta t$ can be derived from $\mathbf{r}(t+\delta t)$, such that $\mathbf{v}(t+\delta t)$ can be calculated by Equation (2.10). Speed Verlet algorithm gives a higher accuracy than original Verlet as well as a higher efficiency in managing memory without the need to save any quantity at $t+\delta t$. Speed Verlet method solve the synchronicity problem calculating speeds and coordinates at $t+\delta t$ in the same step. However, Speed Verlet algorithm is more complicated than Verlet and Leapfrog computationally.

Beeman algorithm might be the most accurate one in calculating velocities among all the Verlet series algorithms [44]:

$$\mathbf{r}(t+\delta t) = \mathbf{r}(t) + \mathbf{v}(t)\delta t + \frac{1}{6}[4\mathbf{a}(t) - \mathbf{a}(t-\delta t)]\delta t^2 \tag{2.11}$$

$$\mathbf{v}(t+\delta t) = \mathbf{v}(t) + \frac{1}{6}[2\mathbf{a}(t+\delta t) + 5\mathbf{a}(t) - \mathbf{a}(t-\delta t)]\delta t, \tag{2.12}$$

wherein Equation (2.12) undoubtably keep the synchrony of coordinates and velocities in the calculations. Beeman Verlet algorithm can adopt a larger step time, whereas the calculation of velocity is not reversible as well as the consumption of computational resource is high for its complication.

In MD simulation, the algorithms based on Newton's equations of motion naturally satisfy the conservation of energy. However, the vast majority of MD simulations for biological system are performed on an ensemble with fixed

temperature and pressure (NPT), such that a thermostat and a barostat are required. Thermostats in MD simulation including velocity scaling [45], Berendsen [46], Andersen [47], Nosé [48] and Nosé-Hoover [49] will be introduced here.

Velocity scaling method is the simplest one to keep a constant temperature for the system, wherein it rescales the velocities of particle periodically. The kinetic energy of each particle is calculated as

$$\langle K \rangle = \frac{1}{2N} \left\langle \sum_i m_i \mathbf{v}_i \cdot \mathbf{v}_i \right\rangle, \tag{2.13}$$

where the angle brackets represent time average. On the other hand, we can write the kinetic energy in another form from equipartition theorem:

$$\langle K \rangle = \frac{3}{2} kT \tag{2.14}$$

By combining Equation (2.13) and Equation (2.14) we have

$$T = \frac{1}{2Nk} \left\langle \sum_i m_i \mathbf{v}_i \cdot \mathbf{v}_i \right\rangle, \tag{2.15}$$

from which we can monitor the temperature of system in real time. Temperature is controlled by rescaling velocities as

$$\begin{aligned} v_{ix}^{new} &= v_{ix} \sqrt{\frac{T_D}{T_A}} \\ v_{iy}^{new} &= v_{iy} \sqrt{\frac{T_D}{T_A}} \\ v_{iz}^{new} &= v_{iz} \sqrt{\frac{T_D}{T_A}}, \end{aligned} \tag{2.16}$$

where T_A is the real temperature of system and T_D the setting temperature.

Berendsen method is another one to control the temperature, by which system is placed in a reservoir with the setting temperature. The function of the reservoir is to complement/remove energy from system when temperature becomes

lower/higher than the setting one. The real temperature T_A shifts as

$$\frac{dT_A}{dt} = \frac{T_D - T_A}{\tau}, \tag{2.17}$$

where τ is relaxation time with dimension of time, describing the coupling between the system and reservoir. Computationally, a discrete form of Equation (2.17) is applied:

$$\Delta T = \frac{\Delta t}{\tau}(T_D - T_A) \tag{2.18}$$

Accordingly, relations of velocity for Berendsen method are

$$\begin{aligned} v_{ix}^{new} &= v_i x \sqrt{1 + \frac{\Delta T}{\tau}\left(\frac{T_D}{T_A} - 1\right)} \\ v_{iy}^{new} &= v_i y \sqrt{1 + \frac{\Delta T}{\tau}\left(\frac{T_D}{T_A} - 1\right)} \\ v_{iz}^{new} &= v_i z \sqrt{1 + \frac{\Delta T}{\tau}\left(\frac{T_D}{T_A} - 1\right)}, \end{aligned} \tag{2.19}$$

which degenerate to Equation (2.16) in Velocity scaling method when $\tau = \Delta T$.

Anderesn method is another thermostat introduced to replace the velocity scaling method, which combines MD and stochastic process. System is soaked in a big reservoir with the setting temperature T, wherein temperature coupling is introduced by a stochastic collision between randomly selected particles. The collision is parameterized by a collision frequency ν, such that a particle's collision probability within time Δt is $\nu \Delta t$. Assuming that each collision is an independent event, time-dependent collision probability exhibits the Poisson distribution $P(t, \nu) = \nu e^{-\nu t}$. During the simulation, MD and stochastic collision are executed alternately, wherein particles follow the Newton's equations of motion during the interval between adjacent stochastic processes, such that the system evolves on an isoenergetic surface. A stochastic process shifts the system from one isoenergetic surface to another with the same temperature, signifying the ergodicity of the system evolving on an isothermal

surface. Andersen thermostat results in a canonical distribution, which reproduces properties of a canonical ensemble in equilibrium. However, Andersen thermostat involves artificial interactions that interrupt the authentic evolution of system and reduce time/spatial correlations, resulting in a low reliability in the simulation of diffusion coefficient. In general, Andersen method is appropriate to simulations on static properties rather than dynamics.

Nosé method introduce an extra degree of freedom s for heat bath to the Hamiltonian, by which it use the MD algorithm to maintain a constant temperature for system. The reservoir is considered to be a part of the system embodied by the extra degree of freedom in Hamiltonian:

$$H_{ext} = \sum_{i=1}^{N} \frac{\boldsymbol{p}_i^2}{2m_i s^2} + V(q) + \frac{\boldsymbol{p}_s^2}{2Q} + gkT_D lns, \tag{2.20}$$

where the first and second terms are the kinetic and potential energies of system, and the third and last terms are the counterparts of reservoir. The magnitude of Q determines the coupling strength between the reservoir and the real system such that influences the temperature fluctuations. s plays the role of a time-scaling parameter that stretch the time scale in the extended system. Therefore, the equations of motion are

$$\dot{\boldsymbol{q}} = \frac{\boldsymbol{p}}{ms^2} \tag{2.21}$$

$$\dot{\boldsymbol{p}} = \boldsymbol{F}(\boldsymbol{q}) \tag{2.22}$$

$$\dot{s} = \frac{\boldsymbol{p}_s}{Q} \tag{2.23}$$

$$\dot{\boldsymbol{p}} = \sum_i \frac{\boldsymbol{p}_i^2}{m_i s^3} - \frac{gkT_D}{s} \tag{2.24}$$

Nosé thermostat is also referred to as Nosé dynamics for the introducing of a Hamiltonian for the extended system. Nosé method maintains good ergodicity, time reversibility and consistent distribution for system studied, whereas the stretched virtual time scale results in a heterogeneous sampling under real time scale, bringing up inconvenience to the subsequent analysis, e.g., calculating time correlation function and non-equilibrium processes.

Nosé-Hoover method improves the Nosé method by Hoover in 1985, eliminating the parameter s which is difficult to calculate:

$$\dot{\boldsymbol{q}} = \frac{\boldsymbol{p}}{m} \tag{2.25}$$

$$\dot{\boldsymbol{p}} = \boldsymbol{F} - \xi \boldsymbol{p} \tag{2.26}$$

$$\dot{\xi} = \frac{\sum\limits_i \frac{\boldsymbol{p}_i^2}{m_i} - gkT_D}{Q}, \tag{2.27}$$

where ξ is a time-dependent friction coefficient calculated by iterating with the equations above. Equation (2.25) $\sim$ (2.27) produce a distribution that satisfies the homogeneous sampling under real time scale, leading to an advantage in the simulations for non-equilibrium process. Since we usually use a NPT ensemble that has a constant temperature and pressure in the simulations for biological systems, we introduce a typical barostat referred to as Nosś-Hoover barostat, wherein an extended dimension to Nosé-Hoover thermostat is applied to pressure. Based on rescaled coordinate $x \equiv q/V^{1/d}$, Hoover defined

$$\dot{\boldsymbol{x}} = \frac{\boldsymbol{p}}{mV^{1/d}} \tag{2.28}$$

$$\dot{\boldsymbol{p}} = \boldsymbol{F} - (\epsilon + \xi)\boldsymbol{p} \tag{2.29}$$

$$\dot{\xi} = \frac{\sum_i \frac{\boldsymbol{p}_i^2}{m_i} - gkT_D}{Q} \tag{2.30}$$

$$\dot{\varepsilon} = \frac{\dot{V}}{dV} \tag{2.31}$$

$$\ddot{\varepsilon} = \frac{P_A - P_D}{\tau^2 kT_D}, \tag{2.32}$$

where P_A and P_D are the real and setting pressure, τ the relaxation time. Equation (2.28) $\sim$ (2.32) involves an extra friction coefficient ε such that $\dot{\varepsilon}$ can be calculated by Equation (2.32) resembling the calculation of $\dot{\xi}$.

2.4.2 Force fields

The interactions between particles drives the evolution of the system. An accurate expression of the force field plays an important role in MD simulation. To define a force field, not only the forms of the functions but also a large numbers of parameters need to be determined. Here we focus on introducing the function forms used for different interactions in MD simulation. It is worth mentioning that different force fields may use a same function forms but different parameters.

Force fields in MD simulation are transferable and empirical. Namely, a force field can apply to a series of relevant molecules without modification to the parameters. On the other hand, the only approach that guarantees the absolute accuracy is the *ab initio* calculation involving quantum mechanics which is unaffordable computationally, such that force fields currently used in MD simulation are comprised of several terms including bonded interactions, e.g., bond stretching, angle bending and dihedral torsion— see Figure 2.10, and non-bonded interactions.

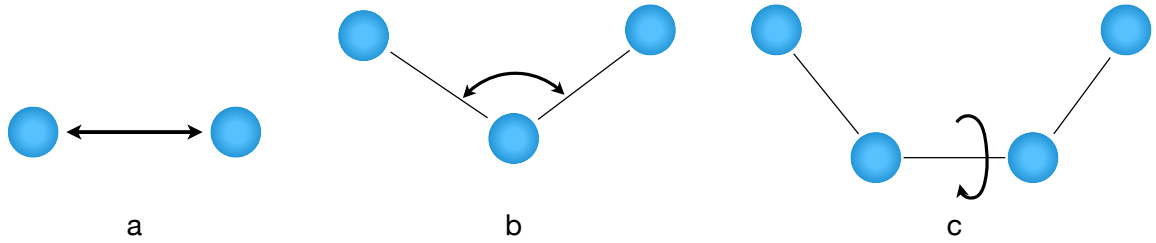

Figure 2.10 Schematics of (a) bond stretching, (b) angle bending and (c) dihedral torsion.

Bond stretching potential between two covalently bonded atoms can be described by Morse potential [50]:

$$u_b(l) = D_e\{1 - \exp\left[-\alpha(l - l_0)\right]\}^2, \tag{2.33}$$

where D_e and α are the depth of the well in kcal/mol and the steepness in nm^{-1}, and l_0 is the reference bond length. As shown in Figure 2.11, Morse potential can precisely describe the energy change with the bond length, whereas the high computational resource cost due to its exponential form as well as the requirement to define three parameters limit the application of Morse potential. A more popular form to describe the bond stretching is harmonic potential:

$$u_b(l) = \frac{1}{2}K_b(l - l_0)^2 \tag{2.34}$$

which is the first-order approximation of Morse potential using Taylor expansion. Harmonic potential merely applicable to a tiny amplitude vibration, where the bond length changes no more than 0.1 Å. To construct a more accurate force field, cubic and quartic terms in Taylor expansion of Morse potential are needed.

Angle bending potential can also be described by Hooke's law referred to as angle harmonic potential:

$$u_\theta(\theta) = \frac{1}{2}K_\theta(\theta - \theta_0)^2, \tag{2.35}$$

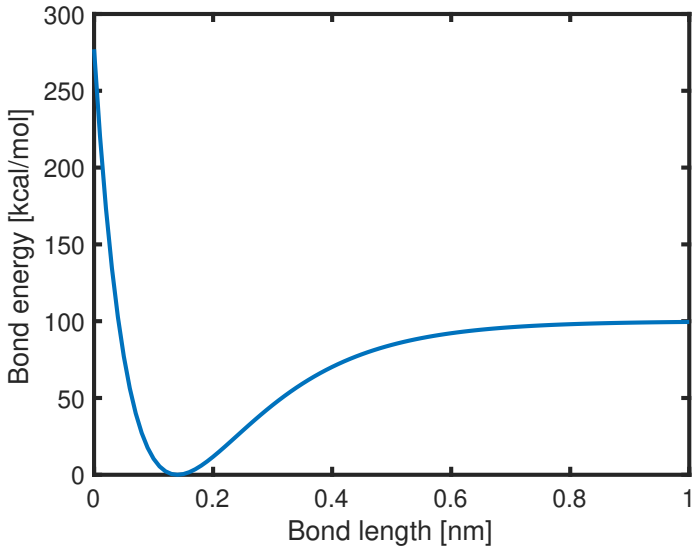

Figure 2.11 The Morse potential well with bond length 0.14 nm.

where θ_0 is the equilibrium bond angle in radian. Besides the cosine harmonic potential is usually used in MD simulations:

$$u_\theta(\theta) = \frac{1}{2}K_\theta(cos\theta - cos\theta_0)^2, \tag{2.36}$$

where θ_0 is the equilibrium bond angle in degree. As can been seen in Figure 2.12, cosine harmonic potential allows bond angle θ reaching 180° such that the calculation of torsion angle and potential is unstable in coarse-grained MD simulations. The restricted bending potential [51] systematically prevents the angle θ from reaching 180° through dividing Equation (2.36) by a $sin^2\theta$ factor:

$$u_\theta(\theta) = \frac{1}{2}K_\theta\frac{(cos\theta - cos\theta_0)^2}{sin^2\theta} \tag{2.37}$$

Since it is difficult to change the bond length and angle of a molecule, the previously discussed potentials are usually regarded as "hard degrees of freedom". On the contrary, dihedral and non-bonded interactions are more accountable for driving the conformational change of molecules. **Dihedral torsional potential** reflects the

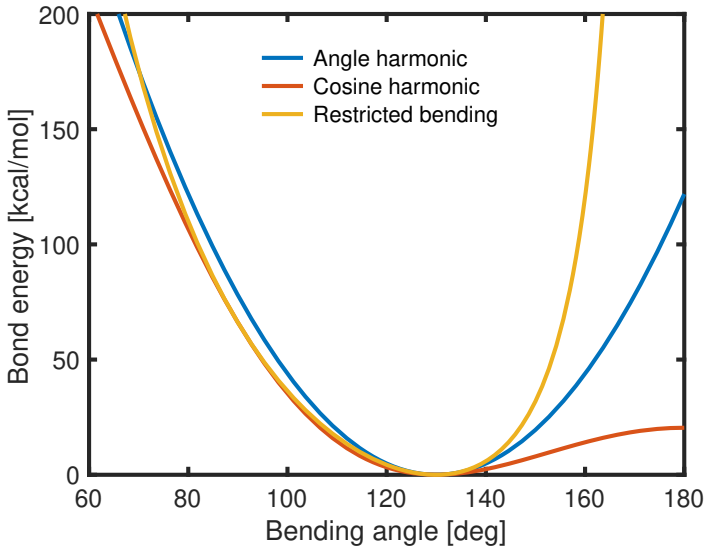

Figure 2.12 Bending angle potentials: angle harmonic (blue), cosine harmonic (red) and restricted bending (orange) with the same bending constant $K_\theta = 320$ kcal/mol and equilibrium angle $\theta = 130°$

energy change due to the rotation with respect to covalent bond— see Figure 2.10c. Dihedral torsional potential always expressed by trigonometric function series:

$$u_\omega(\omega) = \frac{1}{2}\sum_n V_n[1 + (-1)^{n+1} cosn\omega], \tag{2.38}$$

where V_n describes the depth of the well and n represents the number of times that the minimum emerges upon rotating 360° with respect to the bond. The value of n can be different with force fields, e.g., $n = 5$ or 6 in CHARMM force fields. Sometimes, a equilibrium dihedral ω_0 is introduced into Equation (2.38):

$$u_\omega(\omega) = \frac{1}{2}\sum_n V_n[1 + (-1)^{n+1} cos(n\omega - \omega_0)], \tag{2.39}$$

which is equivalent to Equation (2.38) when $\omega_0 = 0$ or π. There are some highly symmetric conformations corresponding to the extrema of dihedral potential referred to as *cis*, *gauche*, and *trans*— see Figure 2.13, wherein the *cis* relates to the maxima and the *gauche* and *trans* relate to the minima. Considering replacing the CH_3 group by H, the molecule holds a 3-fold rotational symmetry, where the *gauche* and

trans conformations are degenerate, resulting in the same value of three minima in dihedral potential. In this case, a term $\frac{1}{2}V_3[1 + cos3\omega]$ (3-fold) is proper to describe the potential—see the orange dashed lines in Figure 2.14. In most of hydrocarbon molecules, the values of minima are not equal. For example, the *trans* conformation has a lower energy than the *gauche* one in *butane* molecule, such that a summation of three terms, i.e., 1-fold, 2-fold and 3-fold, can express this feature—see the black solid line in Figure 2.14a. However, some molecules such as $2 - methylbutane$ exhibits a lower energy in *gauche* transformation, in which dihedral potential can be expressed by a summation of 2-fold and 3-fold— see the black solid line in Figure 2.14b.

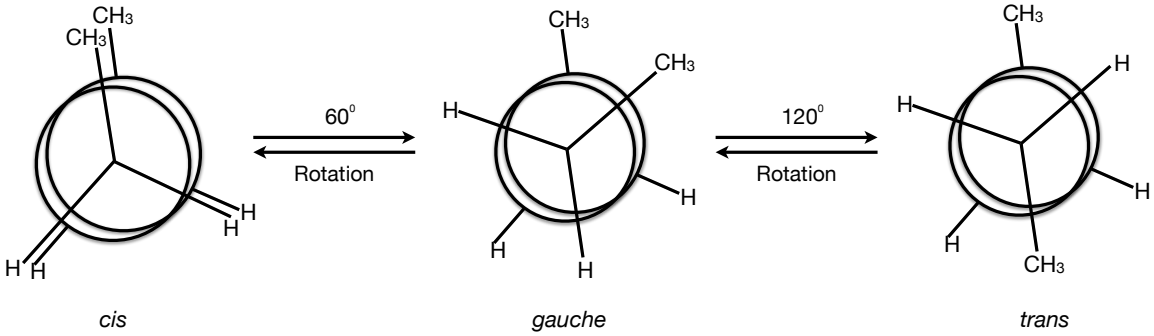

Figure 2.13 A schematic presentation of *cis* (left), *gauche* (middle) and *trans* (right) conformations of butane based on different diherals.

Besides, **cross terms** are needed to describe the coupling of degrees of freedom in molecule, e.g., the bond stretching can induce the change in bond angle and dihedral. Typical cross terms are listed as

a. bond stretching - bond stretching

$$u(l_1, l_2) = \frac{1}{2}K_{l_1,l_2}(l_1 - l_{1,0})(l_2 - l_{2,0}) \tag{2.40}$$

b. bond stretching - angle bending

$$u(l_1, l_2, \theta) = \frac{1}{2}K_{l_1,l_2,\theta}[(l_1 - l_{1,0}) + (l_2 - l_{2,0})](\theta - \theta_0) \tag{2.41}$$

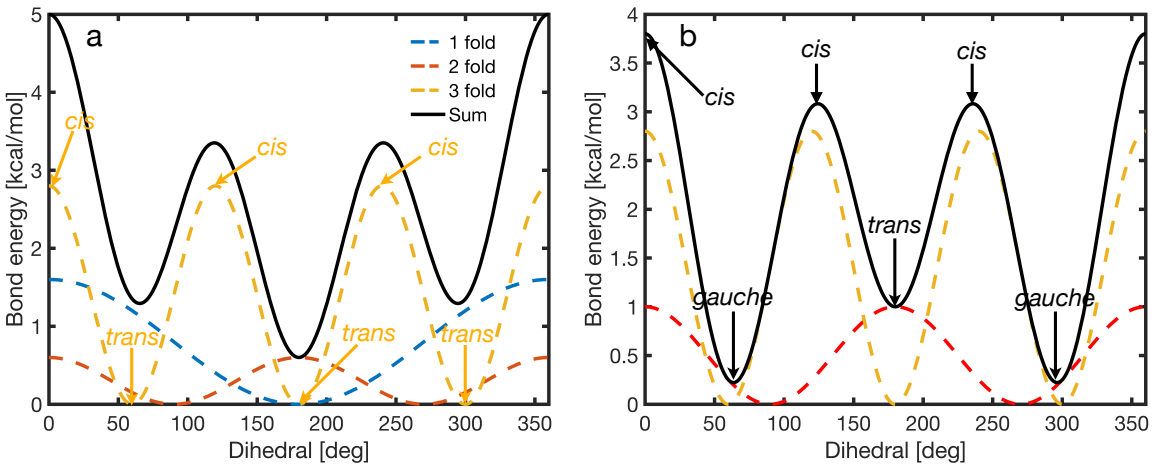

Figure 2.14 Dihedral torsion potential as a function of dihedral angle. (a) The case that the energy of *trans* conformation is lower than that of the *gauche* one, wherein $\frac{1}{2}V_1[1+cos(\omega)]$, $\frac{1}{2}V_2[1+cos(2\omega)]$ and $\frac{1}{2}V_3[1+cos(3\omega)]$ are referred to as 1-fold (blue dashed), 2-fold (red dashed), and 3-fold (orange dashed), of which the summation is represented in black solid line. (b) The case that the energy of *trans* conformation is higher than that of the *gauche* one, wherein the black solid line represents the summation of 2-fold and 3-fold. The angles of special conformations, i.e., *trans*, *cis* and *gauche* are highlighted in the corresponding color.

c. bond stretching - dihedral torsion

$$u(l,\omega) = \frac{1}{2}K_{l,\omega}(l-l_0)(1+cos3\omega) \tag{2.42}$$

d. angle bending - dihedral torsion

$$u(\theta,\omega) = \frac{1}{2}K_{\theta,\omega}(\theta-\theta_0)(1+cos3\omega) \tag{2.43}$$

e. angle bending - angle bending

$$u(\theta_1,\theta_2) = \frac{1}{2}K_{\theta_1,\theta_2}(\theta_1-\theta_{1,0})(\theta_2-\theta_{2,0}) \tag{2.44}$$

Non-bonded interactions contain a dispersion term, a repulsion term and a Coulomb term, among which the dispersion and repulsion terms are combined to form either the Lennard-Jones potential or the Buckingham potential. In particular,

the dispersion term describes the long-ranged interaction but the repulsion one relates to the short-ranged interaction. Lennard-Jones potential is also referred to as 12-6 potential:

$$u(r) = 4\varepsilon \left[\left(\frac{\sigma}{r} \right)^{12} - \left(\frac{\sigma}{r} \right)^{6} \right], \tag{2.45}$$

where σ is the collision diameter representing the distance where the potential equals 0 and ε the depth of the well. Buckingham has a more flexible and realistic repulsion term but is more expensive computationally:

$$u(r) = A \exp\left(-Br\right) - \frac{C}{r^6}, \tag{2.46}$$

where A, B and C are empirical constants.

In practicality, force field is always a package including certain function form and parameters for each interaction. Force fields usually used in MD simulations include OPLS [52], AMBER [53], CHARMM [54] and GROMOS [55].

CHAPTER 3

PEPTIDE-MEMBRANE INTERACTION: IONS AND LIPID COMPOSITION

Amyloid diseases, which include Alzheimer's and Parkinson's, are characterized by the aggregation of peptides into soluble oligomers and fibrils [9, 30, 56–59]. Interactions of these aggregates with the cell membrane accounts for an important mechanism of cell toxicity wherein annular shaped oligomers can form pores in lipid bilayers and amyloid fibrils can induce lipid loss through a detergent-like mechanism [4–7, 9, 60]. These types of damage increase the vulnerability of neurons, and they can lead to cell death [10, 11]. Several factors have been shown to affect toxicity by amyloid peptides including lipid composition and the presence of ions in the solution [12–16, 18, 19, 21–24, 61, 62]. Currently, the molecular mechanisms accounting for amyloid-membrane interactions remain poorly understood and further studies are needed to rationalize how these mechanisms are affected by lipid composition, ions and pH. This fundamental knowledge is critical to better understand cell toxicity, and it may enable rational design of new therapeutics to treat amyloid disease.

Insights into amyloid toxicity are often obtained experimentally by studying peptide aggregation in the presence of vesicles, monolayers, supported or suspended lipid membranes [20, 21, 63–65]. Specifically, vesicles can contribute to either increase or decrease the rate of aggregation [13, 63, 66–69]. Decreased rates of aggregation have been related to the sequestration of peptides into the interior of the bilayer where, surrounded by lipids, it is more difficult for peptides to attract each other [70]. In some cases, increased rates of aggregation have been related to the ability of some lipids to attract and align peptides at the membrane surface facilitating the formation of amyloid fibrils [12, 13]. Accordingly, anionic vesicles have been shown

to induce peptide ordering at the bilayer surface and to increase the rate of amyloid fibril formation [13, 71]. These results have been reproduces for different types of anionic lipids as well as peptide sequences highlighting the importance of electrostatic interactions in amyloid-bilayer binding. At first sight it might appear counterintuitive that the rate of aggregation of negatively charged peptides, e.g., the amyloid-β (Aβ) protein, increases in the presence of anionic membranes. However, Aβ has several positive residues distributed along its amino acid sequence, which can be attracted to the bilayer while keeping negative residues at a certain distance from it [64, 72]. This counterintuitive behavior of Aβ was highlighted by Moore et al [65], wherein this peptide was shown to bind positively, negatively, as well as non-polar surfaces because of its complex distribution of charged and non-polar residues. In the same vein, binding of α-synuclein to membrane was shown to be driven by electrostatic interactions between positive lysine residues and lipid head groups [73]. Additionally, as mentioned before that soluble oligomers formed in the early stage of the aggregation of amyloid have been proposed to be more accountable to the cell toxicity, the study on the initial aggregates under membranous environment is crucial to unveil the mechanism accounting for the cell toxicity. These initial aggregates are hard to study by experiments due to their transient nature.

The importance of electrostatic interactions is further highlighted by the role played by calcium ions in amyloid aggregation at the surface of lipid membranes. Experimental studies consistently report that, the addition of Ca^{2+} ions to solutions containing anionic bilayers promotes the aggregation of amyloid peptides independently of their net charge [7, 17, 61]. This has been related to a reduction in the peptide-membrane binding affinity and/or calcium's ability to promote the stability of lipid membranes, which may inhibit the sequestration of peptides into the bilayer [7, 17, 61, 74]. Calcium's role in regulating the formation of lipid domains and recruitment of ionic lipids to the membrane surface has also been proposed as

mechanisms to explain its effect in aggregation [75–77]. In contrast to these results, an increase in the peptide-membrane binding affinity has also been reported for the Aβ peptide via the formation of "Ca^{2+} bridges" between negative glutamic acid (E) residues and negative phosphate moieties of lipid head groups [18, 78, 79]. The effect of calcium in promoting aggregation close to anionic membrane has, however, been observed even for peptides that do not have negative residues, e.g., amylin. This suggests mechanisms of action that do not depend on the presence of negative residues in the peptide sequence.

Computational studies have been providing important insights into the mechanism of amyloid-membrane binding [19,80–84]. Recent studies have shown that the non-polar segments of amyloid peptides, e.g., the C-terminal and the central-hydrophobic-core of Aβ, are the first to be inserted into the bilayer interior [85]. This highlights the importance of hydrophobic interactions. In these simulations, amyloid peptides cause the thickness of the bilayer and the area per lipid to reduce significantly wherein the fatty acid tail of lipids become strongly disordered [80,85,86]. Despite these important insights, most simulations have not been designed to study the attraction of amyloid to lipid membranes as they are performed with peptides already deposited on the bilayer surface. For the latter study, a large fraction of the simulation box needs to be dedicated to the solvent, which is computationally expensive but necessary to understand how peptides in solution approach the membrane.

Here, we use molecular dynamics simulations to provide atomic insights into the interactions accounting for the attraction and binding of individual amyloid-like peptides, i.e., monomers, to lipid bilayers and the effect of calcium ions in this process. As shown in Figure 3.1, a large fraction of the simulation box dedicated to the solvent in our simulations. We show that the attraction of peptides to membranes is dominated by electrostatic interactions between *positive* residues and *negative* phosphate groups of lipids. Moreover, when the peptide is at close proximity

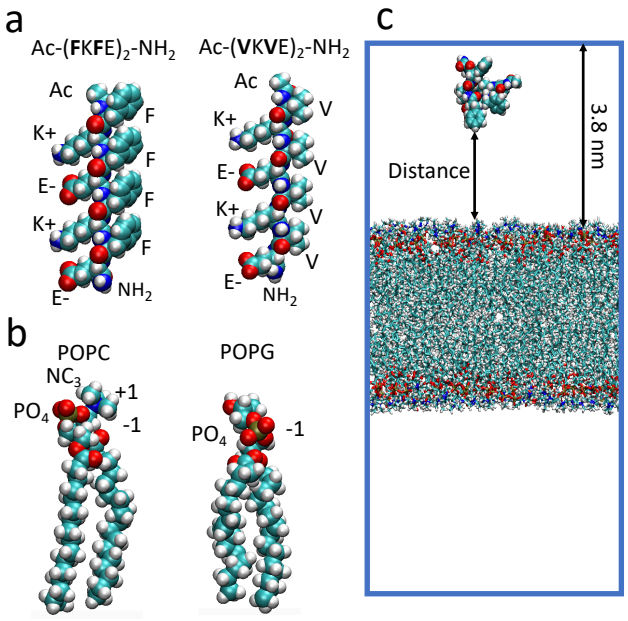

Figure 3.1 Atomic representation of (a) peptide and (b) lipids studied in the work. Cyan, white, blue, red, and orange represent carbon, hydrogen, nitrogen, oxygen, and phosphate atoms, respectively. (c) Schematic representation of the simulation box and the minimum distance between peptide and lipid bilayer.

from the membrane, hydrophobicity drives the burial of non-polar residues into the bilayer, which produces strong binding in our simulations. These modes of interaction were observed for both zwitterionic and anionic bilayers wherein the attraction of positive residues is more pronounced in the latter membrane. We also show that Ca^{2+} ions bind strongly to phosphate groups of the lipid bilayer [87, 88] shielding electrostatic interactions between positive residues and the membrane. This accounts for a significantly weaker attraction of peptides to membranes in our simulations. Strong binding of peptides to lipid membranes occur less frequently in the presence of calcium ions and they involve the formation of "Ca^{2+} bridges" between negative E residues and negative phosphate moieties of lipids.

3.1 Model and Simulation Protocols

Two peptide sequences with alternating non-polar and charged residues are studied, i.e., Ac-(**F**K**F**E)$_2$-NH$_2$ and Ac-(**V**K**V**E)$_2$-NH$_2$–see Figure 3.1a [89, 90]. These

amphipathic peptides differ in the nature of their non-polar residues with the sequence containing phenylalanine (**F**) being more hydrophobic than the one with valine (**V**). These sequences are neutral as the number of positively charged lysine (K) and negatively charged glutamic acid residues are the same. Experimental studies have shown that these peptides self-assembly forming cross-β structures that resemble amyloid fibrils [89, 90]. CHARMM-GUI is used to build four different lipid bilayers [91–93] wherein our reference bilayer is made of 64 zwitterionic phosphatidylcholine (i.e., POPC) lipids in each leaflet. Three negatively charged membranes are studied by replacing POPC with 1-palmitoyl-2-oleoyl-*sn*-glycero-3-phospho-(1'-rac-glycerol) (i.e., POPG) to account for bilayers with 10%, 30%, and 100% anionic lipids. These bilayers will be referred to as PC, PG_{10}, PG_{30} and PG. Atomic structures and charges of POPC and POPG are shown in Figure 3.1b. To neutralize the charge of anionic bilayer, sodium ions are added to the solution as this ion does not bind strongly to lipids or peptide atoms [87, 88]. To study the effect of Ca^{2+} on peptide-bilayer binding, simulations were performed in the presence and absence of $CaCl_2$ in the solution at an approximate concentration of 350 mM. Notice that the concentration of calcium in the extracellular space is of the order of 1-2 mM, which accounts for the presence of less than one calcium ion in a typical simulation box of size $7\times7\times7$ nm^3. Thus, following common practice in molecular dynamics simulations, we are using a much higher concentration of calcium [87,88]. A summary of the different simulations performed in this work is provided in Table 3.1. Notice that multiple simulations were performed for each lipid composition and solvent condition with peptide initiates from different positions in the simulation box to gather enough statistics. All the quantities reported in this work were computed from all the repeated simulations.

Simulations are performed using GROMACS-2018 [94] with the CHARMM36m force field and the TIP3P water model [95]. To model $CaCl_2$, we use the standard CHARMM36m force field as well as the NBFIX correction. The leap-frog algorithm

Table 3.1 Summary of Simulations Performed in Chapter 3

Peptide	Lipid composition	Num. Na	Num. Ca	Num. of traj.	Sim. time
F	POPC	–	–	5	3 μs
		–	61	5	3 μs
	9:1 POPC:POPG	14	–	5	0.77 μs
		14	61	5	1.1 μs
	7:3 POPC:POPG	38	–	5	0.86 μs
		38	61	5	1.03 μs
	POPG	128	–	5	1 μs
		128	61	5	0.9 μs
V	POPC	–	–	5	3 μs

is used to integrate the equations of motion with a 2 fs time step. Simulations are conducted in the NPT ensemble using the Nosé-Hoover thermostat (310 K and τ_T=1 ps) [49,96] and the semi-isotropic Parrinello-Rahman barostat (1 bar and τ_P=5 ps) [97]. A Verlet-list is used to account for first-neighbors and the cut-off for van der Walls interactions is set at 1.2 nm. Electrostatic interactions are treated using the Smooth Particle Mesh Ewald scheme with a grid spacing of 0.12 nm and a 1.2 nm real-space cutoff [98].

3.2 Results and Discussion

3.2.1 Zwitterionic bilayer

A schematic representation of the simulation box and the shortest distance ξ between lipid and peptide atoms is shown in Figure 3.1c. The time dependence of ξ is depicted in Figs.3.2a,b for two trajectories simulated using the F-sequence and the PC bilayer in the absence of $CaCl_2$. In panel a, the peptide undergoes several binding-unbinding events and in panel b it binds strongly to the membrane after an induction time of 200

ns. A characteristic configuration of the peptide in this strong binding state is shown in the inset of panel b wherein non-polar phenylalanine side chains are buried within the dry core of the bilayer and charged side chains are facing the solvent interface. In three out of the five 600 ns simulations performed for this system, the peptide binds strongly to the bilayer after 200, 250, and 500 ns. For the less hydrophobic V-sequence, the peptide binds stongly to the bilayer after 200 ns in only one of the five simulations. In the presence of Ca^{2+} ions, the F-peptide did not bind strongly to the bilayer in any of the five simulations. This is an indication that anchorage of peptides to the bilayer can be reduced by decreasing the hydrophobic character of the sequence and by adding ions to the solution.

To quantify peptide-bilayer interactions, all the simulations are identified as two regions referred to as induction time and strong binding. All the analysis in this work is run on these two regions separately and takes all the replicas into account. Figure 3.2c depicts histograms of ξ computed during the induction time of our simulations. These histograms exhibit three main peaks with maxima at 0.17 nm, 0.21 nm, and 0.47 nm. The first two peaks are characterized by configurations in which atoms of several residues are in direct contact with lipids in the bilayer whereas the peptide remains mainly solvated in the third peak. Thus, the minimum between second and third peaks, i.e., ξ_{cutoff} =0.325 nm, can used as a cut-off to discriminate between membrane bound and unbound states of the peptide. Histograms of simulations performed using F- and V- sequences in the absence of ions differ mainly in the first two peaks which are less pronounced for the less hydrophobic V- peptide. When $CaCl_2$ is added to the solution, the first two peaks of the F-sequence become significantly less pronounced and the probability of finding the peptide at ξ increases with increasing ξ. This suggests that $CaCl_2$ renders the zwitterionic bilayer repulsive to the peptide. The table in Figure 3.2d summarizes these results by showing the percentage of peptide-bilayer bound states of our simulations. This percentage is

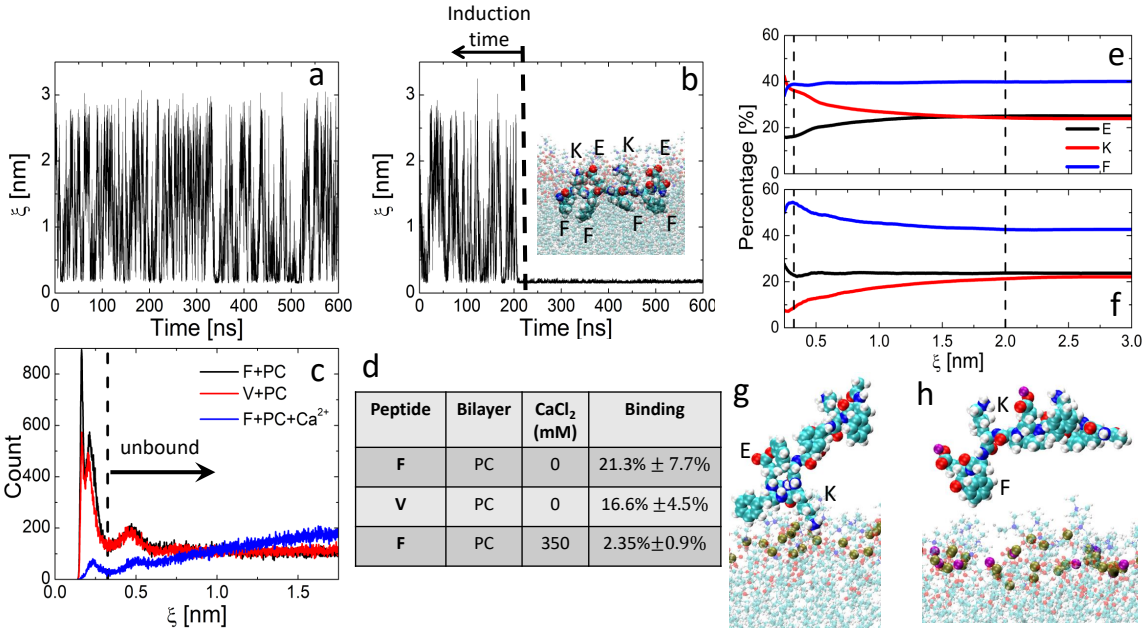

Peptide	Bilayer	$CaCl_2$ (mM)	Binding
F	PC	0	21.3% ± 7.7%
V	PC	0	16.6% ±4.5%
F	PC	350	2.35%±0.9%

Figure 3.2 Peptide binding to zwitterionic (PC) bilayers. Time dependence of peptide-bilayer distance for simulations performed using F-peptide showing (a) without and (b) with strong binding. Inset of panel b shows a configuration in which the peptide is bound strongly to the bilayer with F side chains buried within the lipid tail. (c) Distance distribution computed during the induction time of simulations performed using F- and V- peptides in the absence and presence of 350 mM of $CalCl_2$. (d) Percentage of time F- and V- peptides are bound to the bilayer in the absence and presence of 350 mM of $CaCl_2$. Percentage of bound states at a distance ξ for which E, K, or F residues are closer to the membrane in the (e) absence and (f) presence of $CaCl_2$. Characteristic configurations showing (g) a lysine side chain being attracted to phosphate atoms (in beige) in the absence of $CaCl_2$, and (h) calcium ions (in purple) being attracted to phosphate atom and repelling lysine side chains.

computed from the histogram in Figure 3.2c using ξ_{cutoff}. Reducing the hydrophobic character of the peptide decreases the percentage of bound states in the simulation from 21 % for phenylalanine to 16 % for valine. Adding $CaCl_2$ to the solution has an even stronger effect as it reduces the population of binding events to 2 %.

Figure 3.2e–f provides insights into the chemical groups that are attracted to the bilayer by tracking the type of residues that are closest to the membrane at a distance ξ. For large peptide-bilayer distances (i.e., $\xi \geq 2$ nm), 40% of all configurations in our trajectories have non-polar residues (i.e., F) closer to the membrane. Configurations in which positive (K) and negative (E) residues are closer to the bilayer account for

25% and 25%, respectively, of all frames. The remaining 10% of frames corresponds to configurations in which the N-terminal (acetyl group) is the closest chemical group to the bilayer. These numbers are mostly consistent with the percentage of F (i.e., 44%), E (22%), and K (22%) amino acids in the peptide sequence and they reflect a situation in which the peptide is not interacting with the bilayer.

In the absence of $CaCl_2$ (see Figure 3.2e) and as ξ decreases, the percentage of K-configurations, i.e., configuration in which K is the closest residue to the membrane, increases significantly from 25% to 35%–see red line. Concurrently, E-configurations (black line) become proportionally less populated whereas the percentage of F-configurations (blue line) is mostly unaffected by the minimal peptide-bilayer distance. This highlights the importance of electrostatics in peptide-bilayer interactions wherein positive and negative amino acids are attracted to and repelled from the bilayer, respectively. A characteristic configuration illustrating this type of peptide-bilayer interaction is shown in Figure 3.2g wherein a positive K residue is attracted to negative phosphate atoms of POPC (large beige spheres), which repel negative E residues.

In the presence of $CaCl_2$ (Figure 3.2f) and as ξ decreases, the percentage of K-configurations decreases from 22% to 9% whereas the number of E-configurations remain mostly insensitive to the peptide-bilayer distance. Concurrently, the percentage of F-configurations increase from 40% to 55%. A characteristic configuration wherein F residues are close to the bilayer is shown in Figure 3.2h. This figure also depicts Ca^{2+} ions (purple spheres), which are attracted to negative phosphate atoms (beige) of POPC lipids. We find that on average every four POPC lipids becomes bounded to one Ca^{2+} ion consistent with other studies [87,88]. This renders the bilayer positively charged leading it to repel K residues and accounting for fewer K-configurations in the trajectory. Now, to explain the increased percentage of F-configuration with decreasing ξ in panel f requires noticing that non-polar and charged residues face

opposite sides of our amphipathic peptides–see Figure 3.1a. Thus, repulsion of K residues leaves the non-polar side of the peptide facing the bilayer, which accounts for the increased percentage of F-configurations with decreasing ξ.

Recent studies have suggested that the binding strength of Ca^{2+} to lipid bilayers may be overestimated in most force fields [88]. Accordingly, corrections to the Ca^{2+} force field have been proposed including the electronic continuum correction with rescaling (ECCR) [99] and the pair-specific non-bound fixed optimized Lennard-Jones parameters (NBFIX) [100]. Since binding of calcium to the bilayer is critical to explain effects of this ion on peptide-membrane interactions, we also performed simulations with the NBFIX force field. It shows that the percentage of peptide-bilayer bound states in the presence of Ca^{2+} ions modeled with the NBFIX force field is $11\%\pm1.7\%$. Thus, the effect of $CaCl_2$ in discouraging binding of peptides to the bilayer is robust in simulations although its magnitude may depend on force field.

Figure 3.3a shows that the effect of the positive amino moiety of POPC lipids play a lesser role in attracting peptides to the bilayer as it is exposed to the solvent and, thus, screened by it. In this figure, the average cosine of the angle between the dipole moment of water and the z-axis is plotted as a function of the z-coordinate of water. At distances larger than 1 nm, which corresponds to approximately three layers of water molecules, the average cosine is zero as water molecules do not have a preferential direction. Close to the bilayer, the net orientation of water molecules is consistent with their role in screening positive charges on the bilayer, i.e., the average dipole moment points towards the membrane surface–as shown by red arrows in the inset of Figure 3.3a. Thus, interactions close the bilayer interface are dominated by electrostatic interactions between the negative phosphate moiety of POPC lipids and charged species in the solution. This moiety attracts positive residues of the peptide as well as cations. This latter renders the membrane positive and leads to

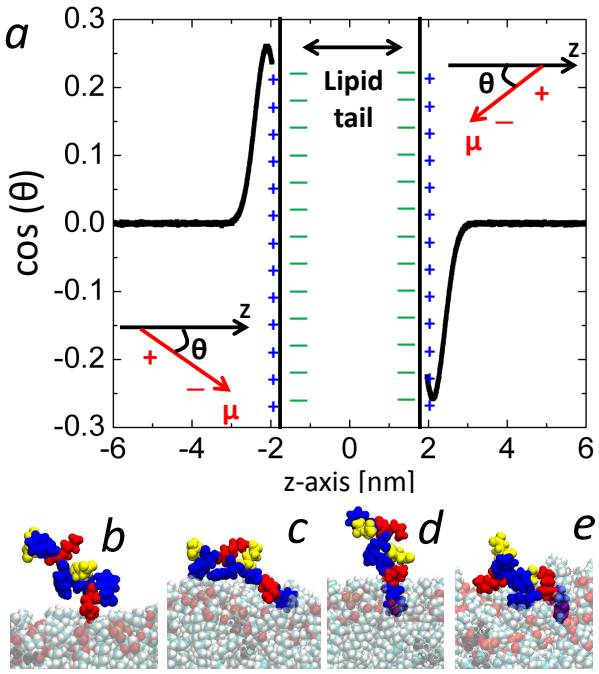

Figure 3.3 Screening of positive amino groups by water molecules and burial of non-polar residues into the bilayer surface. (a) Average cosine of the angle θ between dipole moment μ of water and z-axis as a function of the z-coordinate of water molecules. The space occupied by lipid tails as well as positive (blue) and negative (green) moieties of head groups are shown schematically. The orientation of μ with respect to the bilayer surface is shown in red. (b-e) Burial of non-polar residues (in blue) into the membrane. Red and yellow colors are used to represent lysine and glutamic amino acids. These figures correspond to simulations performed for the F-peptide in the absence of $CaCl_2$.

the repulsion of positive residues. In the absence of cations, the negative phosphate group of POPC attracts positive residues.

Our simulations also show that, when at close proximity to the lipid surface, non-polar residues can bury themselves into the dry core of bilayer–see inset of Figure 3.1b. This accounts for strong peptide-bilayer binding which leaves the peptide anchored onto the membrane surface. A sequence of events leading to hydrophobic burial is shown in Figure 3.3b-e. Initially, the peptide is attracted to membrane surface via one of its lysine residue (panel b) followed by the insertion of a non-polar residue into the lipid bilayer–panel b. The latter residue acts like an anchor keeping the peptide close to the surface for an extended period of time–panel d. This allows other

non-polar residues to embed themselves into the bilayer–panel e. Since residues that are more hydrophobic can penetrate the bilayer more easily, sequences with a higher hydrophobic character are more prone to bind strongly to the bilayer as shown in Figure 3.2d.

3.2.2 Anionic bilayer

To further highlight the role of electrostatic interactions in peptide-bilayer binding, we study effects of anionic lipids in Figure 3.4. In panel *a*, percentages of binding events are shown for PC, PG_{10}, and PG_{30} bilayers in the absence (black symbols) and presence (red symbols) of $CaCl_2$. These quantities were computed from the induction time of the five simulations performed using the F-peptide. Replacing 10% of POPC lipids with anionic POPG does not account for a large change in the population of bound states. However, an increase of almost 10% in the population of bound states is observed when 30% of POPC lipids are replaced with POPG. Moreover, in four out of five trajectories, peptides bind strongly to PG_{30} bilayers before 100 ns. For zwitterionic PC bilayer (i.e., Figure 3.2), strong binding was observed in only three out of five trajectories after 250 ns. This highlights significantly stronger attraction and binding of peptides to anionic bilayers. To rationalize this effect of anionic lipids, Figs.3.4b,c show the percentage of frames in which positive (K) and negative (E) residues are closer to the membrane than any other residues. For PG_{30} bilayers (dashed black lines), K and E residues are significantly closer to and far from the membrane, respectively, when compared to PC bilayers (full black lines). This is consistent with positive residues being more strongly attracted to negative moieties of anionic than zwitterionic lipids.

The addition of $CaCl_2$ to the solution accounts for a strong reduction (by almost 20%) in the percentage of bound states for both zwitterionic and anionic membranes–see Figure 3.4a. Panel b of this figure shows that the percentage of frames in which

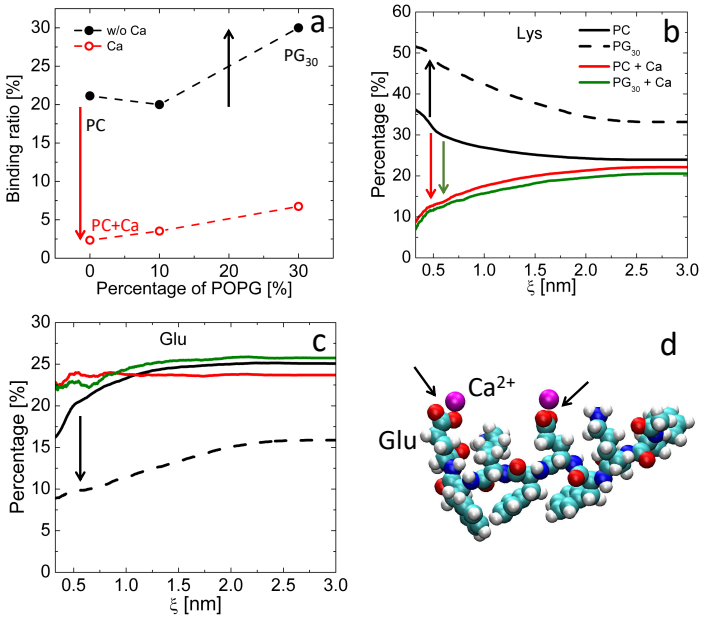

Figure 3.4 Binding of peptides to anionic bilayers. (a) Percentage of time that the F-peptide peptide binds to PC, PG_{10} and PG_{30} bilayers. Arrows highlight effects of anionic lipid (in black) and Ca^{2+} ions (in red). Percentage of frames in our simulations for which (b) lysine and (c) glutamic acid are closest to the membrane than other residues at a distance ξ. Changes with respect to our reference simulation (PC bilayer) is shown by arrows. (d) Characteristic configuration showing Ca^{2+} ions bound to glutamic acid.

positive K residues are closest to the membrane decreases as ξ decreases for both zwitterionic PC (red lines) and anionic PG_{30} (green lines) bilayers. This implies that, in the presence of Ca^{+2} ions, K residues are repelled from the membrane. This is due to the deposition of Ca^{2+} ions to the bilayer (see Figure 3.2h), which accounts for a membrane surface that has a net positive charge. In our simulations, net charges of PC and PG_{30} bilayers due to the deposition of calcium ions are 29e and 13e, respectively. Surprisingly, panel c shows that, in the presence of Ca^{2+} ions, the percentage of frames in which negative E residues are closer to the membrane than other residues is not strongly affected by the distance ξ for both zwitterionic PC (red line) and anionic PG_{30} (green line) membranes. This can be explained by the binding of Ca^{2+} ions to negative E residues in the solution–see Figure 3.4d. This screens the electrostatic interaction between E residues and the positive membrane.

3.2.3 Strong peptide-membrane binding

In the absence of Ca^{2+} ions, the peptide binds the membrane strongly in three and four of the five simulations performed using zwitterionic (i.e., PC) and anionic (i.e., PG_{30}) bilayers, respectively. Strong binding for these systems is characterized by the burial of non-polar side chains of the peptide within the hydrophobic tails of lipids while charged residues remain partially exposed to the solvent. To characterize this scenario, Figure 3.5a depicts density distributions of non-polar F (in black) and negative E (in red) side chains computed for configurations where the peptide is bound strongly to the membrane. Using the maximum in the density distribution of phosphate atoms as our reference (blue dashed line), this figure shows that F and E residues are located within the lipid tail and exposed to the solvent, respectively. A representative configuration depicting strong binding is shown in the inset of Figure 3.5a.

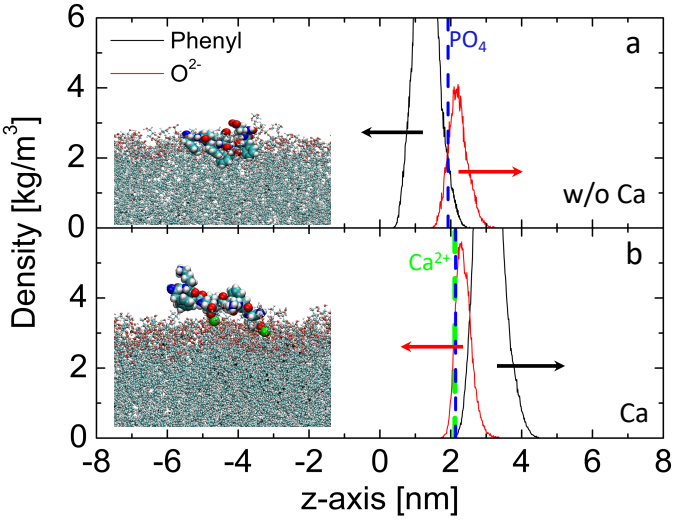

Figure 3.5 Density distributions of phenylalanine (black) and glutamic acid (red) in the (a) absence of $CaCl_2$, and (b) presence of $CaCl_2$ for configuration in which the peptide is bound strongly to the bilayer. Characteristic configurations are shown in the inset with calcium ions being represented in green.

In the presence of Ca^{2+} ions, the peptide did not bind strongly to any of the simulations performed using PC or PG_{10} bilayers. However, strong binding was observed in one of the five simulations performed using PG_{30} bilayers. We also

performed simulations in bilayers made from 100% POPG lipids in the presence of Ca^{2+} ions and strong binding was observed in all five simulations. This type of strong binding in the presence of calcium is characterized by the formation of two "Ca^{2+} bridges" between E residues and phosphate moieties of lipid head groups. Density distributions of F (in black) and E (in red) side chains are shown in Figure 3.5b. In this figure, we also show positions of maximum densities of calcium ions (in dashed green) and phosphate atoms (in dashed blue). These positions coincide indicating strong binding between these species. Moreover, the distribution of E residues overlaps partially with distributions of both calcium ions and phosphate atoms suggesting "Ca^{2+} bridges". The inset of Figure 3.5b provides an example of strong binding configuration in the presence of ions.

"Ca^{2+} bridge" between negative E residues and phosphate atoms was also reported in simulations performed using the Aβ protein [79]. In our simulations, calcium decreased significantly the peptide-membrane binding affinity (see Figure 3.4a), which is consistent with studies suggesting that Ca^{2+} ions prevent the insertion of peptides into the bilayer [74]. Importantly, in configurations where the peptide is bound strongly to the membrane via a "Ca^{2+} bridge, F side chains are exposed to the solvent–see Figure 3.5b. We speculate that these exposed patches of non-polar residues could behave as *hot spots* for attracting peptides and catalysing aggregation.

3.3 Conclusions

In summary, we performed extensive all-atom molecular dynamics simulations to study the interaction of amphipathic peptides with phospholipid bilayers. We show that both electrostatic and hydrophobic interactions contribute to binding. Specifically, positive residues are attracted to negatively charged phosphate moieties of lipid head groups. Moreover, when at close proximity from the membrane, hydrophobicity drives the burial of non-polar residues into the bilayer. This

produces strong binding of peptides to the bilayer. These mechanisms take place for both zwitterionic and anionic bilayers. For the latter membrane, the electrostatic attraction of positive residues is more pronounced than for the zwitterionic membrane. Accordingly, we observe stronger peptide-bilayer binding for anionic membranes compared to zwitterionic ones. We also show that Ca^{2+} ions are attracted to phosphate moieties of lipid head groups leaving the membrane with a net positive charge. This inhibits attraction of positive residues to the bilayer. Accordingly, the population of peptide-bilayer bound states is significantly less pronounced in our simulations containing $CaCl_2$ than in pure water. Strong binding of peptides to bilayers are also observed in simulations containing calcium but they occur less frequently than in simulations without calcium. They are driven by a "Ca^{2+} bridge" between negatively charge residues and phosphate moieties of lipids.

Mechanisms of interaction of antimicrobial peptides with lipid bilayers resemble those of amyloid peptides [101]. A vast majority of these peptides are cationic and some of them form α-helices when their positive residues bind phosphate moieties of lipid head groups. This leaves the non-polar side of the α-helix exposed to the solvent. Insertion of peptides into the membrane requires flipping the helix to enable hydrophobic residues to face the bilayer [102]. This membrane binding mechanism for antimicrobial peptides is very similar to the one outlined in this work for amyloid-like peptides. In particular, both mechanisms involve electrostatic attraction of peptides to the membrane surface followed by the insertion of non-polar residues into the bilayer. This suggests that general principles govern the interaction of peptides to lipid bilayers independently of amino acid sequence.

Effects of cations are critical to understand interactions of peptides with lipid bilayers in amyloid diseases. In particular, it has been reported that concentrations of Ca^{2+} are dysregulated in cells overexpressing amyloids [103], which is expected to affect the type and magnitude of membrane damage [17]. Our simulations show

that Ca^{2+} ions reduce significantly the attraction of peptides to the bilayer. This is consistent with experimental studies which have reported that calcium induces a shallower insertion of amyloid peptides into the bilayer causing less disruption of the membrane's hydrophobic core [7, 17, 61]. The main explanation of this phenomena in our simulations is the deposition of calcium into zwitterionic and anionic bilayers [87, 88], which shields the attraction of positive residues to negative phosphate moieties of lipids. This general electrostatic principle is, therefore, likely to affect the interaction of other peptide-membrane systems. Accordingly, membrane permeabilization by some antimicrobial peptides, including alamethicin [104] and gramicidin [105], is inhibited by calcium. Similarly, a recent study has shown that the attraction of actin filaments (which are negatively charged) to positive but not negative membranes is reversed when divalent ions (i.e., Mg^{2+}) are added to the solutions [106]. Furthermore, experimental studies consistently show that calcium favors Aβ aggregation in the presence of vesicles [17, 61]. Whereas our study does not address aggregation, we speculate that this effect of calcium can be explained by the reduced penetration of peptides into the bilayer where, surrounded by other lipids, they cannot interact with other peptides easily. However, further simulations are needed to confirm this proposed role of Ca^{2+} in aggregation. Notice that, in addition to calcium, free-lipids in solution may an also affect aggregation and the type of membrane damage caused by amyloids [107].

CHAPTER 4

PEPTIDE-MEMBRANE INTERACTION: AMINO ACID SEQUENCE

The interaction of amphipathic peptides with lipid membranes is related to the toxicity of amyloid proteins [9,11,108], the antimicrobial properties of certain peptides [109–111], and the ability of cell penetrating peptides (CPP) to be used in several biomedical applications including drug delivery systems [112, 113]. These peptides are made of polar residues that interact electrostatically with lipid head groups and non-polar side chains that become buried inside the dry membrane core via hydrophobic effects [102, 114]. Currently, it remains unknown how the position of charged and non-polar residues in the sequence affects the interaction of a peptide with the membrane. This type of knowledge is critical to optimize the design of peptides as well as to rationalize the broad scope of sequences known to interact with lipid membranes.

The interaction of peptides with lipid membranes is often study in experiments where peptides damage vesicles in solutions [20, 21, 63–65, 115]. These studies are performed by comparing leakage of vesicles varying in their lipid composition as well as by using different peptides in the presence and absence of cations in solution. Membranes with a higher content of anionic lipids are found to promote both amyloid aggregation into fibrils and membrane damage [13, 71, 82]. This highlights the importance of electrostatic interactions in attracting peptides to the vicinity of negatively charged lipids promoting the formation of amyloid fibrils [116–119]. Accordingly, most CPP and antimicrobial peptides are made of positive sequences with net charge greater than +2. Moreover, increasing the net charge of these sequences using point mutations increases the antimicrobial activity of these peptides [116,117]. Consistent with these studies, divalent cations (e.g., calcium) are attracted

and adsorbed onto lipid membranes [82, 87, 88, 114] . This causes positive moieties of peptides to be repelled from the positive lipid-calcium complex [114], which accounts for a significant reduction in pore formation on the membrane surface by amyloid peptides [7, 17, 61]. Also, the ability of antimicrobial peptides to damage red blood cells (i.e., hemolysis) was shown to depend on the position of positively charged residues in the sequence [118], implying that the sequence pattern can be as important as the net charge in accounting for peptide-membrane interactions. In addition to electrostatic interactions, a certain degree of hydrophobicity is also required to enable the adsorption of peptides onto the membrane surface [78, 118, 120–125]. However, increasing and decreasing the hydrophobicity of antimicrobial peptides beyond a given window was shown to reduce the ability of these peptides to damage lipid membranes.

Despite the important insights obtained from studies of membrane damage, it is important to highlight that the latter is affected not only by how peptides interact with lipid bilayers but also by how they interact with each other in the vicinity of membranes causing damages. Decoupling these effects is important to design sequences with specific function, e.g., as probes for organelles (e.g., mitochondria) that need to interact with lipid membrane without causing damages [126]. Computer simulations can used to study peptide-membrane interactions independently of how peptides damage the membrane.

Here, we perform a systematic study of the interaction of peptides with zwitterionic lipid membranes using all-atom molecular dynamics simulations. In particular, we investigate effects of the net charge, hydrophobicity, and sequence pattern of the peptide. We find that adding positive and negative residues to the amphipathic Ac-(FKFE)-NH_2 peptide increases and decreases, respectively, its affinity to the membrane. Moreover, the frequency with which a peptide encounters the membrane is also affected by the position of its positive residues in the peptide sequence. The latter affects the extend by which positive side chains are exposed

to the solvent and, thus, can be attracted to the membrane. We find that positive residues located close to both extremities of a peptide (i.e., C- and N-terminals) are more exposed to the solvent and, thus, encounter the membrane with a higher frequency. Peptide adsorption involves burying non-polar residues into the dry core of lipid bilayer. Accordingly, we find that amphipathic peptides made using non-polar residues that are highly hydrophobic (i.e., phenylalanine) are adsorbed in all our simulations as opposed to peptides made using alanine and valine. In the same vein, we observe that the position of non-polar residues in the peptide sequence affects its tendency to be adsorbed into the membrane. Sequences with phenylalanine at the extremity of the peptide sequence have a higher tendency to be adsorbed in our simulations.

4.1 Model and Simulation Protocols

To study peptide-membrane binding, we use variation of an amphipathic peptide wherein non-polar (i.e., phenylalanine **F**) and charged (i.e., positive lysine K

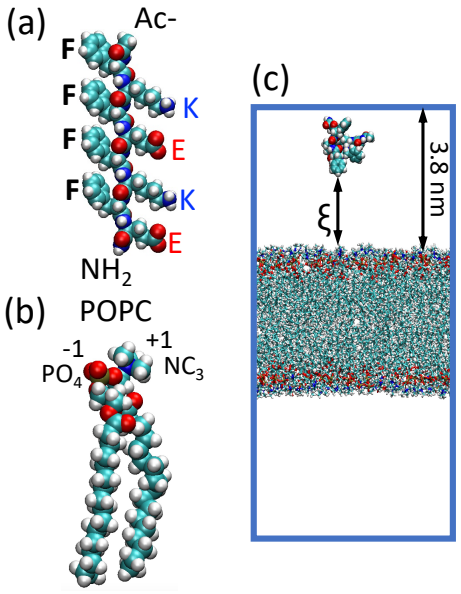

Figure 4.1 Atomic representation of (a) the reference peptide and (b) a POPC lipid. (c) Schematic representation of the simulation box and the minimum distance ξ between peptide and lipid bilayer.

and negative glutamic acid E) residues alternate along the sequence, i.e., Ac-(**F**K**F**E)$_2$-NH$_2$–see Figure 4.1a. This *reference* peptide was shown to self-assembly into amyloid-like fibril structures both in computer simulations and experiments [89, 90, 127]. Moreover, in all-atom simulations, it was shown to bind to lipid membranes in less than 1 μs making it suitable for computational studies [114]. We study membrane binding of fifteen peptides made by adding positive (K) or negative (E) amino acids to the N-terminus of the reference sequence or by scrambling the position of its residues. A comparative study of membrane binding by these peptides allowed us to provide insights into effects of net charge and position of charged residues on the peptide sequence. Membrane binding was also study for peptides where phenylalanine residues of the reference peptide were replaced with valine or alanine to provide insights into effects of non-polar side chains.

A zwitterionic bilayer made with 64 phosphatidylcholine (POPC) lipids in each leaflet is used to study membrane binding–see Figure 4.1b. This membrane was created using CHARMM-GUI [92,93,128] in a box of initial size $6.6 \times 6.6 \times 12$ nm^3. For each of the 15 peptides studied here, five to eight simulations were performed by adding the peptide randomly to the simulation box at a distance larger than 2 nm from the membrane. The system was solvated with TIP3P water molecules and sodium/chloride ions were added to the solution to neutralize charged peptides. These monovalent ions do not interact strongly with lipids and peptide [87, 88], and thus, their presence does not affect significantly peptide-membrane binding when compared to divalent ions [114], e.g., Ca^{2+}. Figure 4.1c shows a typical simulation box without water molecules and the minimal distance ξ between atoms of the peptide and the membrane, which is one of the main quantities computed in this study.

Simulations were performed using GROMACS-2020 [129] with the CHARMM36m force field [95]. Equations of motion were integrated using the leapfrog algorithm with a 2 fs time step. The Nóse-Hoover thermostat (310 K and $\tau_T = 1$ ps) [49, 96]

and the Parrinello-Rahman barostat (1 bar and $\tau_p = 5$ ps) [97] were used to perform simulations in the NPT ensemble. A Verlet-list was used to account for first-neighbors, wherein the cutoff for van der Waals interactions was set to be 1.2 nm. The Smooth Particle Mesh Ewald scheme with a grid spacing of 0.12 nm and a real space cutoff of 1.2 nm was used to treat electrostatic interactions [98].

4.2 Results and Discussion

4.2.1 Peptide-membrane simulation

Figure 4.2a shows the distance ξ between atoms of peptide and bilayer in the seven simulations performed using the reference peptide. In these trajectories, the peptide experiences several binding and unbinding events as ξ increases and decreases. In

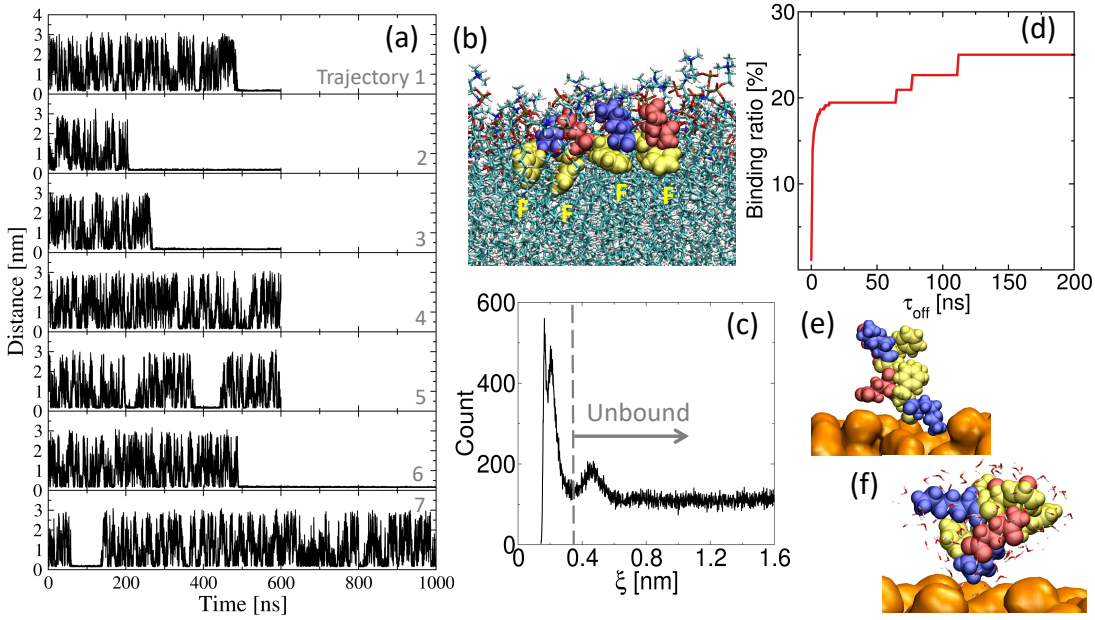

Figure 4.2 (a) The minimum distance ξ between atoms of peptides and bilayer in the seven simulations using the reference peptide. (b) A schematic representation of adsorbed peptide on membrane with non-polar residues (**F**) in yellow, positive ones (K) in blue and negative (E) in red. (c) The distribution of ξ computed from all the reversible trajectories of the reference peptide. ξ_{cutoff} is highlighted by a gray vertical dashed line. (d) The dependence of the binding ratio on τ_{off}. Characteristic conformations of binding frames with peptide in (e) direct contact and (f) remaining solvated.

four simulations (labeled 1,2,3, and 6), the peptide becomes adsorbed onto membrane surface after several hundreds of nanoseconds. In the adsorbed state, non-polar side chains are buried into the dry core of the bilayer and charged residues are exposed to the solvent–see panel b. In the time-frame of our simulations, the reference peptide does not get desorbed.

One of the goals of this study is to provide insights into the attraction of peptides to the membrane. Thus, a main focus is on the reversible binding-unbinding events that take place before the peptide get adsorbed. Since life-times of adsorbed and "reversible" bound states are very different, we distinguish between these states by tracking the binding-time of ever encounter of the peptide to the membrane. If this time is longer than a cut-off time τ_{off}, we consider the peptide to be adsorbed. Portions of the trajectory in which the peptide is adsorbed are not taken into account in the analysis. Figure 4.2c shows the distribution of ξ computed from all the reversible trajectories of the reference peptide using $\tau_{\text{off}} = 45$ ns. This distribution is characterized by three peaks at positions 0.17, 0.21 and 0.47 nm. In the first two peaks, the peptide is in direct contact with the bilayer (see panel e) whereas it remains solvated in the third broad peak–see panel f. Accordingly, we use the minimum between second and third peaks, i.e., $\xi_{\text{cutoff}} = 0.325$ nm, as a cut-off to define bound states of the peptide.

A main quantity computed in this study is the fraction of all reversible frames in which the peptide is found bound to the membrane. This quantity is referred to as the "binding ratio" of the peptide. The dependence of the latter on τ_{off} is shown in Figure 4.2d. Initially, the binding ratio increases abruptly and it saturates at $\tau_{\text{off}} \sim 20$ ns. For larger values of τ_{off}, the binding ratio increases in small steps highlighting the existence of only a small number of binding events that survive for a long time, i.e., adsorbed states. The comparison of the binding ratio for the different peptides studied in this work does not depend on the actual choice of τ_{off} except

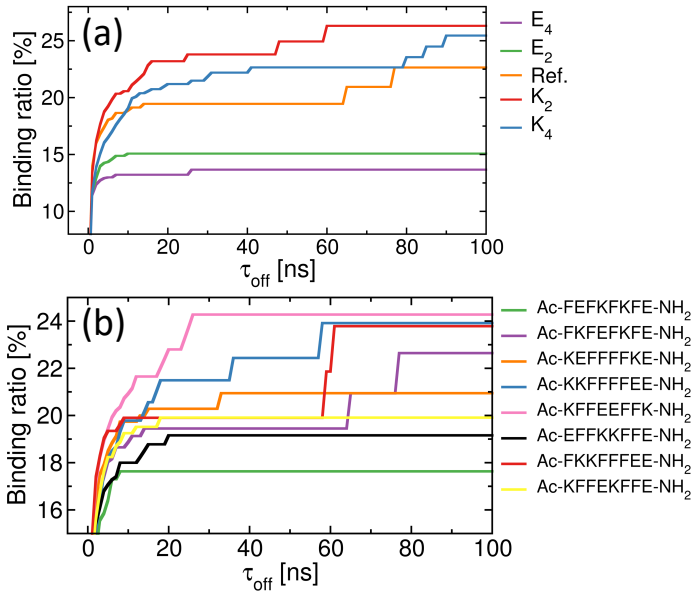

Figure 4.3 The dependence of the binding ratio on τ_{off} for (a) charged peptides and (b) neutral peptides. The *reference* peptide is shown in both panels.

for two sequences–see Figure 4.3. The latter cases involve a single event where the peptide remains bound to the membrane for more than 60 ns before detaching from it. Since our simulations are not long enough to sample these rare long binding events, binding ratios are computed using $\tau_{\text{off}} = 45$ ns. For all the simulated peptides in this study, the dependence of the "binding ratio" on τ_{off} is shown in Figure 4.3. Error bars correspond to statistical uncertainties estimated by computing the standard deviation of the binding ratio for (N-1) trajectories where one of the N different simulations was removed each time during the calculation.

4.2.2 Net peptide charge

In order to study how the net charge of a peptide affects its binding to the membrane, two or four glutamic acid (E) or lysine (K) amino acids are added to the N-terminal of the neutral Ac-$(FKFE)_2$-NH_2 peptide to account for net charges of -4, -2, +2, and +4, respectively– see Figure 4.4a. These peptides are referred to as E_4, E_2, K_2, and K_4, respectively. To compute binding ratios, five 1-μs trajectories were generated for E_4, E_2, and K_2 peptides. These peptides are mostly disordered in our simulations with

all residues adopting coil structures consistently. In one of the simulations performed with the K_4 peptide, it formed a transient β-hairpin structure that survived for 0.2 μs. This suggests that the K_4 peptide can adopt more complex conformations and, therefore, requires more thorough sampling. We generated eight 1-μs simulations for this peptide such that its average binding ratio changed by only 0.3% when segments of the trajectories where it adopts β-hairpin conformations are removed from the analysis. Thus, for all peptides studied in this work, secondary structure formation is not a factor affecting peptide-membrane binding. Note that because of the finite size of the simulation box, the shortest peptide (i.e., our reference peptide) can sample larger distances ξ from the membrane compared to E_4 and K_4 peptides. Binding ratios of the shortest peptides are, therefore, biased towards the unbound state compared

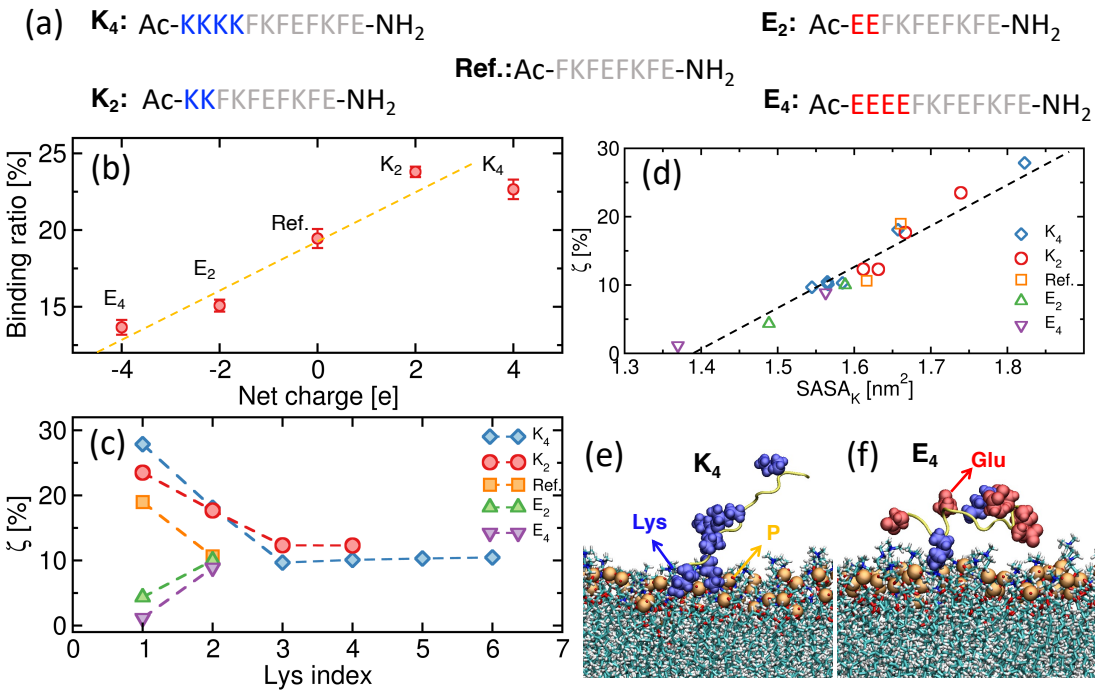

Figure 4.4 (a) The sequences of peptides K_4, K_2, reference, E_2 and E_4. (b) Binding ratios of the peptides with respect to their net charge. (c) The percentage ζ of reversible-bound frames wherein the i^{th} lysine is bound to a lipid. (d) The dependence of ζ on the $SASA_K$ for each lysine. Characteristic conformations of reversible-bound (e) K_4 and (f) E_4, wherein lysines are represented in blue, glutamic acids in red and phosphate groups in orange.

to E_4 and K_4. To correct for this finite size effect, only frames for which $\xi < 2.5$ nm (where 2.5 nm is a distance sampled by all peptides) are taken into account when computing for binding ratios.

Figure 4.4b shows the binding ratios of peptides with net charge varying from -4 to +4. This quantity increases monotonically with the net peptide charge up to +2. The binding ratio of K_4 is slightly lower than for K_2 but still higher than for the neutral reference peptide. This shows that positively charged peptides are more favorably attracted to lipid bilayers than neutral or negatively charged chains highlighting the importance of electrostatic interactions in this process. This trend is independent of our definition of binding ratio given by τ_{off}–see Figure 4.3. These results are consistent with previous studies on the reference peptide where negatively and positively charged side chains were shown to be repelled from and attracted to lipid membranes, respectively [114].

Figure 4.4c characterizes contributions of each positive residue to membrane binding by computing the percentage ζ of reversible-bound frames in the trajectory wherein the i^{th} lysine in the sequence is bound to a lipid. We consider that a lysine residue is bound to a lipid if the minimal atomic distance between these groups is less than 0.325 nm–see Figure 4.2c. The index i starts with the first lysine residue at the N-terminal. Figure 4.4c shows that for K_4 and K_2, the two lysines close to the N-terminal bind more frequently to lipids than the other positive residues defined by indices 3 to 6. For reference and anionic (i.e., E_2 and E_4) peptides, the first lysine in the sequence binds more and less frequently, respectively, than the second lysine.

To provide insight into the different contributions of lysine residues to membrane-binding, Figure 4.4d shows the dependence of ζ on the solvent accessible surface area SASA_{K} for each individual lysine. There is a clear positive correlation between these quantities, which shows that lysine residues that are more exposed to the solvent are also more likely to be attracted to the membrane. Since lysine residues that are

located closer to one of the extremities of a peptide are expected to have a larger $SASA_K$, they are also expected to be more attracted to the membrane. This explains the larger ζ for the first lysine residues of K_4, K_2, and the reference peptide. The lower ζ of the first lysine residue in anionic peptides (green and purple symbols in Figure 4.4c can be explained by its closer proximity to negative E side chains. These oppositely charged residues attract each other to form salt-bridges, which reduces $SASA_K$. Panels e and f show characteristic configurations of reversible-bound states for K_4 and E_4 peptides. In the former, lysine residues that are located closer to the N-terminal of the K_4 peptide are binding to negative phosphate atoms of the bilayer. In panel f, the lysine residue located closer to the N-terminal of the E_4 peptide is forming salt-bridges with negative glutamic acids and it is the second lysine that is binding to the membrane.

4.2.3 Peptide sequence

In summary, Figure 4.4 shows that membrane binding is affected by both the net charge of a peptide and the position of its positive residues in the amino acid sequence. The latter affects the extend by which positive residues are exposed to the solvent and, therefore, can interact with negative moieties of lipids. To better understand the relationship between exposure of positively charged residues and membrane binding, eight neutral sequences were designed by reordering the amino acids of the reference peptide. The two lysine residues are separated from each other by at least one residue for sequences A–E and placed consecutively in the amino acid sequence for peptides F–H, see Figure 4.5a. In these two sets of peptides, lysine residues are placed at different distances from the extremity of the peptide. The exposure of positive residues is quantified by computing the average solvent accessible surface area $SASA_K$ of both lysine residues over all reversible frames in which the peptide is not bound to the bilayer. This quantity varies from 2.99 nm^2 to 3.73 nm^2 and it correlates with the

position of lysine residues in the peptide sequence. In particular, sequences A, B and F that have lysine residues located at the extremities of the peptide exhibit the largest $SASA_K$ in our simulations. Conversely, peptides that have lysine residues located in the middle of the sequence, e.g., peptides E and H, exhibit the lowest $SASA_K$ values—see Figure 4.5b.

The dependence of the binding ratio on $SASA_K$ is outlined in Figure 4.5b using red and blue dashed lines for peptides A-E and F-H, respectively. For these neutral sequences, the binding ratio increases with $SASA_K$ wherein peptides with the lowest and highest $SASA_K$ are found bound to the bilayer 15% and 25% of the time, respectively. Interestingly, these binding ratio levels are comparable to the ones for anionic (i.e., peptides E_2 and E_4) and cationic (K_2 and K_4) peptides in Figure 4.5b, respectively. Thus, adding positive residues to the N-terminal of a given peptide can have the same effect on membrane binding as increasing its $SASA_K$ by moving existing lysine residues to its extremities. Similarly, adding negative residues to the N-terminal can have the same effect as reducing its $SASA_K$ by placing lysine residues in the middle of the peptide sequence.

In Figure 4.5b, peptides with the same $SASA_K$ have a higher binding ratio if their lysine residues are found consecutively in the peptide sequence (red dashed line in Figure 4.5b) as opposed to separated by other residues (blue line). This can be rationalized by noticing that both lysine residues are more likely to bind simultaneously to negative phosphate atoms of lipids if they are located close to each as opposed to separated by several residues. This accounts for bound states that have a longer life-time and, thus, a higher binding ratio. Evidence of increased lysine-phosphate binding for sequence F-H is provided by computing the number N_P of phosphate atoms bound to lysine residues. This quantity is shown as numbers in Figure 4.4b, which are computed by averaging over all frames in the reversible portions of the trajectories where the peptide is found bound to the membrane, i.e.,

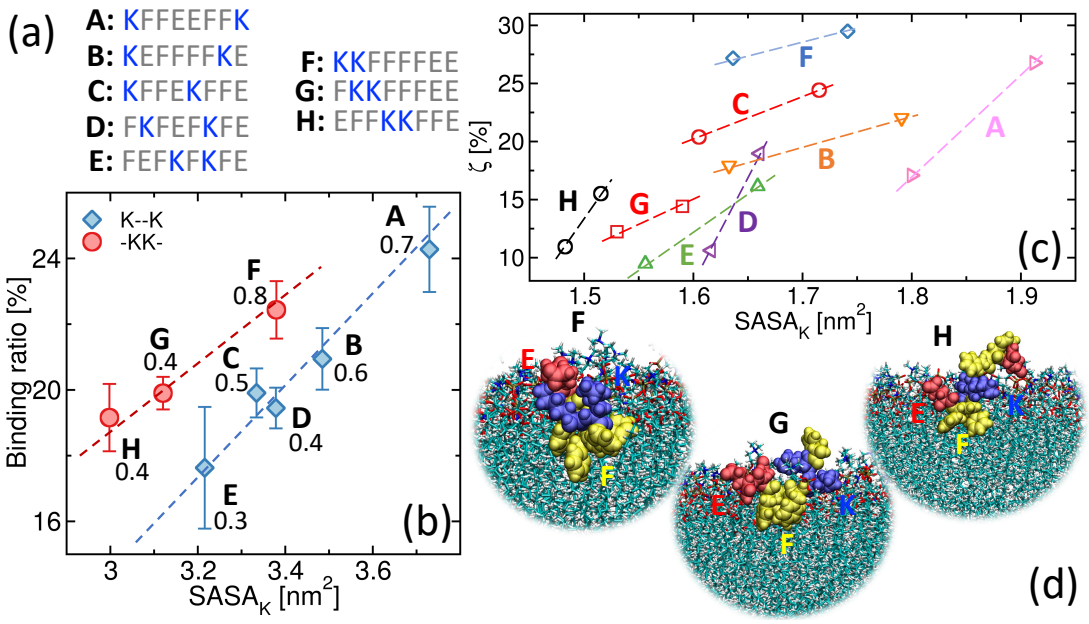

Figure 4.5 (a) The sequences of peptides A-H. (b) The dependence of binding ratio on $SASA_K$ for peptides A-H. N_P for each peptide is shown as a number in (b). (c) The dependence of ζ on the $SASA_K$ for each lysine. (d) Characteristic conformations of adsorbed peptides F, G and H.

$\xi < \xi_{cutoff}$. Peptide F binds to twice as many phosphate atoms as peptides D and C that have similar $SASA_K$. Similarly, peptide G has a higher N_P than peptide E.

Figure 4.5c depicts the percentage ζ of reversible-bound frames in which first and second lysine residues are bound to the membrane. In particular, ζ is shown as a function of $SASA_K$ computed for each lysine residue for peptides A–H. This figure shows that lysine residues contribute more to the bound state if they have a large $SASA_K$. For example, lysine residues of peptides A, B, C, and F have a larger $SASA_K$ and ζ than peptides D, E, G, and H. However, this correlation is not as well defined as for charged peptides in Figure 4.4d suggesting that other factors, e.g., other residues of the peptide, also play a role in accounting for bound states.

Out of the five 1-μs trajectories performed for each sequence, between 1 and 4 of them ended up with the peptide adsorbed onto the bilayer. Adsorbed states are stabilized by the burial of their non-polar residue in the dry bilayer core. This may involve the burial of four, three, or two phenylalanine residues as in the case of

Table 4.1 Percentage of Trajectories in Which the Peptide Becomes Adsorbed onto the Membrane

	A	B	C	**D**	**E**	F	**G**	H
Adso. (%)	40	40	60	**60**	**80**	60	**60**	20

peptides F, G, and H in Figure 4.5d. A trend can be highlighted from an analysis of the trajectories in which peptide A-H are adsorbed. In particular, sequences D, E, and G, which have a phenylalanine residue at one extremity (i.e., the N-terminal), are found to be adsorbed in at least 60% of the trajectories–see Table 4.1. In contrast, sequences A, B, C, F, and H with lysine or glutamic acid at their extremities are absorbed in 60% or less of the trajectories–see Table 4.1. This suggests that sequences that have phenylalaline residues at their extremities are more likely to be adsorbed onto the membrane. To test this ideas, five additional 1-μs simulations were performed with peptide Ac-FFKKFFEE-NH_2 which has two phenylalanine residues at the N-terminal.

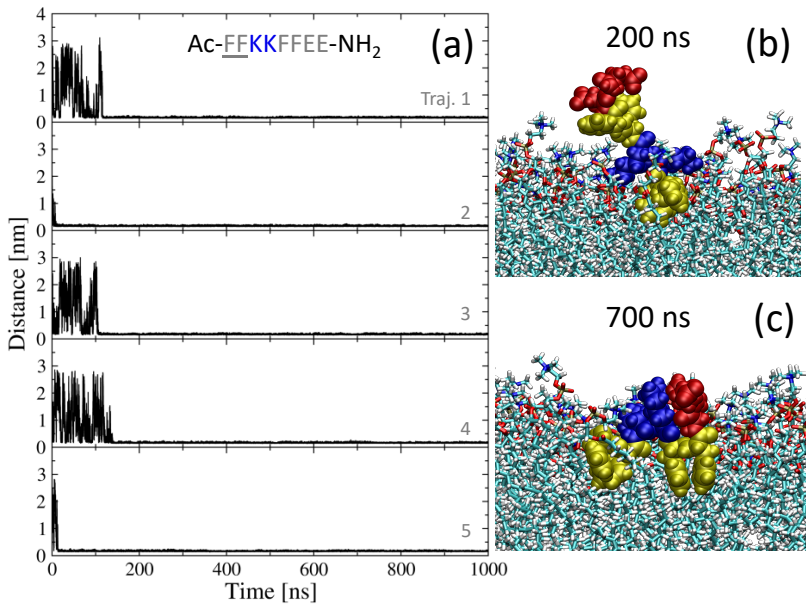

Figure 4.6 Minimal distance ξ between atoms of Ac-FFKKFFEE-NH_2 peptides and the bilayer in five independent trajectories. Characteristic conformations of adsorbed peptide at (b) 200 ns and (c) 700 ns for trajectory number one.

Figure 4.6a shows the minimal distance of this peptide in the different trajectories. The peptide becomes adsorbed to the membrane in less than 200 ns after only a few reversible binding events. The sequences of events leading to adsorption is shown in panels b-c for trajectory number one. At 200 ns (panel b), only the first two phenylalanine residues are embedded into the membrane. At 700 ns (panel c), all the four phenylalanine become anchored into the membrane. This corroborates the trend observed for peptides A-G but it needs to be validated with more trajectories and more peptide sequences.

4.2.4 Non-polar residues.

The role played by non-polar residues in peptide-membrane binding is investigated by replacing phenylalanine residues of the reference peptide (i.e., **F**) with less hydrophobic valine (i.e., **V**) and alanine (i.e., **A**) amino acids. We will refer to these sequences as **F**-, **V**- and **A**-peptides in this section. The binding ratio of these peptides computed from five 1-μs trajectories (as in previous sections) does not change significantly. It is 19% for both **F**- and **V**-peptides, and 20% for the A-peptide. This corroborates the idea that the attraction of peptides to the lipid membranes, which accounts for reversible bound states, is determined by charged residues and not non-polar amino acids. In contrast, the adsorbed state always involves the insertion of non-polar side chains into the hydrophobic interior of lipid bilayer. Accordingly, in four out of the seven trajectories for the **F**-peptide (see Figure 4.2a), the peptide becomes adsorbed into the membrane. For the less hydrophobic peptides, adsorption only takes place in one of the five 1-μs trajectories of the **V**-peptide and in none of the trajectories for the **A**-peptide. Thus, more hydrophobic peptides become anchored into the membrane with a lesser probability to unbind from it.

4.3 Conclusion

In this chapter, we explored effects of net charge, sequence pattern, and hydrophobicity on peptide-membrane binding using extensive all-atom molecular dynamics simulations. In a typical trajectory, the peptide that is initially located in the solvent undergoes several binding and unbinding events to the membrane before becoming adsorbed onto it. We show that the net charge of a peptide and the position of its charged residues in the sequence play an important role in accounting for the frequency of binding-unbinding events whereas non-polar residues affect peptide adsorption.

Our simulations are consistent with a previous study in which the presence of anionic lipids in the membrane increased the frequency of binding events showing that charged moieties of the peptide are attracted to negative phosphate atoms of lipid membranes. Accordingly, we find that adding positive and negative residues to a peptide increases and decreases, respectively, its affinity to the membrane. Moreover, the frequency with which a peptide encounters the membrane is affected by the position of its positive residues in the peptide sequence. The latter affects the extend by which positive side chains are exposed to the solvent and, thus, can interact with the membrane. We find that positive residues at a peptide's extremity (i.e., N- and C-terminal) are more exposed to the solvent and, thus, encounter the membrane with a higher frequency. In contrast, positive residues located in the middle of the peptide sequence tend to be less exposed to the solvent and to bind the lipid bilayer with lesser frequency.

The adsorption of a peptide to the membrane involves burying its non-polar residues into the dry core of the lipid bilayer. Accordingly, we find that amphipathic peptides made using non-polar residues that are less hydrophobic [130] (e.g, alanine and valine) are adsorbed into the membrane in a smaller number of trajectories than peptides made with more hydrophobic residues (e.g., phenylalanine). In the same

vein, we observe that the position of non-polar residues in the peptide sequence affects its tendency to be adsorbed into the membrane. Sequences with phenylalanine at the extremity of the peptide sequence have a higher tendency to be adsorbed in our simulations. The generality of this statement needs, however, to be further validated for other peptide sequences.

In summary, this current study provides insights into the mechanisms accounting for peptide-membrane binding and the role played by electrostatic and hydrophobic interactions in it. We anticipate that these insights will contribute to guide the design of new cell-penetrating-peptides and more efficient antimicrobial peptides. Moreover, our results are consistent with previous studies in which electrostatic interactions between peptide and membrane was altered by either adding divalent cations to the solution [61, 114] or by tuning the lipid composition rendering the membrane charged [17,19,114]. The latter is intimately liked to the selectivity of certain peptides for cell membranes with specific lipid composition, which is important in designing efficient antimicrobial peptides with low toxicity to host cells.

CHAPTER 5

AMYLOID-INDUCED MEMBRANE DAMAGE

Several amphipathic peptides are toxic and can cause cell death. They comprise amyloid peptides related to neurodegenerative diseases [9, 11, 108], antimicrobial peptides that enable organisms to defend themselves against biological threats [109–111], and artificially designed peptides [112, 113]. Extensive studies have been dedicated to provide insights into the mechanisms accounting for their toxicity, which include non-specific interactions with the cell membrane. These interactions enable lipids to be extracted from the bilayer (i.e., detergent-like mechanism of membrane damage) and ions to permeate the membrane via the formation of pore-like structures in its surface [68, 131–140]. An understanding of the pathways and interactions required to account for these types of membrane damage is critical to enable the development of therapeutics for amyloid diseases and to guide the design of novel antimicrobial peptides [141, 142].

Computer simulations have the potential to provide important new atomic insights into our understanding of membrane damage by amphipathic peptides [102,139,143]. However, all-atom simulations of peptide aggregation on the membrane surface and their penetration into the lipid bilayer are computationally demanding. Accordingly, the spontaneous formation of pores has only been simulated for α-helical peptides, which retain their secondary structure in the non-polar environment of the bilayer where inter-peptide hydrogen bonds are more stable than in solution [143]. These unbiased simulations have been performed at high temperatures wherein peptides penetrate the bilayer in a time-scale accessible to supercomputers (> 5 μs). The early stages of melittin aggregation has been captured by these simulations showing that this peptide forms transient pores in the bilayer [144–146]. Attempts to

simulate the spontaneous formation of pore-like structures by β-sheet peptides have not been successful so far. For example, low molecular weight oligomers from amyloid peptides [147–150] as well as β-sheets made from up to eight antimicrobial protegrin-1 peptides [151] did not penetrate the membrane in long all-atom simulations.

Evidence that membrane damage by amyloids and β-hairpin peptides can involve the formation of pores is provided by atomic force microscopy wherein the radius of pores is reported to be 1–2 nm [152–154]. Computationally, pore-like damages are often studied starting with peptides already inserted in the interior of the membrane to reduce the time-cost to simulate their aggregation and penetration in the bilayer [18, 155–164]. Accordingly, idealized pores from amyloid and β-hairpin antimicrobial peptides have been shown to be stable in all-atom simulations although they perturb lipids inside the bilayer [83, 151, 165–168]. In addition to pore formation, experimental studies have shown that amyloids and β-hairpin antimicrobial peptides can also cause damage by removing lipids from the membrane surface [132–135]. This phenomena has been related to the amphipathic nature of these peptides that can bind simultaneously non-polar and polar moieties of lipids as well as solvent molecules [7, 17, 61, 107]. Despite these insights, the sequence of events and the interactions accounting for both the removal of lipids from the bilayer and poration [169, 170] by amyloids and β-hairpin peptides remain mostly unknown.

In this chapter, we study membrane damage by a short amphipathic peptide with sequence alternating between non-polar and charged residues: Ac-$(FKFE)_2$-NH_2. This peptide self-assembles promptly into amyloid-like fibrils in solution making it suitable for computational studies [89, 90, 127]. Moreover, it was shown to bind strongly to lipid bilayers [114]. Here, all-atom simulations are used to study the sequence of events accounting for the self-assembly of membrane-bound Ac-$(FKFE)_2$-NH_2 peptides into β-sheets that spontaneously penetrate the membrane to form pore-like structures enabling solvent molecules to permeate the lipid bilayer.

The spontaneous removal of lipids from model membranes by Ac-$(FKFE)_2$-NH_2 peptides are also simulated providing one of the first atomic insights into this type of membrane damage. An analysis of these simulations shows that interactions of lipid tails with non-polar side chains play an important role in accounting for membrane damage. They enable lipids to be dragged from the bilayer and contribute to stabilize pore-like structures.

In our simulations, lipid removal takes place during the interaction of two membrane bound β-sheets as they emerge out of the membrane to bury their non-polar residues against each other. In this process, lipids that are strongly bound to non-polar residues are dragged out of the membrane. During the simulations, membrane bound β-sheets become twisted with one of their extremities partially penetrating the core of the bilayer. This partial penetration allowed peptides on opposite leaflets to interact and form a long transmembrane β-sheet initiating poration. The twist in β-sheets also allows water molecules to partially penetrate the membrane. In simulations where peptides are deposited on a single membrane leaflet, two β-sheets penetrate the membrane by tilting their polar faces towards these water molecules from opposite sides. This takes place while their non-polar residues remain bound to the acyl tail of lipids leading to the formation of pores with diameters ranging from 1.2 nm to 1.8 nm. Charged and non-polar residues of these β-sheets face the interior and exterior of pores, respectively. We also show that fibril-like structures do not perturb the membrane significantly in our simulations.

5.1 Model and Simulation Protocols

Molecular Dynamics Simulation. Amphipathic peptides with sequence that alternates strictly between non-polar (i.e., phenylalanine *F*) and charged amino acids (i.e., positive lysine *K*, and negative glutamic acid *E*), i.e., Ac-$(FKFE)_2$-NH_2, is used to study membrane damage. Experimental studies have shown that

this peptide self-assembles into amyloid fibrils forming supramolecular nanotubes [89, 90, 171]. In all-atom simulations, this peptide was also shown to self-assemble into amyloid-like fibrils and to interact with lipid membranes in a computationally accessible time-frame [114, 127]. Here, membrane damage is studied using three anionic membranes made by combining zwitterionic, i.e., 1-palmitoyl-2-oleoyl-*sn*-glycero-3-phosphocholine (POPC), 1,2-dipalmitoyl-*sn*-glycero-3-phosphocholine (DPPC), 1,2-dimyristoyl-*sn*-glycero-3-phosphocholine (DMPC), with anionic lipids, i.e., 1-palmitoyl-2-oleoyl-*sn*-glycero-3-phosphoglycerol (POPG), 1,2-dipalmitoyl-*sn*-glycero-3-phosphoglycerol (DPPG), 1,2-dimyristoyl-*sn*-glycero-3-phosphoglycerol (DMPG). The lipid composition of the three membranes studied here are 7:3 POPC:POPG, 7:3 DPPC:DPPG, and 7:3 DMPC:DMPG. These bilayers differ in the number of carbon atoms and the number of saturated bonds in their lipid tails, which is 18:0–16:1 for POPC:POPG, 16:0 for DPPC:DPPG, and 14:0 for DMPC:DMPG. This accounts for a gel-liquid transition temperature of $\sim$ 268 K, 297.3 K, and 315.6 K, respectively [172–174]. The CHARMM-GUI suite was used to build these anionic bilayers wherein sodium ions were added to the solution to account for systems with neutral charge [92, 93, 128].

Simulations starting with peptides deposited on the membrane surface were prepared in a step by step approach. In particular, up to three peptides were added to the solution and a short simulation was carried out until they became deposited on the membrane surface [114]. These process was repeated until the desired number of peptides on each membrane surface was attained. During preparation of the simulation and whenever needed, peptides were deleted from the membrane surface, e.g., to ensure an equal number of peptides on both membrane leaflet or to ensure that peptides are only deposited on one membrane leaflet. Simulation were also performed with a preformed fibrils or tetramers in solution. Table 5.1 provides a list of all simulations performed in this study. In Table 5.1, asterisk represents that

Table 5.1 Summary of Simulations Performed in Chapter 5

No.	Protein/quantity	Int. state	Bilayer	Temp.	Time	Remark
1	Monomer/18	Bound	POPC:POPG	350 K	5 μs	–
2	Monomer/18	Bound	POPC:POPG	350 K	5 μs	Poration
3	Monomer/18	Bound	POPC:POPG	350 K	5 μs	Poration
4	Oligomer[a]/4	Bound	POPC:POPG	320 K	4 μs	Poration
5	Oligomer[b]/2	Bound*	POPC:POPG	350 K	9 μs	Lipid loss
6	Oligomer[c]/3	Bound*	DPPC:DPPG	350 K	5 μs	Poration
7	Oligomer[d]/2	Bound*	DMPC:DMPG	350 K	1.5 μs	Poration
8	Oligomer[d]/2	Bound*	DMPC:DMPG	320 K	3 μs	Poration
9-12	Oligomer[e]/3	Unbound	POPC:POPG	350 K	1 μs	Lipid loss
13	Fibril[f]/2	Unbound	POPC:POPG	350 K	1 μs	–
14-17	Fibril[g]/1	Unbound	POPC:POPG	350 K	1 μs	–

proteins are bound to the same leaflet of the bilayer. (a) A trimer, tetramer and monomer on one leaflet and a hexamer and a tetramer on the other. (b) A dimer and pentamer. (c) Two trimers and a tetramer. (d) A dimer and heptamer. (e) Three tetramers. (f) Two cross-β structured fibrils consisting 14 peptides and 11 peptides respectively. (g) A cross-β structured fibril with 10 peptides.

Some of the simulations were performed on our local cluster using GROMACS-2020 [129] with the CHARMM36m force field and the TIP3P water model [95]. The leapfrog algorithm was used to integrate the equations of motion with a time step of 2 fs. Simulations were conducted in the NPT ensemble using the Nóse-Hoover thermostat [48, 49] with $\tau_T = 1$ ps and the semi-isotropic Parrinello–Rahman [97] barostat with $\tau_P = 5$ ps. The cutoff for van der Waals interactions was set to be 1.2 nm. Electrostatic interactions were treated using the Smooth Particle Mesh Ewald

scheme with a grid spacing of 0.12 nm and a 1.2 nm real-space cutoff [98]. As shown in Table 5.1, some of the simulations were executed on the Anton 2 supercomputer [175].

Analysis. The secondary structure of peptides is determined using the STRIDE algorithm within VMD [176]. In the different trajectories, peptides are found either in a disordered state (most residues are in the coil state) or as a β-strand when interacting with other peptides. Fibrils emerge when non-polar residues of two neighboring β-sheets pack against each other minimizing their exposure to the solvent–see Figure 5.10. Oligomers are loosely defined in this chapter as the structures emerging when three β-sheets in solution pack against each other. Non-polar residues are still largely exposed to the solvent in the latter—see Figure 5.8.

To estimate the pore diameter, we calculated the average number of water molecules inside a 1 nm height probe inside the pore. Then, assuming the probe to be a cylinder, its diameter was calculated using a radius of 0.14 nm for water molecules. Angles Θ and χ were computed using in-house Python codes using MDTraj package. The deuterium order parameters were computed using the GROMACS suite.

5.2 Results and Discussion

5.2.1 Pore-like membrane damage

Peptides deposited on both membrane leaflets. Three 5 μs-simulations were performed with eighteen (18) peptides randomly deposited on both leaflets of a 7:3 POPC:POPG bilayer made with 128 lipids. A temperature of 350 K was used to accelerate diffusion enabling the formation of small size β-sheets within a time-frame of $\sim$3 μs. In two of the three simulations performed here, β-sheets interacted with each other leading to the formation of a pore in the lipid membrane. This phenomena is characterized in Figure 5.1 for one of the simulations. In this figure, panel a shows the number N_w of water molecules in the space between the two leaflets. This quantity is mostly zero in the beginning of the simulation and it increases abruptly close to 3.4 μs

when poration takes place. The inset of this panel shows water molecules permeating the membrane at the end of the simulation. Panel b quantifies peptide aggregation by showing the number of backbone hydrogen bonds as a function of time. This quantity increases as peptides encounter each other on the membrane surface forming small size β-sheets [127, 177, 178]. Panels e-g illustrate this aggregation process through snapshots of peptides on upper (top panels) and lower (bottom panels) leaflets at different instances of time. Panel e depicts isolated peptides and dimers at the beginning of the simulation. At 1.7 μs (panel f), aggregation leads to the formation of trimers and tetramers on both membrane leaflets. At $\sim$ 2.9 μs, the number of hydrogen bonds saturates (see panel b) and the larger aggregates that have formed are hexamer and tetramer on one leaflet, and tetramer and dimer on the other–see panel g. The formation of tetramers or larger β-sheets preceded poration in all simulations where this phenomena took place.

Panel c shows the position of the center-of-mass (COM) of the different β-sheets along the direction normal to the membrane surface, i.e., z-axis. In this panel, the position of maximum density of POPC phosphate atoms is also shown as a reference. Peptides remain on the surface of the bilayer until very close to poration when hexamer (in orange) and tetramer (in blue) on bottom and top leaflets, respectively, penetrate the membrane. Penetration takes places within the short time-window (i.e., $\sim$ 0.2 μs) highlighted by the shaded area in Figure 5.1. subsequently, tetramer (in red) and monomers (in green) penetrate the bilayer from bottom and upper leaflets, respectively. Poration starts when some of the atoms of β-sheets that are on opposite leaflets (i.e., hexamer and tetramer) hover on top of each other–see panel h. These atoms are the first to penetrate the membrane causing β-sheets to twist–see panel h-i. This enables peptides on opposite leaflets to interact with each other half way along the bilayer cross-section to create a long transmembrane β-sheet made of ten peptides–see panel j. The latter accounts for half of the surface of a cylindrical pore

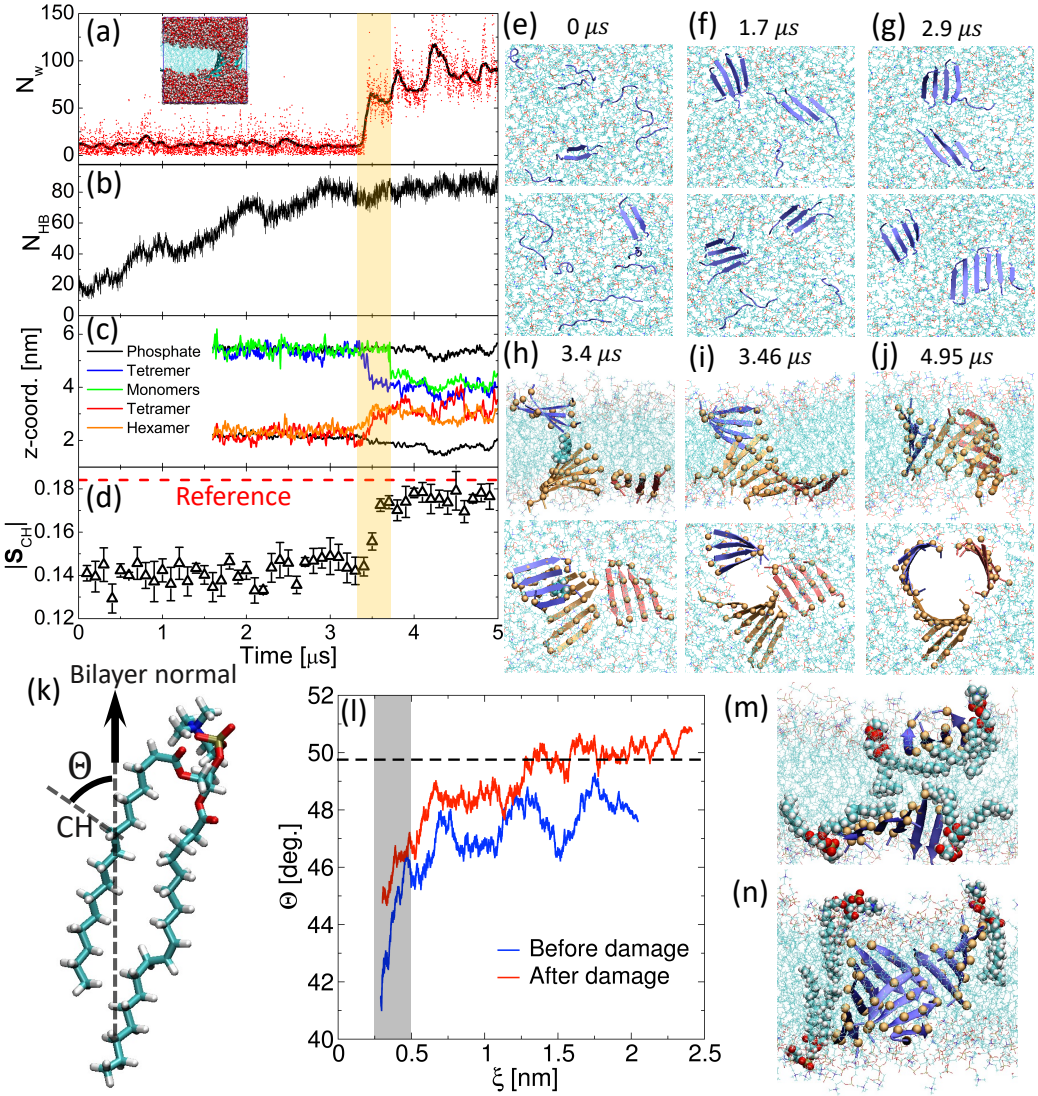

Figure 5.1 Spontaneous formation of pores starting with peptides on both membrane leaflets. (a) Number N_w of water molecules in the dry core of the bilayer (red dots) and its 100 point moving average (black line). The inset highlights water permeation at 3.78 μs. (b) Number N_{HB} of inter-backbone hydrogen bonds.(c) z-position of the COM of the different β-sheets and POPC phosphate atoms. (d) Order parameter $|\mathbf{S}_{CH}|$ computed for the methylene group of the sixth carbon atoms of POPC/POPG acyl chains. The red dashed line corresponds to the reference $|\mathbf{S}_{CH}|$ computed for a bilayer simulated without peptides. (e-j) Visual representation of peptides (in blue) on the bilayer at different time. For panels e-g, upper and lower snapshots correspond to views of top and bottom leaflets of the bilayer. For panels h-j, upper and lower snapshots correspond to views of the cross-section and top leaflet of the bilayer. For the latter panels, α-carbon atoms of phenylalanine residues are represented by orange beads. (k) Definition of the angle Θ used to define $|\mathbf{S}_{CH}|$. (l) Dependence of Θ on the minimal distance ξ of lipids to peptides. Visual representations of lipid when β-sheets are (m) deposited on the membrane and (n) forming pores.

inside the membrane. The other half of the cylindrical pore is formed by the tetramer from the bottom leaflet. Peptides forming the cylinder have non-polar and charged side chains facing its exterior and interior, respectively [141]. Moreover, the diameter of the cross-section of the pore that is available to the solvent is approximately 1.77 nm.

Notice that the spontaneous formation of a stable pore implies that the assembly of β-sheets in a cylindrical structure inside the bilayer is more favorable energetically than having individual β-sheets dispersed on the membrane surface. We hypothesize that a reduction in the distortions of acyl tail of lipids contribute to favor these pore-like assemblies of β-sheets. This is investigated in panel d where the magnitude of the deuterium order parameter is shown as a function of time. This quantity is defined as $|\mathbf{S}_{CH}| = \langle|\frac{3\cos^2\Theta-1}{2}|\rangle$, where Θ is the angle between carbon–hydrogen bonds of methylene groups and the bilayer normal [179, 180]–see panel k. For clarity, panel *d* shows $|\mathbf{S}_{CH}|$ computed for the methylene group of the sixth POPC carbon atom averaged over all lipids in the simulation box and all conformations within a

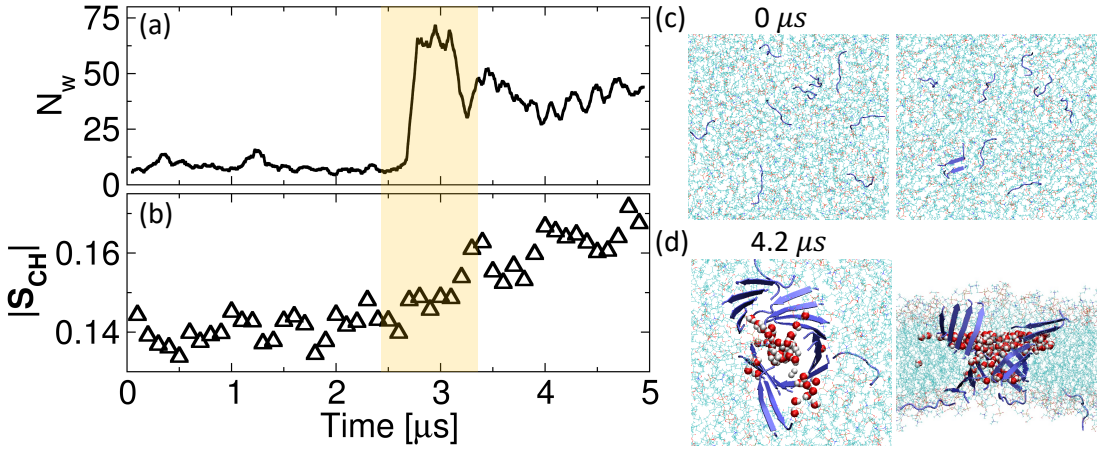

Figure 5.2 Results of the simulation No.3. (a) Number of water molecules (100 point moving average) penetrating the dry core of the bilayer. (b) Deuterium order parameter $|\mathbf{S}_{CH}|$ of the sixth acyl carbon atom. The yellow rectangle highlights the timeframe during which peptides penetrate the bilayer to form pores. Visual representation of β-sheets (in blue) on the bilayer at (c) 0 μs and (d) 4.2 μs. Top and bottom views of the bilayer are shown in left and right panels, respectively.

time-frame of 0.1 μs. Errors were estimated using block average, wherein the 0.1 μs trajectory were divided into blocks spanning 0.02 μs in time. As reference, $|\mathbf{S}_{CH}|$ computed for a 7:3 POPC:POPG bilayer simulated without peptides is shown as a red dotted line in panel *d*. Before pore formation, $|\mathbf{S}_{CH}|$ deviates significantly from the reference bilayer suggesting strong distortions in lipid tails. The formation of a pore leads to a reduction in these distortions as $|\mathbf{S}_{CH}|$ approaches the reference value. Order parameters for other methylene groups of POPC (not shown here) exhibit a similar abrupt change in $|\mathbf{S}_{CH}|$ when a pore is formed.

Panel *l* provides insights into lipid tail conformations by depicting the average angle Θ of lipids as a function of their minimal distance ξ from peptides. This distance is computed between phosphate atoms of lipid head groups and C_α atoms of peptides. Red and blue lines correspond to Θ computed just before (2.9–3.0 μs) and just after (3.1–3.2 μs) pore formation, respectively. This panel shows that close to peptides (highlighted by the gray area in the figure) lipid tails are more parallel to the membrane surface (i.e., Θ is smaller) before compared to after poration. This can be explained by favorable interactions between atoms of lipid tails and non-polar side chains. These interactions, which hold peptides anchored on the membrane surface [114, 181], also induce distortions in the lipid tail as depicted in panel m. The latter panel highlights selected lipids that are close to β-sheets before poration. Notice that acyl tails of those lipids are almost parallel to the membrane surface filling the void in the bilayer beneath β-sheets [182] and maximizing their interactions with phenylalanine side chains. Panel n highlights lipids that are close to the cylindrical pore. Hydrophobic tails of those lipids are oriented perpendicularly to the membrane surface maximizing their interactions with phenylalanine side chains of pore structures.

In addition to Figure 5.1, results from an independent 5 μs simulation performed at 350 K and starting with 18 peptides deposited on both membrane leaflets of a 7:3

POPC:POPG bilayer are shown in Figure 5.2. Also, in an attempt to study poration at a lower temperature, we reduced the temperature of the trajectory shown in Figure 5.1 to 320 K when it reached 2.5 μs, i.e., $\sim$1 μs before poration. At this instant, monomers had already aggregated into small β-sheets without penetrating into the bilayer. This system was simulated for 4 μs as shown in Figure 5.3. Both of these additional simulations are characterized by large distortions in the orientation of lipid tails due to the presence of β-sheets on the membrane surface. These distortions are significantly reduced during pore formation. Moreover, in these simulations, poration started with peptides on opposite leaflets penetrating the bilayer to interact with each other, which is consistent with results from Figure 5.1. Notice that there is increasing evidence that the Aβ peptide related to Alzheimer's disease can be found both in the intra-cellular as well as in the extra-cellular space [183–185]. This may give rise to a scenario where poration emerges from the interaction of peptides on opposite leaflets of the bilayer as shown in Figure 5.1. However, *in vitro* studies have also reported pore formation from peptides on just one leaflet of the bilayer. This situation is studied below.

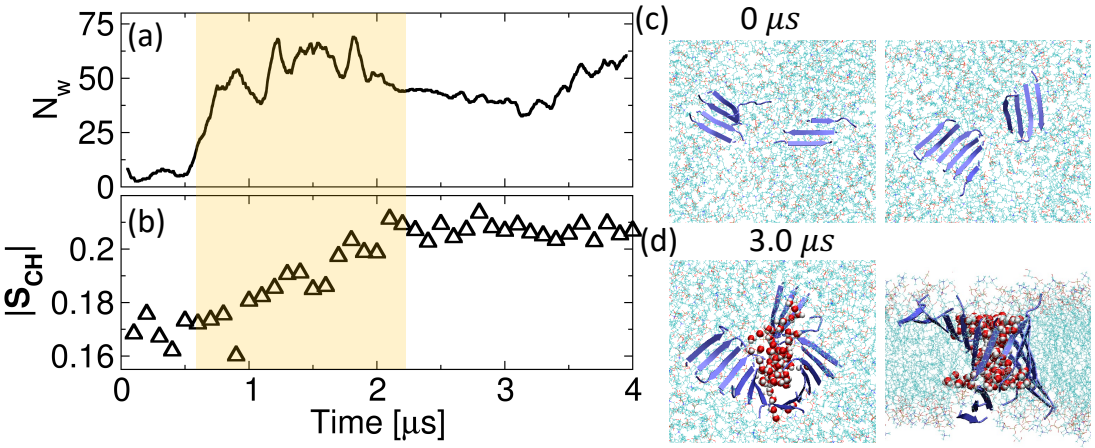

Figure 5.3 Pore formation at 320 K. (a) Number of water molecules (100 point moving average) penetrating the dry core of the bilayer. (b) Order parameter of the sixth acyl carbon atom. The yellow rectangle highlights the timeframe during which peptides penetrate the bilayer to form pores. Visual representation of β-sheets (in blue) on the bilayer at (c) 0 μs and (d) 3.0 μs. Left and right panels correspond to top and bottom views of the bilayer, respectively.

β-sheets deposited on just one membrane leaflet. Poration was observed in a simulation where two trimers and one tetramer were deposited on the same leaflet of a 7:3 DPPC:DPPG bilayer at 350 K. In this simulation, the tetramer and one of the trimers interacted to form a heptamer at 1 μs. This was followed by poration at 4.2 μs when interactions between heptamer and the remaining trimer on the membrane led to the formation of a cylinder inside the bilayer. These events are characterized in Figure 5.4 where panel a shows the z-coordinate of the COM of the different β-sheets, and panels b-d depicts the angle χ formed between the surface of β-sheets and the membrane surface–see schematic representation in Figure 5.4f. In panels b-d, the angle Θ characterizing the orientation of lipid tails (see definition in Figure 5.1k) in the vicinity of these sheets is also shown. We considered a lipid to be in the vicinity of a β-sheet if the minimum atomic distance of their tails to phenylalanine residues is smaller than 0.5 nm.

Heptamer formation and poration account for large changes in χ, Θ, and the z-coordinate of the β-sheets involved in these phenomena as highlighted by green and orange areas in Figure 5.4a-d, respectively. Heptamer formation starts with the interaction between phenylalanine side chains at the edges of the tetramer and one of the trimers as depicted in panel g. These β-sheets partially emerge out of the membrane surface enabling their non-polar faces to pack against each other to maximize favorable interactions between phenylalanine residues–see panel g. Accordingly, the z-coordinate of the COM of these β-sheets within the highlighted green area in panel a emerges out of the bilayer boundary given by phosphate atoms. This is characterized by an increase in χ in panels c,d. These β-sheet conformations remain stable for more than 0.5 μs (see green area) after which trimer and tetramer approach each other in an orientation that allows their backbone atoms to hydrogen bond–see panel h. This accounts for the formation of a stable β-sheet made from seven peptides in panel i. Until poration takes place, this larger β-sheet remains

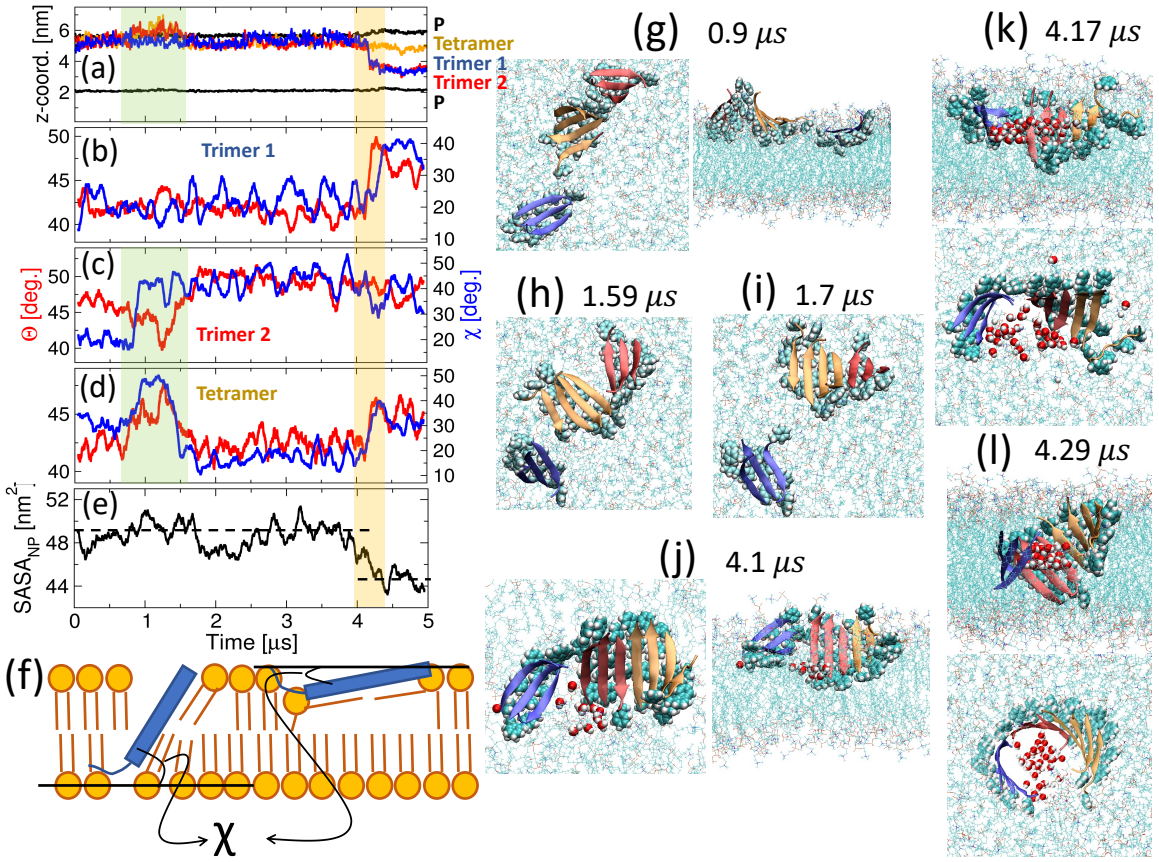

Figure 5.4 Pore formation by β-sheets deposited on one of the membrane leaflets. (a) z-coordinate of the COM of the different β-sheets and DPPC phosphate atoms (in black). Time dependence of Θ (in red) and χ (in blue) computed for (b) trimer 1, (c) trimer 2, and (d) tetramer. (e) Solvent accessible surface area of non-polar moieties (i.e., $SASA_{NP}$) of both peptides and lipids. Average values of $SASA_{NP}$ computed before and after poration are shown using black dashed lines. (f) Schematic representation of the angle χ for two β-sheets represented in blue. (g-l) Visual representations of β-sheets on the membrane surface at times. A view from the top of the membrane is provided for all time-frames. A cross-section view of the membrane is also shown in panels g and j-l. β-sheets are represented using the same color code as in panel a. Atoms of phenylalanine side chains are represented using a van der Waals representation. Only water molecules that penetrate deeply within the bilayer are shown in panels j-l.

twisted with one of its extremities being mostly parallel to the membrane surface (i.e., $\chi \sim 15^{o}$ in panel d) and the other extremity being tilted (i.e., $\chi \sim 40^{o}$ in panel c). This correlates with the orientation of lipid tails which are more parallel to the membrane surface (i.e., $\Theta \sim 40^{o}$ in panel d) around the former β-sheet extremity

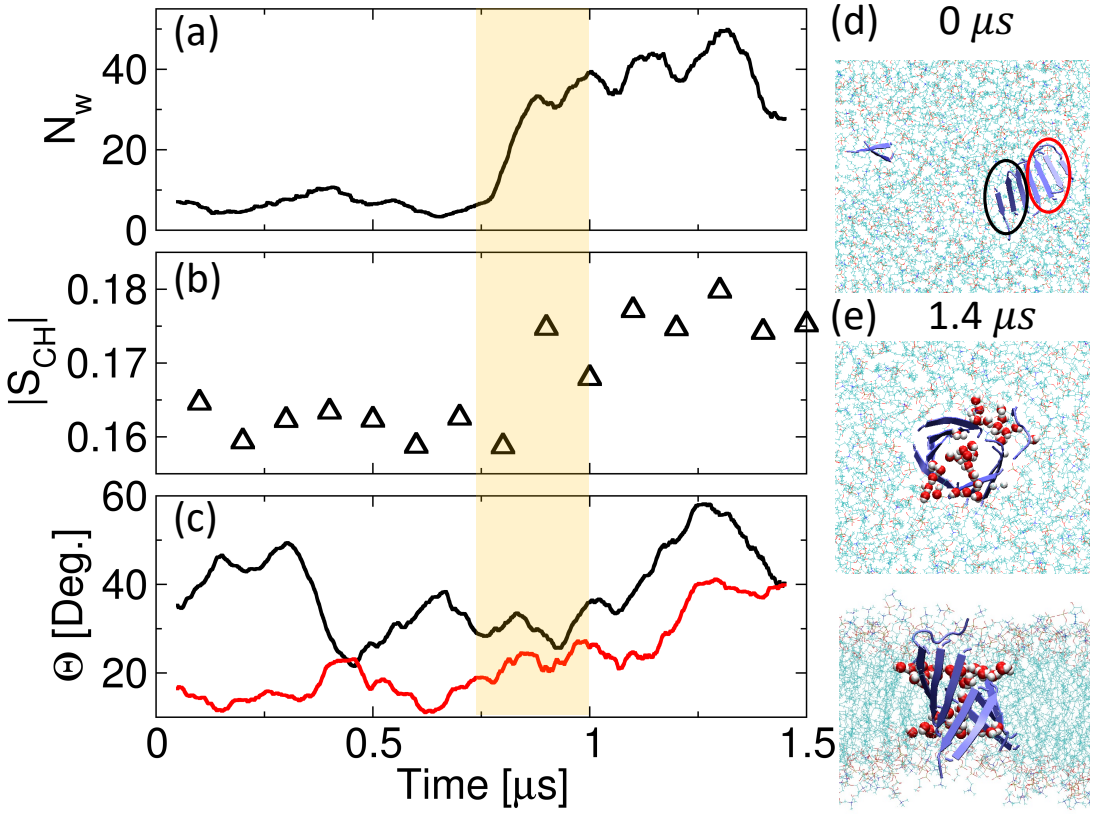

Figure 5.5 Results of simulation 7 in Table 5.1. (a) Number of water molecules (100 point moving average) penetrating the dry core of the bilayer. (b) Order parameter of the sixth acyl carbon atom. (c) Angle Θ computed for the two parts of the heptamer. The yellow rectangle highlights the time frame during which peptides penetrate the bilayer to form pores. Visual representation of β-sheets (in blue) on the bilayer at (d) 0 μs and (e) 1.4 μs. Upper and lower panels corresponds to the top and cross-section views of the bilayer.

than around the latter extremity (i.e., $\Theta \sim 50^{o}$ in panel c). As in Figure 5.1, this correlation can be related to interactions between non-polar side chains and lipid tails.

Poration is preceded by the partial penetration of water molecules, which are attracted to the charged face of β-sheets, inside the membrane. As illustrated in panel j, this penetration is pronounced around the twisted extremity of the heptamer (i.e., red β-sheet) when it interacts with the remaining trimer (blue β-sheet) on the membrane. This causes polar faces of β-sheets to wrap themselves around these water molecules to reduce the accessibility of non-polar groups of the bilayer to the solvent as shown in panels k,l. Accordingly, the solvent accessible surface area ($SASA_{NP}$)

of non-polar groups decreases during poration as shown in panel e. This minimizes unfavorable interactions of water with non-polar lipid tails inside the membrane and it contributes to stabilize the cylindrical pore structure.

In summary, small size oligomers on the membrane surface can interact with each other via the formation of contacts between non-polar side chains. This can trigger β-sheets to bury their non-polar side chains against each leading them to partially emerge from the membrane surface–see panel g. Alternatively, backbone atoms of β-sheets that are brought close to each other may form hydrogen bonds accounting for a longer β-sheet–see panel h-i. The latter becomes twisted on the membrane wherein one of its extremities remains parallel to the surface and the other penetrates the membrane–see panel j. Together with the latter extremity, water molecules, which are attracted to polar faces of β-sheets, partially penetrate inside the membrane surface–see panel j. This unfavorable presence of water inside the bilayer is minimized by tilting the polar face of β-sheets towards the axis where solvent molecules are located–panel k. This, combined with a reduction in lipid tail distortions accounts for the formation and stabilization of pore-like structures enabling water molecules to permeate membranes. The diameter of the cross-section of the cylindrical pore available to the solvent in panel l is approximately 1.24 nm.

In addition to Figure 5.4, poration from just one membrane leaflet was also simulated using a 7:3 DMPC:DMPG bilayer at 350 K and 320 K–see Figs. 5.5 and 5.6. This phenomena required only 3 μs to take place in this thinner bilayer compared to the DPPC:DPPG membrane shown in Figure 5.4. In both of these simulations, poration accounted for a significant reduction in lipid tail distortions, and, before poration, β-sheets were twisted. This is consistent with results from Figure 5.4. Simulations starting with β-sheets on just one membrane leaflet were also performed using a 7:3 POPC:POPG bilayer at 350 K. This simulation did, however, not form a pore even after 9 μs and it is discussed in the next section.

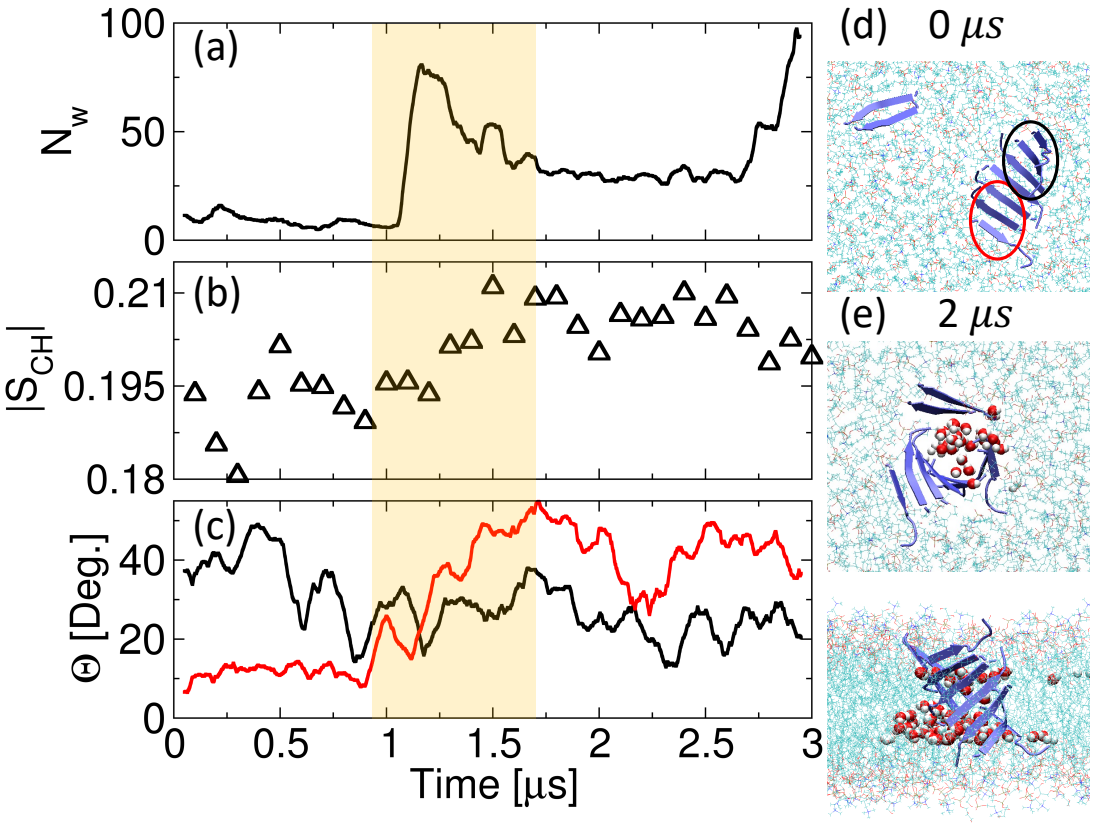

Figure 5.6 Results of simulation 8 in Table 5.1. (a) Number of water molecules (100 point moving average) penetrating the dry core of the bilayer. (b) Order parameter of the sixth acyl carbon atom. (c) Angle Θ computed for the two parts of the heptamer. The yellow rectangle highlights the timeframe during which peptides penetrate the bilayer to form pores. Visual representation of β-sheets (in blue) on the bilayer at (d) 0 μs and (e) 2 μs. Upper and lower corresponds to the top and cross-section views of the bilayer.

5.2.2 Detergent-like damage

Figure 5.7 characterizes the trajectory of a 9 μs simulation wherein hexamer and pentamer β-sheets are deposited on one leaflet of a 7:3 POPC:POPG bilayer at 350 K. In this simulation, hexamer and pentamer do not penetrate the bilayer nor do they hydrogen bond with each other to form a larger β-sheet. Instead, these oligomers partially emerge out of the lipid bilayer at three occasions similarly to the events preceding heptamer formation in Figure 5.4. These attempts to leave the membrane are highlighted by green shaded areas in Figure 5.7a where z-coordinates of the COM of hexamer and pentamer are found outside the region delimited by phosphate

atoms on both leaflets. Panel b depicts the minimum distance between hexamer and pentamer. It shows that attempts of β-sheets to emerge out of the bilayer only take place when they are interacting with each other, i.e., their distance is minimal. As in the case of heptamer formation in Figure 5.4, the force driving these events is the packing of phenylalanine side chains of different β-sheets against each other. These interactions are maximized when non-polar faces of hexamer and pentamer are buried against each other instead of facing the dry core of the bilayer. Packing of phenylalanine side chains is quantified in panel c where the solvent accessible surface area of phenylalanine side chains ($SASA_F$) is computed assuming that there is no lipids in the solutions. As hexamer and pentamer emerge out of the lipid

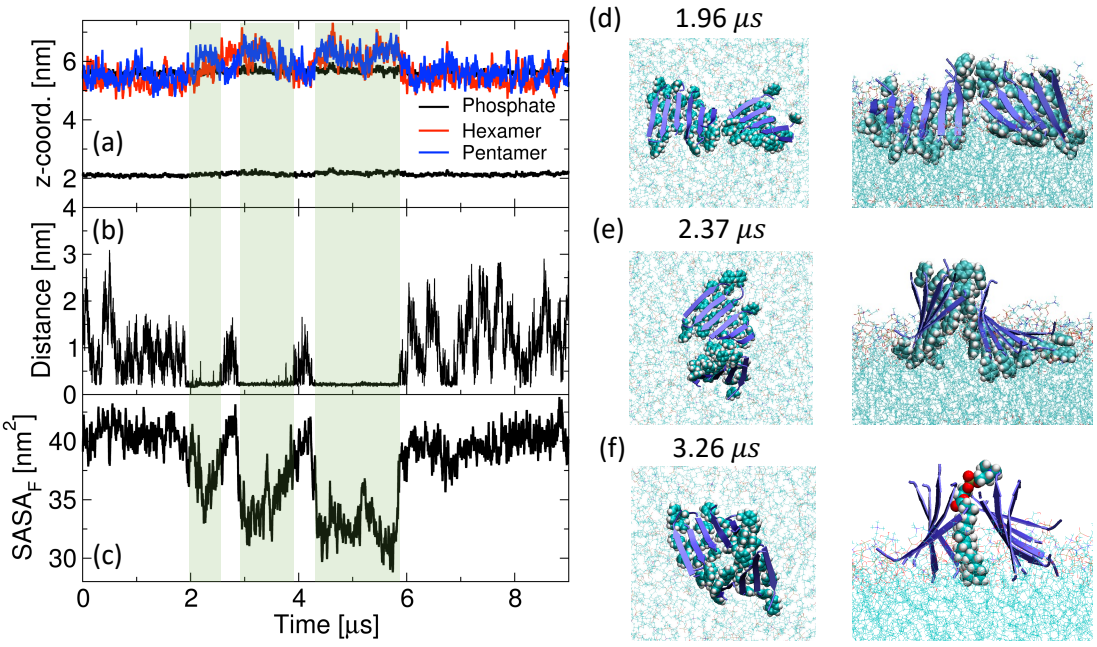

Figure 5.7 Detergent-like damage starting with β-sheets deposited on the membrane surface. (a) z-coordinate of the COM of β-sheets and POPC phosphate atoms. (b) Minimal distance between the hexamer and pentamer. The three shaded areas in panels a-c highlight regions in which β-sheets emerge out of the membrane surface. (c) Solvent accessible surface area ($SASA_F$) of phenylalanine side chains assuming that there is no lipids in the solutions. (d-f) Visual representation of β-sheets (in blue) on the bilayer at (d) 1.96 μs, (e) 2.37 μs and (f) 3.26 μs. Atoms of phenylalanine side chains are highlighted using a van der Waals representation. Left and right panels correspond to top and cross-section views of the bilayer. A selected lipid emerging out of the membrane is highlighted in panel f.

membrane, phenylalanine side chains become buried against each other and $SASA_F$ decreases. Conversely, $SASA_F$ is maximum when these β-sheets are deposited flat on the membrane.

Selected conformations of β-sheets as they emerge out the membrane are shown in panels d-f. These events take place when phenylalanine side chains at the edge of hexamer and pentamer interact with each other. During the first attempt to emerge out of the membrane, only a few side chains are interacting with each other–see panel d. During the second attempt, edges of hexamer and pentamer are better aligned enabling more phenylalanine side chains to interact–see panel e. These interactions are optimized in the third attempt to emerge out of the membrane–see panel f. Accordingly, the magnitude of $SASA_F$ in panel c drops to its lowest value in third, followed by second, and first attempts to leave the membrane. This accounts for the greater stability of the third event that survives for almost 2 μs whereas second and first events last for slightly more and less than 1 μs, respectively. In the third attempt to emerge out of the membrane, a lipid trapped in between hexamer and pentamer emerges out of the membrane–see panel f. In this configuration, lipid head and tails are exposed to the solvent and buried in between non-polar faces of β-sheets, respectively. This illustrates how the amphipathic nature of β-sheets can behave as a "detergent" removing lipids from the core of the bilayer.

The removal of lipids from the bilayer can also take place starting with β-sheets in the solution. This is illustrated in Figure 5.8 for a simulation performed with three tetramers initially located randomly in the solution–see panel d. Hydrophobic interactions between phenylalanine side chains drive tetramers towards each other enabling the formation of the *trilobal* structure in panel e. This is followed closely by the interaction of this aggregate with the 7:3 POPC:POPG membrane depicted in panel f. Favorable interactions between lipid tails and phenylalanine side chains

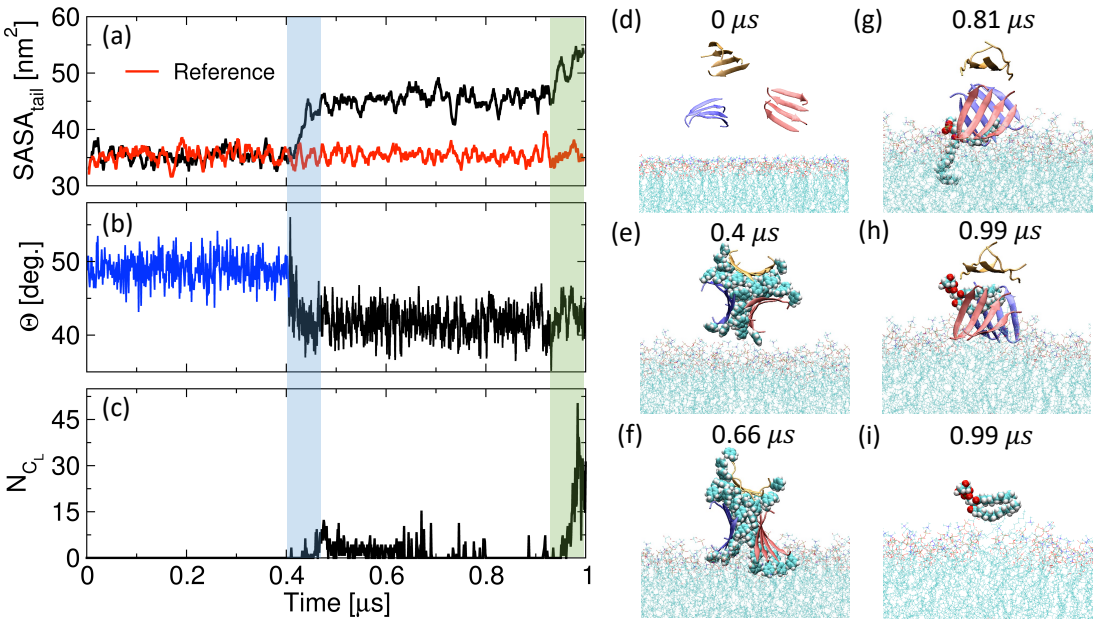

Figure 5.8 (a) Solvent accessible surface area of lipid tail atoms, i.e., $SASA_{tail}$, assuming peptides are not in the simulation box. (b) Angle Θ computed for lipids that are in the vicinity of β-sheets. (c) Number of lipid tail carbon atoms with z-coordinate outside the boundary given by the average position of nitrogen atoms of lipid head groups of upper and lower leaflets. (d-h) Visual representations of β-sheets on the lipid bilayer at different time intervals. A lipid emerging out of the bilayer is highlighted in panels g-h. Panel i highlights this lipid by hiding the trilobal structure.

stabilize the trilobal structure onto the surface of the bilayer wherein lipid tail atoms are attracted to the dry core of the trilobal structure.

To provide insights into the integrity of the membrane, Figure 5.8a shows contributions of lipid tail atoms to the solvent accessible surface area ($SASA_{tail}$) of the bilayer in the absence of peptides. This quantity is a minimum when the bilayer is unperturbed with all lipid tails packed in the dry membrane core, and it increases when lipid tails become exposed at the bilayer surface. As a reference, we show results for a simulation performed without tetramers (see red line) wherein $SASA_{tail}$ fluctuates around 35 nm^2 during the whole simulation. Before binding of the trilobal structure to the membrane surface, $SASA_{tail}$ also fluctuates around 35 nm^2. However, this quantity increases abruptly at $\sim$ 0.4 μs when the trilobal structure anchors onto the membrane causing lipid tails to become exposed at the

membrane-protein interface. This exposure can be quantified by computing the angle Θ (defined in Figure 5.1k), which characterizes the orientation of lipid tails that are in the vicinity of the trilobal structure. As in Figure 5.4b-d, we consider a lipid to be in the vicinity of a β-sheet if the minimum atomic distance of their lipid tails to phenylalanine residues is smaller than the cut-off distance of 0.5 nm–see black line in panel b. Since there are no lipids in the vicinity of β-sheets in the beginning of the simulation (i.e., $<$0.4 μs), Θ was estimated using the larger cut-off distance of 3.0 nm–see blue line in panel b. Using the latter definition, Θ fluctuates around 50^{o}, which is consistent with the orientation of lipid tails away from pore structures in Figure 5.1j, where damage is minimal. As soon as the trilobal structure binds to the membrane (see blue shaded area in Figure 5.4a-c), the value of Θ drops abruptly to approximately 40^{o}. This highlights the tendency of lipid tails to become more parallel to the membrane surface close to the trilobal structure as illustrated in panel g.

Close to the end of the simulation (shaded green area in Figure 5.8a-c), some lipids are almost completely removed from the membrane surface wherein their interactions with phenylalanine side chains are maximized–see panels h-i. As in Figure 5.7f, this highlights the potential of amphipathic β-sheets to dismantle the membrane via a detergent-like mechanisms where lipids are dragged out of the bilayer. This is quantified in Figure 5.8c by computing the number of lipid tails carbon atoms N_{C_L} with z-coordinate outside the boundary given by nitrogen atoms of lipid head groups of upper and lower leaflets. Panel c shows that a small number of lipid tail atoms emerge out of the membrane soon after the trilobal structure starts interacting with the bilayer. This number increases abruptly close to the end of the simulations characterizing the removal of lipids as depicted in panels h-i.

Note that a trilobal structure was formed in the four trajectories we generated with three tetramers in the solution. In all of these trajectories, the interactions of the trilobal structure with the membrane accounted for lipid removal. This is illustrated

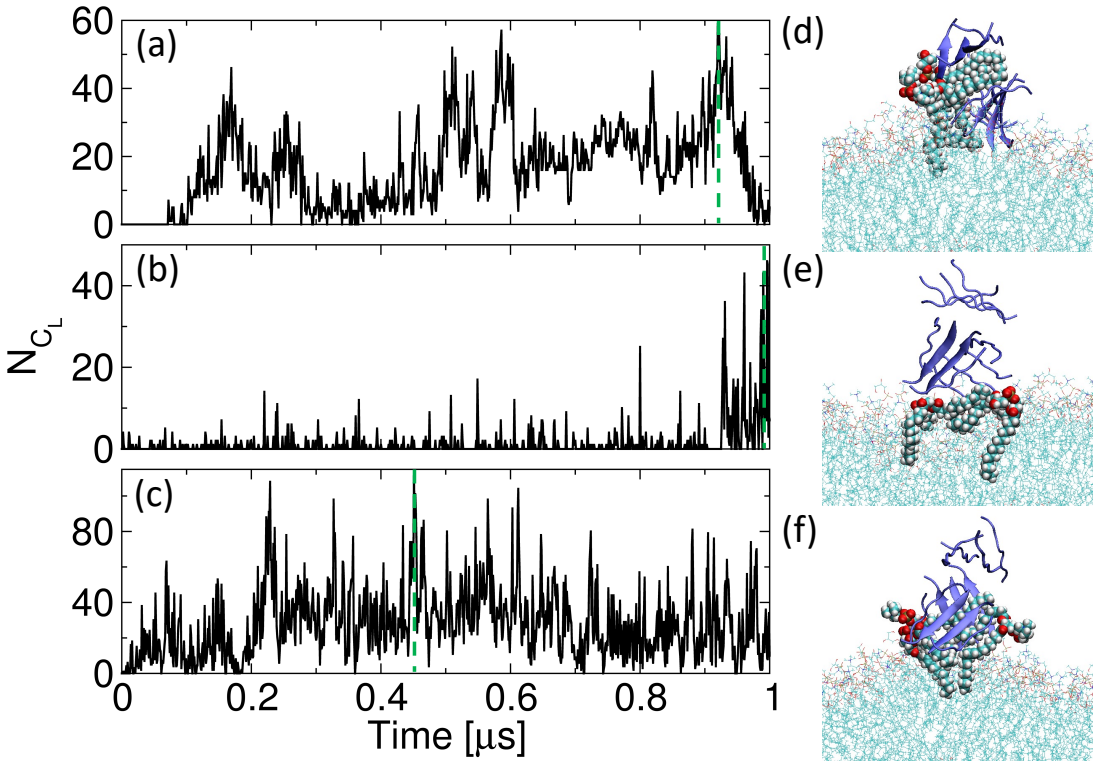

Figure 5.9 The number of carbon atoms in lipid tails that are removed from the bilayer interior computed for simulations (a) 9, (b) 10, and (c) 11 in Table 5.1. Visual presentations of β-sheets (in blue) on the bilayer with removed lipids highlighted by a van der Waals representation at times(d) 0.93 μs, (e) 0.99 μs, and (f) 0.45 μs. The corresponding times of the visual presentations are marked by green vertical dashed lines in panels a-c.

for another trajectory in Figure 5.9. It highlights the robustness of the detergent-like mechanism of membrane damage by amyloid-like peptides, which has been reported experimentally for different amyloid proteins. [17, 61, 132]

5.2.3 Fibrils are less toxic

Figure 5.10 characterizes the interaction of a small fibril with a 7:3 POPC:POPG bilayer at 350 K. The fibril is assembled by packing non-polar faces of two anti-parallel β-sheets made from five Ac–$(FKFE)_2$–NH_2 peptides each. Panel a shows the time evolution of the minimum distance between fibril and bilayer. The fibril undergoes several binding-unbinding events during the first 0.4 μs after which it remains bound to the bilayer surface until very close to the end of the simulation when it becomes

detached. Panel b shows contributions of lipid tails to the solvent accessible surface area of the bilayer in the absence of the fibril, i.e., $SASA_{tail}$. As a comparison, $SASA_{tail}$ is also shown for both a bilayer unperturbed by peptides (in red) and the bilayer interacting with the *trilobal* structure in Figure 5.8 (in blue). This figure shows that interactions of the fibril with the bilayer increases the exposure of lipid tails when compared to simulations performed without peptides. This exposure is, however, significantly lower than the one caused by the trilobal structure. Panel c depicts the average angle Θ of lipids tail in the vicinity of the fibril (in black) and the *trilobal* structure (in blue). As in Figure 5.8, a lipid is considered to be in the vicinity of fibril if the minimum atomic distance of its acyl tails to phenylalanine residues is

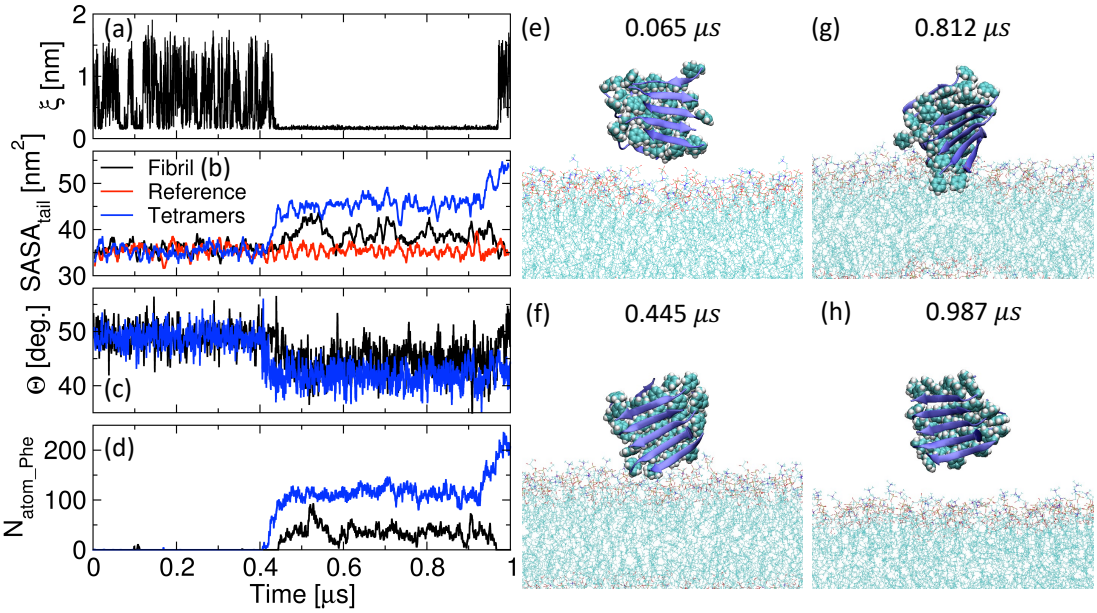

Figure 5.10 (a) Minimal distance ξ between atoms of the fibril and the bilayer. (b) Contribution of lipid tail atoms to the solvent accessible surface area of the bilayer (i.e., $SASA_{tail}$) assuming that peptides are not in the simulation box. Black, blue, and red lines are for simulations performed with a fibril in the solution, the trilobal structure of Figure 5.8, and no peptides. (c) Average angle Θ of lipids that are in the vicinity of a fibril (in black) or of the trilobal structure of Figure 5.8 (in blue). (d) The number of phenylalanine side chain atoms that are at a distance smaller than 0.5 nm from lipid tails. Black and blue lines are for simulations performed with a fibril and trilobal structure, respectively. (e-h) Visual representations of fibril and bilayer at different instants of time. A van der Waals representation is used for phenylalanine side chain.

smaller than the cut-off distance of 0.5 nm. A larger cut-off distance of 3.0 nm is used in the beginning of the simulation when the fibril is not in contact with the bilayer. This panel shows that interactions of the fibril or the *trilobal* structure with the bilayer account for a reduction in Θ as the acyl tail of lipids become more distorted. The latter distortions are, however, less pronounced around the fibril than around the *trilobal* structure. These differences can be related to less pronounced interactions between phenyalanine side chains and the lipid bilayer. Accordingly, panel g and Figure 5.8f depict two and at least four phenylalanine side chains deeply buried inside the bilayer for fibril and *trilobal* structure, respectively. This is quantified in panel d where the number of phenylalanine side chain atoms that are at a distance smaller than 0.5 nm from any lipid tail is shown. These numbers are higher for the *trilobal* structure than for the fibril. Thus, although our simulations cannot assert that fibrils are non-toxic due to the limited simulation time, it disrupts the membrane less significantly than oligomers/trilobal structures. At the end of the simulation (i.e., panel h) the fibril detaches itself from the membrane.

5.3 Conclusion

The atomic details of how amyloids and β-hairpin peptides interact with lipid membranes causing damage remains unclear. This knowledge is critical to develop new treatments for amyloid diseases as well as to rationally design antimicrobial peptides. Here, we performed one of the first all-atom simulations in which membrane-bound peptides self-assemble into β-sheets that subsequently either form pores on the membrane surface or drag lipids out of the bilayer core. An analysis of these simulations shows that these mechanisms of membrane damage are strongly affected by interactions between non-polar side chains and the acyl tail of lipids, which hold peptides anchored onto the membrane surface [114]. These strong interactions enable lipids to be dragged out of the bilayer by oligomeric structures in

a detergent-like manner. They also account for distortions in the orientation of lipid tails that are minimized when pores are formed.

In our simulations, membrane damage took place as a result of the interaction between two β-sheets. In detergent-like damages, two β-sheets emerge out of the membrane to bury their non-polar residues against each other. In this process, lipid tails that are strongly bound to non-polar residues are also dragged out of the membrane. In pore-like damages, two β-sheets penetrate the membrane while maintaining their non-polar residues buried against the dry core of the bilayer. Each β-sheet accounts for half of the cylindrical surface of pores that have diameters ranging from 1.2 nm to 1.8 nm in our simulations. Notice that non-polar residues are buried in the dry core of fibrils and, thus, these structures did not perturb lipid membranes in a significant manner in our simulations.

In simulations, membrane-bound β-sheets become twisted with one of their extremities partially penetrating the lipid bilayer. This allows peptides on opposite leaflets to interact and form long transmembrane β-sheets that initiate poration. The twist of β-sheets also allows water molecules to partially penetrate the membrane. In simulations where peptides are deposited on a single leaflet, β-sheets penetrate the membrane by tilting their polar faces towards these partially penetrating water molecules while keeping non-polar residues buried against acyl-tails of lipids.

The mechanistic insights brought up by this study were obtained from an analysis of several simulations (a total of ~ 40 μs) performed at two temperatures (320 K or 350 K), using three anionic membranes, and different numbers of peptides on the membrane/solution. The results obtained from this study are, therefore, robust but their scope needs to be tested for other peptide sequences. We also believe that important new insights will be obtained by simulating membrane damage using different lipid compositions, which has been shown to affect the onset of amyloid diseases [9, 13, 15, 19, 60, 186].

CHAPTER 6

SUMMARY AND FUTURE WORK

6.1 Conclusion

In this dissertation, we addressed three major problems related to the amyloid-membrane interactions using molecular dynamics simulations. First, we studied binding mechanisms of amyloid-like peptides to lipid membrane and effects of lipid composition and divalent cations. Understanding the driving force of peptide-membrane attraction and the factor that affect this interaction give important insights into the pathogenesis of amyloid diseases including Alzheimer's. Second, we investigated a set of amphipathic peptides with varying net charge, amino acid order and hydrophobicity. These peptides exhibits discrepant binding affinity to lipid membrane, which is important to determine the toxic segment of amyloid protein. This study also sheds light to the design of antimicrobial peptides that enable organisms to defend themselves against biological threats. Third, we studied membrane damage induced by amyloid peptides. This knowledge is critical to understand the cell toxicity of amyloid proteins. To address these problems, we performed all atom molecular dynamics simulations with explicit water model.

In Chapter 3 of this dissertation, we studied binding mechanisms of peptides to lipid bilayers and effects of lipid composition and ions. We performed simulations using individual peptides with alternating polar and non-polar residues. We employed a water box with a large size in the z-direction allowing the peptide move freely in the solution. The simulations show that the peptide can bind to the lipid bilayer with two modes, in which it binds to the head groups of the bilayer for a short period of time, i.e., reversible binding, and anchors to the bilayer with non-polar side chains buried in the dry core of the bilayer for a long term, i.e., strong binding. The reversible

binding frames allow us to represent their binding strength quantitatively. Our results show that the presence of Ca^{2+} can significantly resist peptide from binding to the bilayer, whereas the addition of anionic lipids into the bilayer can enhance the binding strength. These results imply that the peptide binds to the bilayer through the attraction between positive side chains of peptide and negative moieties of lipid head groups for the reason that the binding of Ca^{2+} to the bilayer makes it positively charged, whereas the addition of anionic lipids derives a negative bilayer. The latter was validated by tracking the type of residues that are closest to the membrane at different distance. This study indicates the importance of positive charge in the peptide sequences regarding the peptide-membrane attraction.

In addition, we explored another important factor, i.e., amino acid sequence, that can impact the binding of peptide to lipid membrane in Chapter 4. The results of our simulations on a series of peptide sequences with varying net charge show that their affinity to the lipid bilayer exhibit significant discrepancy, wherein positive peptides are favored in contrast to negatively charged ones. This observation highlights the importance of positive charges in the binding of peptides to lipid membrane. As such, we studied a series of neutral peptides with the same number of positive, negative, and non-polar residues, in which the position of positive residues vary from the extremities to the middle of the peptide. The results show that the latter affects the extend by which positive side chains are exposed to the solvent. We find that peptides with positive residues located at their extremities are more exposed to the solvent and, thus, encounter the membrane with higher frequency. On the other hand, the adsorption of a peptide to the membrane involves burying its non-polar side chains into the dry core of the lipid bilayer. Accordingly, we find that amphipathic peptides made with non-polar residues that are less hydrophobic are adsorbed into the membrane in a smaller number of trajectories than peptides made with more hydrophobic residues. In the same vein, we observed that the position of

non-polar residues in the peptide sequence affects its tendency to be adsorbed into the membrane, i.e., sequences with phenylalanine at the extremity of the peptide sequence have the higher tendency to be adsorbed in our simulations.

In Chapter 5, we performed the first all-atom simulations in which membrane-bound peptides self-assemble into β-sheets that subsequently either form pores on the membrane surface or drag lipids out of the bilayer core. The analysis of the simulations shows that these mechanisms of membrane damage are strongly affected by interactions between non-polar side chains and the acyl tail of lipids. These strong interactions enable lipids to be dragged out of the bilayer by oligomeric structures in a detergent-like damage. They also disturb the orientation of lipid tails in the vicinity of peptides. These distortions are minimized around pore structures. We also show that membrane-bound β-sheets become twisted with one of their extremities partially penetrating the lipid bilayer. This allows peptides on opposite leaflets to interact and form a long transmembrane β-sheet, which initiates poration. In simulations where peptides are deposited on a single leaflet, the twist in β-sheet allows them to penetrate the membrane and form pores. In addition, our simulations show that fibril-like structures produce little damage to lipid membranes as non-polar side chains in these structures are unavailable to interact with the acyl tail of lipids.

6.2 Proposed Future Work

We showed the importance of positive charge in the peptide-membrane interactions, whereas the role of negative charge in peptides is worth exploring. In our simulations, negative charge exhibits strong aversion to the lipid membranes, however, the negatively charged N-terminal region of Aβ may play a critical role in the adsorption of Aβ on membrane [187]. Moreover, cation mediated binding between negative side chain and negative moiety of lipid (i.e., salt bridge) in the presence of strongly anionic membrane can make negatively charged peptides become favorable to lipid

membrane [114]. Thus, it could be interesting to perform simulations on the interaction of negatively charged peptides with anionic lipid bilayers in the presence of divalent cations, e.g., Ca^{2+}. This study can also provide insights into the design of antimicrobial peptides due the anionic property of bacterial membrane. Moreover, the outer membrane of bacteria contains lipopolysaccharide, which could play an important role in peptide-membrane binding. Thus, it is worth checking the affinity of peptides to membranes containing lipopolysaccharide.

In this dissertation, we performed the first all-atom simulations in which membrane-bound peptides self-assemble into β-sheets that subsequently either form pores on the membrane surface or drag lipids out of the bilayer core. In these simulations, pre-deposited peptides showed the potential to aggregate on membrane surface. This aggregation can also be found in the solvent [127]. However, it is obvious that the membranous environment is different from the solvent. The aggregation of different peptides in solvent-membrane interface can be a valuable direction to proceed. For example, some peptide that were found to have low tendency to aggregate in the solvent [127] might aggregate when they anchored to membrane surface. Regarding the penetrating of the β-sheets forming pores in the membrane, I anticipate that new insights will be obtained by studying either different peptide sequences or membranes with different lipid compositions.

In the simulations where we observed detergent-like damages of the membrane, lipids were dragged out of the bilayer core to occupy the dry cage formed by β-sheets. A limitations of these simulations are that the lipid-protein complex has never been observed to completely depart from the membrane and the removal of lipids from the membrane is reversible. These behaviors deviate from the proposed detergent-like effect of amyloid. We believe that alternate peptide sequences and longer time frame simulations are needed to address these discrepancies.

REFERENCES

[1] S. C. Lovell, I. W. Davis, W. B. Arendall III, P. I. W. de Bakker, J. M. Word, M. G. Prisant, J. S. Richardson, and D. C. Richardson. Structure validation by cα geometry: ϕ, ψ and cβ deviation. *Proteins: Structure, Function, and Bioinformatics*, 50(3):437–450, 2003.

[2] T. F. Cunningham, M. R. Putterman, A. Desai, W. S. Horne, and S. Saxena. The double-histidine cu^{2+}-binding motif: a highly rigid, site-specific spin probe for electron spin resonance distance measurements. *Angewandte Chemie*, 54(21):6330–6334, 2015.

[3] T. Luhrs, C. Ritter, M. Adrian, D. Riek-Loher, B. Bohrmann, H. Doeli, D. Schubert, and R. Riek. 3d structure of alzheimer's amyloid-beta (1-42) fibrils. *Proceedings of the National Academy of Sciences*, 102(48):17342–17347, 2005.

[4] R. Kayed. Common structure of soluble amyloid oligomers implies common mechanism of pathogenesis. *Science*, 300(5618):486–489, 2003.

[5] C. Haass and D. J. Selkoe. Soluble protein oligomers in neurodegeneration: lessons from the alzheimer's amyloid β-peptide. *Nature Reviews Molecular Cell Biology*, 8(2):101–112, 2007.

[6] S. Chimon, M. A. Shaibat, C. R. Jones, D. C. Calero, B. Aizezi, and Y. Ishii. Evidence of fibril-like β-sheet structures in a neurotoxic amyloid intermediate of alzheimer's β-amyloid. *Nature Structural & Molecular Biology*, 14(12):1157–1164, 2007.

[7] M. F. M. Sciacca, S. A. Kotler, J. R. Brender, J. Chen, D. K. Lee, and A. Ramamoorthy. Two-step mechanism of membrane disruption by a beta through membrane fragmentation and pore formation. *Biophysical Journal*, 103(4):702–710, 2012.

[8] M. Stefani and C. M. Dobson. Protein aggregation and aggregate toxicity: new insights into protein folding, misfolding diseases and biological evolution. *Journal of Molecular Medicine*, 81(11):678–699, 2003.

[9] M. C. Owen, D. Gnutt, M. Gao, S. K. Wärmländer, J. Jarvet, A. Gräslund, R. Winter, S. Ebbinghaus, and B. Strodel. Effects of in vivo conditions on amyloid aggregation. *Chemical Society Reviews*, 48:3946–3996, 2019.

[10] I. Bezprozvanny and M. P. Mattson. Neuronal calcium mishandling and the pathogenesis of alzheimer's disease. *Trends in Neurosciences*, 31(9):454 – 463, 2008.

[11] C. Cecchi, S. Baglioni, C. Fiorillo, A. Pensalfini, G. Liguri, D. Nosi, S. Rigacci, M. Bucciantini, and M. Stefani. Insights into the molecular basis of the differing susceptibility of varying cell types to the toxicity of amyloid aggregates. *Journal of Cell Science*, 118(15):3459–3470, 2005.

[12] J. Habchi, S. Chia, C. Galvagnion, T. C. T. Michaels, M. M. J. Bellaiche, F. S. Ruggeri, M. Sanguanini, I. Idini, J. R. Kumita, and E. Sparr. Cholesterol catalyses aβ42 aggregation through a heterogeneous nucleation pathway in the presence of lipid membranes. *Nature Chemistry*, 10(6):673–683, 2018.

[13] X. Zhang, J. R. St. Clair, E. London, and D. P. Raleigh. Islet amyloid polypeptide membrane interactions: effects of membrane composition. *Biochemistry*, 56(2):376–390, 2017.

[14] J. E. Straub and D. Thirumalai. Membrane–protein interactions are key to understanding amyloid formation. *The Journal of Physical Chemistry Letters*, 5(3):633–635, 2014.

[15] E. Drolle, A. Negoda, K. Hammond, E. Pavlov, and Z. Leonenko. Changes in lipid membranes may trigger amyloid toxicity in alzheimer's disease. *PLoS One*, 12(8):e0182194, 2017.

[16] M. Bucciantini, S. Rigacci, and M. Stefani. Amyloid aggregation: Role of biological membranes and the aggregate–membrane system. *The Journal of Physical Chemistry Letters*, 5(3):517–527, 2014.

[17] M. F. M. Sciacca, I. Monaco, C. La Rosa, and D. Milardi. The active role of ca^{2+} ions in aβ-mediated membrane damage. *Chemical Communications*, 54(29):3629–3631, 2018.

[18] Y. Liu, B. Ren, Y. Zhang, Y. Sun, Y. Chang, G. Liang, L. Xu, and J. Zheng. Molecular simulation aspects of amyloid peptides at membrane interface. *Biochimica et Biophysica Acta - Biomembranes*, 1860(9):1906 – 1916, 2018.

[19] C. L. Dias, S. Jalali, Y. Yang, and L. Cruz. Role of cholesterol on binding of amyloid fibrils to lipid bilayers. *The Journal of Physical Chemistry B*, 124(15):3036–3042, 2020.

[20] F. Hane, E. Drolle, R. Gaikwad, E. Faught, and Z. Leonenko. Amyloid-beta aggregation on model lipid membranes: an atomic force microscopy study. *Journal of Alzheimer's Disease*, 26(3):485–494, 2011.

[21] E. Drolle, R. M. Gaikwad, and Z. Leonenko. Nanoscale electrostatic domains in cholesterol-laden lipid membranes create a target for amyloid binding. *Biophysical Journal*, 103(4):L27–L29, 2012.

[22] M. Manna and C. Mukhopadhyay. Binding, conformational transition and dimerization of amyloid-beta peptide on GM1-containing ternary membrane: insights from molecular dynamics simulation. *PLoS ONE*, 8(8):e71308, 2013.

[23] N. Ntarakas, I. Ermilova, and A. P. Lyubartsev. Effect of lipid saturation on amyloid-beta peptide partitioning and aggregation in neuronal membranes: molecular dynamics simulations. *European Biophysics Journal*, 48(8):813–824, 2019.

[24] P. K. Kinnunen. Amyloid formation on lipid membrane surfaces. *The Open Biology Journal*, 2(1):163–175, 2009.

[25] K. W. Tipping, T. K. Karamanos, T. Jakhria, M. G. Iadanza, S. C. Goodchild, R. Tuma, N. A. Ranson, E. W. Hewitt, and S. E. Radford. ph-induced molecular shedding drives the formation of amyloid fibril-derived oligomers. *Proceedings of the National Academy of Sciences*, 112(18):5691–5696, 2015.

[26] G. Ramachandran, C. Ramakrishnan, and V. Sasisekharan. Stereochemistry of polypeptide chain configurations. *Journal of Molecular Biology*, 7(1):95–99, 1963.

[27] C. B. Anfinsen. Principles that govern the folding of protein chains. *Science*, 181(4096):223–230, 1973.

[28] J. Kubelka, J. Hofrichter, and W. A. Eaton. The protein folding 'speed limit'. *Current Opinion in Structural Biology*, 14(1):76–88, 2004.

[29] M. Frost, E. Karakatsani, N. von Solms, D. Richon, and G. M. Kontogeorgis. Vapor–liquid equilibrium of methane with water and methanol. measurements and modeling. *Journal of Chemical & Engineering Data*, 59(4):961–967, 2013.

[30] F. Chiti and C. M. Dobson. Protein misfolding, functional amyloid, and human disease. *Annual Review of Biochemistry*, 75(1):333–366, 2006.

[31] P. Cras, M. Kawai, D. Lowery, P. Gonzalez-DeWhitt, B. Greenberg, and G. Perry. Senile plaque neurites in alzheimer disease accumulate amyloid precursor protein. *Proceedings of the National Academy of Sciences*, 88(17):7552–7556, 1991.

[32] M. Nistor, M. Don, M. Parekh, F. Sarsoza, M. Goodus, G. Lopez, C. Kawas, J. Leverenz, E. Doran, I. Lott, M. Hill, and E. Head. Alpha- and beta-secretase activity as a function of age and beta-amyloid in down syndrome and normal brain. *Neurobiology of Aging*, 28(10):1493–1506, 2007.

[33] W. T. Astbury, S. Dickinson, and K. Bailey. The x-ray interpretation of denaturation and the structure of the seed globulins. *Biochemical Journal*, 29(10):2351–2360.1, 1935.

[34] T. J. Huang, D.-S. Yang, P. E. Fraser, and A. Chakrabartty. Alternate aggregation pathways of the alzheimer β-amyloid peptide. *Journal of Biological Chemistry*, 275(46):36436–36440, 2000.

[35] A. Lomakin, D. S. Chung, G. B. Benedek, D. A. Kirschner, and D. B. Teplow. On the nucleation and growth of amyloid beta-protein fibrils: detection of nuclei and quantitation of rate constants. *Proceedings of the National Academy of Sciences*, 93(3):1125–1129, 1996.

[36] M. Fändrich, J. Meinhardt, and N. Grigorieff. Structural polymorphism of alzheimer aβ and other amyloid fibrils. *Prion*, 3(2):89–93, 2009.

[37] C. Schmitz, B. P. Rutten, A. Pielen, S. Schäfer, O. Wirths, G. Tremp, C. Czech, V. Blanchard, G. Multhaup, P. Rezaie, H. Korr, H. W. Steinbusch, L. Pradier, and T. A. Bayer. Hippocampal neuron loss exceeds amyloid plaque load in a transgenic mouse model of alzheimer's disease. *The American Journal of Pathology*, 164(4):1495–1502, 2004.

[38] J. M. M. Donald, G. M. Savva, C. Brayne, A. T. Welzel, G. Forster, G. M. Shankar, D. J. Selkoe, P. G. Ince, and D. M. Walsh. The presence of sodium dodecyl sulphate-stable aβ dimers is strongly associated with alzheimer-type dementia. *Brain*, 133(5):1328–1341, 2010.

[39] C. A. McLean, R. A. Cherny, F. W. Fraser, S. J. Fuller, M. J. Smith, K. Vbeyreuther, A. I. Bush, and C. L. Masters. Soluble pool of aβ amyloid as a determinant of severity of neurodegeneration in alzheimer's disease. *Annals of Neurology*, 46(6):860–866, 1999.

[40] E. Oldfield and D. Chapman. Deuteron resonance: A novel approach to the study of hydrocarbon chain mobility in membrane systems. *FEBS Letters*, 16(2):102–104, 1971.

[41] L. Verlet. Computer "experiments" on classical fluids. i. thermodynamical properties of lennard-jones molecules. *Physical Review*, 159(1):98–103, 1967.

[42] R. Hockney. The potential calculation and some applications. *Methods in Computational Physics*, 9:136, 1970.

[43] W. C. Swope, H. C. Andersen, P. H. Berens, and K. R. Wilson. A computer simulation method for the calculation of equilibrium constants for the formation of physical clusters of molecules: Application to small water clusters. *The Journal of Chemical Physics*, 76(1):637–649, 1982.

[44] D. Beeman. Some multistep methods for use in molecular dynamics calculations. *Journal of Computational Physics*, 20(2):130–139, 1976.

[45] L. Woodcock. Isothermal molecular dynamics calculations for liquid salts. *Chemical Physics Letters*, 10(3):257–261, 1971.

[46] H. J. C. Berendsen, J. P. M. Postma, W. F. van Gunsteren, A. DiNola, and J. R. Haak. Molecular dynamics with coupling to an external bath. *The Journal of Chemical Physics*, 81(8):3684–3690, 1984.

[47] H. C. Andersen. Molecular dynamics simulations at constant pressure and/or temperature. *The Journal of Chemical Physics*, 72(4):2384–2393, 1980.

[48] S. Nosé. A unified formulation of the constant temperature molecular dynamics methods. *The Journal of Chemical Physics*, 81(1):511–519, 1984.

[49] W. G. Hoover. Canonical dynamics: Equilibrium phase-space distributions. *Physical Review A*, 31(3):1695–1697, 1985.

[50] P. M. Morse. Diatomic molecules according to the wave mechanics. ii. vibrational levels. *Physical Review*, 34:57–64, 1929.

[51] M. Bulacu, N. Goga, W. Zhao, G. Rossi, L. Monticelli, X. Periole, D. P. Tieleman, and S. J. Marrink. Improved angle potentials for coarse-grained molecular dynamics simulations. *Journal of Chemical Theory and Computation*, 9(8):3282–3292, 2013.

[52] W. L. Jorgensen and J. Tirado-Rives. The opls [optimized potentials for liquid simulations] potential functions for proteins, energy minimizations for crystals of cyclic peptides and crambin. *Journal of the American Chemical Society*, 110(6):1657–1666, 1988.

[53] S. J. Weiner, P. A. Kollman, D. A. Case, U. C. Singh, C. Ghio, G. Alagona, S. Profeta, and P. Weiner. A new force field for molecular mechanical simulation of nucleic acids and proteins. *Journal of the American Chemical Society*, 106(3):765–784, 1984.

[54] B. R. Brooks, R. E. Bruccoleri, B. D. Olafson, D. J. States, S. Swaminathan, and M. Karplus. Charmm: A program for macromolecular energy, minimization, and dynamics calculations. *Journal of Computational Chemistry*, 4(2):187–217, 1983.

[55] C. Oostenbrink, A. Villa, A. E. Mark, and W. F. Van Gunsteren. A biomolecular force field based on the free enthalpy of hydration and solvation: The gromos force-field parameter sets 53a5 and 53a6. *Journal of Computational Chemistry*, 25(13):1656–1676, 2004.

[56] J. Hardy and D. Allsop. Amyloid deposition as the central event in the aetiology of alzheimer's disease. *Trends in Pharmacological Sciences*, 12:383–388, 1991.

[57] E. Y. Hayden and D. B. Teplow. Amyloid β-protein oligomers and alzheimer's disease. *Alzheimer's Research & Therapy*, 5(6):60, 2013.

[58] I. Benilova, E. Karran, and B. De Strooper. The toxic a-β oligomer and alzheimer's disease: an emperor in need of clothes. *Nature Neuroscience*, 15(3):349–357, 2012.

[59] S.-Y. Ow and D. E. Dunstan. A brief overview of amyloids and alzheimer's disease. *Protein Science*, 23(10):1315–1331, 2014.

[60] M. Stefani and G. Liguri. Cholesterol in alzheimer's disease: unresolved questions. *Current Alzheimer Research*, 6(1):15–29, 2009.

[61] M. F. Sciacca, D. Milardi, G. M. Messina, G. Marletta, J. R. Brender, A. Ramamoorthy, and C. L. Rosa. Cations as switches of amyloid-mediated membrane disruption mechanisms: calcium and iapp. *Biophysical Journal*, 104(1):173 – 184, 2013.

[62] K. W. Tipping, P. van Oosten-Hawle, E. W. Hewitt, and S. E. Radford. Amyloid fibres: inert end-stage aggregates or key players in disease? *Trends in Biochemical Sciences*, 40(12):719–727, 2015.

[63] E. Hellstrand, E. Sparr, and S. Linse. Retardation of abeta fibril formation by phospholipid vesicles depends on membrane phase behavior. *Biophysical Journal*, 98(10):2206 – 2214, 2010.

[64] B. Bonev, A. Watts, M. Bokvist, and G. Gröbner. Electrostatic peptide–lipid interactions of amyloid-beta peptide and pentalysine with membrane surfaces monitored by 31p MAS NMR. *Physical Chemistry Chemical Physics*, 3(14):2904–2910, 2001.

[65] B. Moores, E. Drolle, S. J. Attwood, J. Simons, and Z. Leonenko. Effect of surfaces on amyloid fibril formation. *PLoS ONE*, 6(10):e25954, 2011.

[66] D. J. Lindberg, E. Wesén, J. Björkeroth, S. Rocha, and E. K. Esbjörner. Lipid membranes catalyse the fibril formation of the amyloid-β (1–42) peptide through lipid-fibril interactions that reinforce secondary pathways. *Biochimica et Biophysica Acta - Biomembranes*, 1859(10):1921–1929, 2017.

[67] H.-J. Lee, C. Choi, and S.-J. Lee. Membrane-bound α-synuclein has a high aggregation propensity and the ability to seed the aggregation of the cytosolic form. *Journal of Biological Chemistry*, 277(1):671–678, 2002.

[68] E. Sparr, M. F. Engel, D. V. Sakharov, M. Sprong, J. Jacobs, B. de Kruijff, J. W. Höppener, and J. Antoinette Killian. Islet amyloid polypeptide-induced membrane leakage involves uptake of lipids by forming amyloid fibers. *FEBS Letters*, 577(1-2):117–120, 2004.

[69] M. Zhu, P. O. Souillac, C. Ionescu-Zanetti, S. A. Carter, and A. L. Fink. Surface-catalyzed amyloid fibril formation. *Journal of Biological Chemistry*, 277(52):50914–50922, 2002.

[70] S.-R. Ji, Y. Wu, and S.-f. Sui. Cholesterol is an important factor affecting the membrane insertion of β-amyloid peptide (aβ1–40), which may potentially inhibit the fibril formation. *Journal of Biological Chemistry*, 277(8):6273–6279, 2001.

[71] E. Y. Chi, C. Ege, A. Winans, J. Majewski, G. Wu, K. Kjaer, and K. Y. C. Lee. Lipid membrane templates the ordering and induces the fibrillogenesis of alzheimer's disease amyloid-β peptide. *Proteins: Structure, Function, and Bioinformatics*, 72(1):1–24, 2008.

[72] A. Chauhan, I. Ray, and V. P. Chauhan. Interaction of amyloid beta-protein with anionic phospholipids: possible involvement of lys28 and c-terminus aliphatic amino acids. *Neurochemical Research*, 25(3):423–429, 2000.

[73] C. Kang and R. Sun. Molecular dynamics study of the interaction between the n-terminal of alpha-synuclein and a lipid bilayer mimicking synaptic vesicles. *The Journal of Physical Chemistry B*, 125(4):1036–1048, 2021.

[74] A. A. Meratan, A. Ghasemi, and M. Nemat-Gorgani. Membrane integrity and amyloid cytotoxicity: a model study involving mitochondria and lysozyme fibrillation products. *Journal of Molecular Biology*, 409(5):826–838, 2011.

[75] S. Ohnishi and T. Ito. Calcium-induced phase separations in phosphatidylserine-phosphatidylcholine membranes. *Biochemistry (Mosc)*, 13(5):881–887, 1974.

[76] S. Tamamizu-Kato, M. G. Kosaraju, H. Kato, V. Raussens, J.-M. Ruysschaert, and V. Narayanaswami. Calcium-triggered membrane interaction of the α-synuclein acidic tail. *Biochemistry (Mosc)*, 45(36):10947–10956, 2006.

[77] V. Gerke, C. E. Creutz, and S. E. Moss. Annexins: linking ca^{2+} signalling to membrane dynamics. *Nature Reviews Molecular Cell Biology*, 6(6):449–461, 2005.

[78] C. Lockhart and D. K. Klimov. Calcium enhances binding of aβ monomer to dmpc lipid bilayer. *Biophysical Journal*, 108(7):1807–1818, 2015.

[79] X. Yi, Y. Zhang, M. Gong, X. Yu, N. Darabedian, J. Zheng, and F. Zhou. Ca^{2+} interacts with glu-22 of aβ (1–42) and phospholipid bilayers to accelerate the aβ (1–42) aggregation below the critical micelle concentration. *Biochemistry (Mosc)*, 54(41):6323–6332, 2015.

[80] J. A. Lemkul and D. R. Bevan. Perturbation of membranes by the amyloid beta-peptide - a molecular dynamics study. *FEBS Journal*, 276(11):3060–3075, 2009.

[81] A. M. Brown and D. R. Bevan. Molecular dynamics simulations of amyloid beta-peptide (1-42): tetramer formation and membrane interactions. *Biophysical Journal*, 111(5):937–949, 2016.

[82] X. Yu, Q. Wang, Q. Pan, F. Zhou, and J. Zheng. Molecular interactions of alzheimer amyloid-β oligomers with neutral and negatively charged lipid bilayers. *Physical Chemistry Chemical Physics*, 15(23):8878, 2013.

[83] H. Jang, J. Zheng, and R. Nussinov. Models of beta-amyloid ion channels in the membrane suggest that channel formation in the bilayer is a dynamic process. *Biophysical Journal*, 93(6):1938–1949, 2007.

[84] R. Friedman, R. Pellarin, and A. Caflisch. Amyloid aggregation on lipid bilayers and its impact on membrane permeability. *Journal of Molecular Biology*, 387(2):407 – 415, 2009.

[85] C. Lockhart, A. K. Smith, and D. K. Klimov. Three popular force fields predict consensus mechanism of amyloid β peptide binding to the dimyristoylglycerophosphocholine bilayer. *Journal of Chemical Information and Modeling*, 60(4):2282–2293, 2020.

[86] C. Lockhart and D. K. Klimov. Alzheimer's aβ10–40 peptide binds and penetrates dmpc bilayer: an isobaric–isothermal replica exchange molecular dynamics study. *The Journal of Physical Chemistry B*, 118(10):2638–2648, 2014.

[87] M. Javanainen, A. Melcrová, A. Magarkar, P. Jurkiewicz, M. Hof, P. Jungwirth, and H. Martinez-Seara. Two cations, two mechanisms: interactions of sodium and calcium with zwitterionic lipid membranes. *Chemical Communications*, 53(39):5380–5383, 2017.

[88] A. Catte, M. Girych, M. Javanainen, C. Loison, J. Melcr, M. S. Miettinen, L. Monticelli, J. Määttä, V. S. Oganesyan, O. H. S. Ollila, and et al. Molecular electrometer and binding of cations to phospholipid bilayers. *Physical Chemistry Chemical Physics*, 18(47):32560–32569, 2016.

[89] C. J. Bowerman and B. L. Nilsson. A reductive trigger for peptide self-assembly and hydrogelation. *Journal of the American Chemical Society*, 132(28):9526–9527, 2010.

[90] D. M. Marini, W. Hwang, D. A. Lauffenburger, S. Zhang, and R. D. Kamm. Left-handed helical ribbon intermediates in the self-assembly of a β-sheet peptide. *Nano Letters*, 2(4):295–299, 2002.

[91] J. Lee, X. Cheng, J. M. Swails, M. S. Yeom, P. K. Eastman, J. A. Lemkul, S. Wei, J. Buckner, J. C. Jeong, Y. Qi, and et al. Charmm-gui input generator for namd, gromacs, amber, openmm, and charmm/openmm simulations using the charmm36 additive force field. *Journal of Chemical Theory and Computation*, 12(1):405–413, 2015.

[92] S. Jo, J. B. Lim, J. B. Klauda, and W. Im. Charmm-gui membrane builder for mixed bilayers and its application to yeast membranes. *Biophysical Journal*, 97(1):50–58, 2009.

[93] S. Jo, T. Kim, V. G. Iyer, and W. Im. Charmm-gui: a web-based graphical user interface for charmm. *Journal of Computational Chemistry*, 29(11):1859–1865, 2008.

[94] M. J. Abraham, T. Murtola, R. Schulz, S. Páll, J. C. Smith, B. Hess, and E. Lindahl. Gromacs: High performance molecular simulations through multi-level parallelism from laptops to supercomputers. *SoftwareX*, 1:19–25, 2015.

[95] J. B. Klauda, R. M. Venable, J. A. Freites, J. W. O'Connor, D. J. Tobias, C. Mondragon-Ramirez, I. Vorobyov, A. D. MacKerell, and R. W. Pastor. Update of the charmm all-atom additive force field for lipids: validation on six lipid types. *The Journal of Physical Chemistry B*, 114(23):7830–7843, 2010.

[96] S. Nosé. A unified formulation of the constant temperature molecular dynamics methods. *The Journal of Chemical Physics*, 81(1):511–519, 1984.

[97] M. Parrinello and A. Rahman. Polymorphic transitions in single crystals: a new molecular dynamics method. *Journal of Applied Physics*, 52(12):7182–7190, 1981.

[98] T. Darden, D. York, and L. Pedersen. Particle mesh ewald: an nlog(n) method for ewald sums in large systems. *The Journal of Chemical Physics*, 98(12):10089–10092, 1993.

[99] M. Kohagen, P. E. Mason, and P. Jungwirth. Accurate description of calcium solvation in concentrated aqueous solutions. *The Journal of Physical Chemistry B*, 118(28):7902–7909, 2014.

[100] K. Han, R. M. Venable, A.-M. Bryant, C. J. Legacy, R. Shen, H. Li, B. Roux, A. Gericke, and R. W. Pastor. Graph–theoretic analysis of monomethyl phosphate clustering in ionic solutions. *The Journal of Physical Chemistry B*, 122(4):1484–1494, 2018.

[101] C. M. Ernst and A. Peschel. Broad-spectrum antimicrobial peptide resistance by mprf-mediated aminoacylation and flipping of phospholipids. *Molecular Microbiology*, 80(2):290–299, 2011.

[102] P. Park, L. R. Franco, H. Chaimovich, K. Coutinho, I. M. Cuccovia, and F. S. Lima. Binding and flip as initial steps for bp-100 antimicrobial actions. *Scientific Reports*, 9(1):1–14, 2019.

[103] J. Parkash, M. A. Chaudhry, A. S. Amer, S. Christakos, and W. B. Rhoten. Intracellular calcium ion response to glucose in β-cells of calbindin-d_{28k} nullmutant mice and in βHC13 cells overexpressing calbindin-d_{28k}. *Endocrine*, 18(3):221–230, 2002.

[104] J. E. Hall and M. D. Cahalan. Calcium-induced inactivation of alamethicin in asymmetric lipid bilayers. *Journal of General Physiology*, 79(3):387–409, 1982.

[105] F. Gambale, A. Menini, and G. Rauch. Effects of calcium on the gramicidin a single channel in phosphatidylserine membranes. *European Biophysics Journal*, 14(6):369–374, 1987.

[106] C. F. E. Schroer, L. Baldauf, L. van Buren, T. A. Wassenaar, M. N. Melo, G. H. Koenderink, and S. J. Marrink. Charge-dependent interactions of monomeric and filamentous actin with lipid bilayers. *Proceedings of the National Academy of Sciences*, 117(11):5861–5872, 2020.

[107] M. F. Sciacca, F. Lolicato, C. Tempra, F. Scollo, B. R. Sahoo, M. D. Watson, S. García-Viñuales, D. Milardi, A. Raudino, J. C. Lee, A. Ramamoorthy, and C. La Rosa. Lipid-chaperone hypothesis: a common molecular mechanism of membrane disruption by intrinsically disordered proteins. *ACS Chemical Neuroscience*, 11(24):4336–4350, 2020.

[108] C. Julien, C. Tomberlin, C. M. Roberts, A. Akram, G. H. Stein, M. A. Silverman, and C. D. Link. In vivo induction of membrane damage by β-amyloid peptide oligomers. *Acta neuropathologica communications*, 6(1):131, 2018.

[109] M. Zasloff. Antimicrobial peptides of multicellular organisms. *Nature*, 415(6870):389–395, 2002.

[110] M. Magana, M. Pushpanathan, A. L. Santos, L. Leanse, M. Fernandez, A. Ioannidis, M. A. Giulianotti, Y. Apidianakis, S. Bradfute, A. L. Ferguson et al. The value of antimicrobial peptides in the age of resistance. *The Lancet Infectious Diseases*, 20(9):e216–e230, 2020.

[111] C. D. Fjell, J. A. Hiss, R. E. Hancock, and G. Schneider. Designing antimicrobial peptides: form follows function. *Nature Reviews Drug Discovery*, 11(1):37–51, 2012.

[112] M. López de la Paz, K. Goldie, J. Zurdo, E. Lacroix, C. M. Dobson, A. Hoenger, and L. Serrano. De novo designed peptide-based amyloid fibrils. *Proceedings of the National Academy of Sciences*, 99(25):16052–16057, 2002.

[113] L. Tjernberg, W. Hosia, N. Bark, J. Thyberg, and J. Johansson. Charge attraction and β propensity are necessary for amyloid fibril formation from tetrapeptides. *Journal of Biological Chemistry*, 277(45):43243–43246, 2002.

[114] Y. Yang, S. Jalali, B. L. Nilsson, and C. L. Dias. Binding mechanisms of amyloid-like peptides to lipid bilayers and effects of divalent cations. *ACS Chemical Neuroscience*, 12(11):2027–2035, 2021.

[115] S. Ciudad, E. Puig, T. Botzanowski, M. Meigooni, A. S. Arango, J. Do, M. Mayzel, M. Bayoumi, S. Chaignepain, G. Maglia et al. Aβ (1-42) tetramer and octamer structures reveal edge conductivity pores as a mechanism for membrane damage. *Nature Communications*, 11(1):1–14, 2020.

[116] Z. Jiang, A. I. Vasil, J. D. Hale, R. E. W. Hancock, M. L. Vasil, and R. S. Hodges. Effects of net charge and the number of positively charged residues on the biological activity of amphipathic α-helical cationic antimicrobial peptides. *Biopolymers*, 90(3):369–383, 2007.

[117] J. J. L. Cascales, S. Zenak, J. G. de la Torre, O. G. Lezama, A. Garro, and R. D. Enriz. Small cationic peptides: Influence of charge on their antimicrobial activity. *ACS Omega*, 3(5):5390–5398, 2018.

[118] L. M. Yin, M. A. Edwards, J. Li, C. M. Yip, and C. M. Deber. Roles of hydrophobicity and charge distribution of cationic antimicrobial peptides in peptide-membrane interactions. *Journal of Biological Chemistry*, 287(10):7738–7745, 2012.

[119] L. Ringstad, A. Schmidtchen, and M. Malmsten. Effect of peptide length on the interaction between consensus peptides and DOPC/DOPA bilayers. *Langmuir*, 22(11):5042–5050, 2006.

[120] Y. Huang, J. Huang, and Y. Chen. Alpha-helical cationic antimicrobial peptides: relationships of structure and function. *Protein & Cell*, 1(2):143–152, 2010.

[121] D. G. Lee, H. N. Kim, Y. Park, H. K. Kim, B. H. Choi, C.-H. Choi, and K.-S. Hahm. Design of novel analogue peptides with potent antibiotic activity based on the antimicrobial peptide, HP (2–20), derived from n-terminus of helicobacter pylori ribosomal protein l1. *Biochimica et Biophysica Acta*, 1598(1-2):185–194, 2002.

[122] L. Chen and S. Harrison. Cell-penetrating peptides in drug development: enabling intracellular targets. *Biochemical Society transactions*, 35(4):821–825, 2007.

[123] I. Kustanovich, D. E. Shalev, M. Mikhlin, L. Gaidukov, and A. Mor. Structural requirements for potent cersus selective cytotoxicity for antimicrobial dermaseptin s4 derivatives. *Journal of Biological Chemistry*, 277(19):16941–16951, 2002.

[124] I. Zelezetsky, S. Pacor, U. Pag, N. Papo, Y. Shai, H.-G. Sahl, and A. Tossi. Controlled alteration of the shape and conformational stability of α-helical cell-lytic peptides: effect on mode of action and cell specificity. *Biochemical Journal*, 390(1):177–188, 2005.

[125] M. Dathe, T. Wieprecht, H. Nikolenko, L. Handel, W. Maloy, D. L. MacDonald, M. Beyermann, and M. Bienert. Hydrophobicity, hydrophobic moment and angle subtended by charged residues modulate antibacterial and haemolytic activity of amphipathic helical peptides. *FEBS Letters*, 403(2):208–212, 1997.

[126] T. Zhao, X. Liu, S. Singh, X. Liu, Y. Zhang, J. Sawada, M. Komatsu, and K. D. Belfield. Mitochondria penetrating peptide-conjugated tamra for live-cell long-term tracking. *Bioconjugate Chemistry*, 30(9):2312–2316, 2019.

[127] S. Jalali, Y. Yang, F. Mahmoudinobar, S. M. Singh, B. L. Nilsson, and C. Dias. Using all-atom simulations in explicit solvent to study aggregation of amphipathic peptides into amyloid-like fibrils. *Journal of Molecular Liquids*, 347:118283, 2022.

[128] J. Lee, X. Cheng, J. M. Swails, M. S. Yeom, P. K. Eastman, J. A. Lemkul, S. Wei, J. Buckner, J. C. Jeong, Y. Qi, and et al. Charmm-gui input generator for namd, gromacs, amber, openmm, and charmm/openmm simulations using the charmm36 additive force field. *Journal of Chemical Theory and Computation*, 12(1):405–413, 2016.

[129] M. J. Abraham, T. Murtola, R. Schulz, S. Páll, J. C. Smith, B. Hess, and E. Lindahl. Gromacs: High performance molecular simulations through multi-level parallelism from laptops to supercomputers. *SoftwareX*, 1-2:19 – 25, 2015.

[130] W. C. Wimley and S. H. White. Experimentally determined hydrophobicity scale for proteins at membrane interfaces. *Nature Structural Biology*, 3(10):842–848, 1996.

[131] M. P. Muller, T. Jiang, C. Sun, M. Lihan, S. Pant, P. Mahinthichaichan, A. Trifan, and E. Tajkhorshid. Characterization of lipid–protein interactions and lipid-mediated modulation of membrane protein function through molecular simulation. *Chemical Reviews*, 119(9):6086–6161, 2019.

[132] D. C. Bode, M. Freeley, J. Nield, M. Palma, and J. H. Viles. Amyloid-β oligomers have a profound detergent-like effect on lipid membrane bilayers, imaged by atomic force and electron microscopy. *Journal of Biological Chemistry*, 294(19):7566–7572, 2019.

[133] K. Sasahara, K. Morigaki, and K. Shinya. Effects of membrane interaction and aggregation of amyloid β-peptide on lipid mobility and membrane domain structure. *Physical Chemistry Chemical Physics*, 15(23):8929, 2013.

[134] M. F. M. Engel, L. Khemtemourian, C. C. Kleijer, H. J. D. Meeldijk, J. Jacobs, A. J. Verkleij, B. de Kruijff, J. A. Killian, and J. W. M. Hoppener. Membrane damage by human islet amyloid polypeptide through fibril growth at the membrane. *Proceedings of the National Academy of Sciences*, 105(16):6033–6038, 2008.

[135] N. P. Reynolds, A. Soragni, M. Rabe, D. Verdes, E. Liverani, S. Handschin, R. Riek, and S. Seeger. Mechanism of membrane interaction and disruption by α-synuclein. *Journal of the American Chemical Society*, 133(48):19366–19375, 2011.

[136] N. Arispe, E. Rojas, and H. B. Pollard. Alzheimer disease amyloid β protein forms calcium channels in bilayer membranes: blockade by tromethamine and aluminum. *Proceedings of the National Academy of Sciences*, 90(2):567–571, 1993.

[137] N. Arispe, H. B. Pollard, and E. Rojas. β-amyloid ca^{2+}-channel hypothesis for neuronal death in alzheimer disease. *Molecular and Cellular Biochemistry*, 140(2):119–125, 1994.

[138] N. Arispe, H. B. Pollard, and E. Rojas. Giant multilevel cation channels formed by alzheimer disease amyloid beta-protein [a beta p-(1-40)] in bilayer membranes. *Proceedings of the National Academy of Sciences*, 90(22):10573–10577, 1993.

[139] R. Lipkin and T. Lazaridis. Computational studies of peptide-induced membrane pore formation. *Philosophical Transactions of the Royal Society B: Biological Sciences*, 372(1726):20160219, 2017.

[140] M. Gao and R. Winter. The effects of lipid membranes, crowding and osmolytes on the aggregation, and fibrillation propensity of human IAPP. *Journal of Diabetes Research*, 2015:1–21, 2015.

[141] A. K. Pearce and R. K. O'Reilly. Polymers for biomedical applications: the importance of hydrophobicity in directing biological interactions and application efficacy. *Biomacromolecules*, 22(11):4459–4469, 2021.

[142] Z. Li, A. K. Pearce, J. Du, A. P. Dove, and R. K. O'Reilly. Uniform antibacterial cylindrical nanoparticles for enhancing the strength of nanocomposite hydrogels. *Journal of Polymer Science*, 1, 2022.

[143] C. H. Chen, M. C. Melo, N. Berglund, A. Khan, C. de la Fuente-Nunez, J. P. Ulmschneider, and M. B. Ulmschneider. Understanding and modelling the interactions of peptides with membranes: from partitioning to self-assembly. *Current Opinion in Structural Biology*, 61:160–166, 2020.

[144] S. K. Upadhyay, Y. Wang, T. Zhao, and J. P. Ulmschneider. Insights from microsecond atomistic simulations of melittin in thin lipid bilayers. *The Journal of Membrane Biology*, 248(3):497–503, 2015.

[145] Y. Wang, C. H. Chen, D. Hu, M. B. Ulmschneider, and J. P. Ulmschneider. Spontaneous formation of structurally diverse membrane channel architectures from a single antimicrobial peptide. *Nature Communication*, 7(1):1–9, 2016.

[146] B. S. Perrin Jr, R. Fu, M. L. Cotten, and R. W. Pastor. Simulations of membrane-disrupting peptides ii: Amp piscidin 1 favors surface defects over pores. *Biophysical Journal*, 111(6):1258–1266, 2016.

[147] H. Fatafta, M. Khaled, M. C. Owen, A. Sayyed-Ahmad, and B. Strodel. Amyloid-β peptide dimers undergo a random coil to β-sheet transition in the aqueous phase but not at the neuronal membrane. *Proceedings of the National Academy of Sciences*, 118(39), 2021.

[148] S. Banerjee, M. Hashemi, K. Zagorski, and Y. L. Lyubchenko. Cholesterol in membranes facilitates aggregation of amyloid β protein at physiologically relevant concentrations. *ACS Chemical Neuroscience*, 12(3):506–516, 2021.

[149] A. M. Brown and D. R. Bevan. Molecular dynamics simulations of amyloid β-peptide (1-42): Tetramer formation and membrane interactions. *Biophysical Journal*, 111(5):937–949, 2016.

[150] I. Ermilova and A. P. Lyubartsev. Modelling of interactions between aβ (25–35) peptide and phospholipid bilayers: effects of cholesterol and lipid saturation. *RSC Advances*, 10(7):3902–3915, 2020.

[151] R. Lipkin, A. Pino-Angeles, and T. Lazaridis. Transmembrane pore structures of β-hairpin antimicrobial peptides by all-atom simulations. *The Journal of Physical Chemistry B*, 121(39):9126–9140, 2017.

[152] L. Connelly, H. Jang, F. Teran Arce, R. Capone, S. A. Kotler, S. Ramachandran, B. L. Kagan, R. Nussinov, and R. Lal. Atomic force microscopy and md simulations reveal pore-like structures of all-d-enantiomer of alzheimer's β-amyloid peptide: relevance to the ion channel mechanism of ad pathology. *The Journal of Physical Chemistry B*, 116(5):1728–1735, 2012.

[153] L. Connelly, H. Jang, F. Teran Arce, S. Ramachandran, B. L. Kagan, R. Nussinov, and R. Lal. Effects of point substitutions on the structure of toxic alzheimer's β-amyloid channels: atomic force microscopy and molecular dynamics simulations. *Biochemistry*, 51(14):3031–3038, 2012.

[154] A. Quist, I. Doudevski, H. Lin, R. Azimova, D. Ng, B. Frangione, B. Kagan, J. Ghiso, and R. Lal. Amyloid ion channels: a common structural link for protein-misfolding disease. *Proceedings of the National Academy of Sciences*, 102(30):10427–10432, 2005.

[155] X. Dong, Q. Qiao, Z. Qian, and G. Wei. Recent computational studies of membrane interaction and disruption of human islet amyloid polypeptide: Monomers, oligomers and protofibrils. *Biochimica et Biophysica Acta - Biomembranes*, 1860(9):1826–1839, 2018.

[156] D. Sun, J. Forsman, and C. E. Woodward. Molecular simulations of melittin-induced membrane pores. *The Journal of Physical Chemistry B*, 121(44):10209–10214, 2017.

[157] A. Pino-Angeles and T. Lazaridis. Effects of peptide charge, orientation, and concentration on melittin transmembrane pores. *Biophysical Journal*, 114(12):2865–2874, 2018.

[158] S. T. Ngo, H. M. Hung, K. N. Tran, and M. T. Nguyen. Replica exchange molecular dynamics study of the amyloid beta (11-40) trimer penetrating a membrane. *RSC Advances*, 7(12):7346–7357, 2017.

[159] J. M. Leveritt III, A. Pino-Angeles, and T. Lazaridis. The structure of a melittin-stabilized pore. *Biophysical Journal*, 108(10):2424–2426, 2015.

[160] M. Mihajlovic and T. Lazaridis. Antimicrobial peptides in toroidal and cylindrical pores. *Biochimica et Biophysica Acta - Biomembranes*, 1798(8):1485–1493, 2010.

[161] A. Pino-Angeles, J. M. Leveritt III, and T. Lazaridis. Pore structure and synergy in antimicrobial peptides of the magainin family. *PLoS Computational Biology*, 12(1):e1004570, 2016.

[162] M. Mihailescu, M. Sorci, J. Seckute, V. I. Silin, J. Hammer, B. S. Perrin Jr, J. I. Hernandez, N. Smajic, A. Shrestha, K. A. Bogardus et al. Structure and function in antimicrobial piscidins: histidine position, directionality of membrane insertion, and ph-dependent permeabilization. *Journal of the American Chemical Society*, 141(25):9837–9853, 2019.

[163] H. D. Herce and A. E. Garcia. Molecular dynamics simulations suggest a mechanism for translocation of the hiv-1 tat peptide across lipid membranes. *Proceedings of the National Academy of Sciences*, 104(52):20805–20810, 2007.

[164] H. Leontiadou, A. E. Mark, and S. J. Marrink. Antimicrobial peptides in action. *Journal of the American Chemical Society*, 128(37):12156–12161, 2006.

[165] H. Jang, F. T. Arce, S. Ramachandran, R. Capone, R. Azimova, B. L. Kagan, R. Nussinov, and R. Lal. Truncated β-amyloid peptide channels provide an alternative mechanism for alzheimer's disease and down syndrome. *Proceedings of the National Academy of Sciences*, 107(14):6538–6543, 2010.

[166] H. Jang, L. Connelly, F. Teran Arce, S. Ramachandran, B. L. Kagan, R. Lal, and R. Nussinov. Mechanisms for the insertion of toxic, fibril-like β-amyloid oligomers into the membrane. *Journal of Chemical Theory and Computation*, 9(1):822–833, 2012.

[167] Z. Chang, Y. Luo, Y. Zhang, and G. Wei. Interactions of aβ25- 35 β-barrel-like oligomers with anionic lipid bilayer and resulting membrane leakage: an all-atom molecular dynamics study. *The Journal of Physical Chemistry B*, 115(5):1165–1174, 2011.

[168] K. Gupta, H. Jang, K. Harlen, A. Puri, R. Nussinov, J. P. Schneider, and R. Blumenthal. Mechanism of membrane permeation induced by synthetic β-hairpin peptides. *Biophysical Journal*, 105(9):2093–2103, 2013.

[169] J. Vargas, J. Alarcón, and E. Rojas. Displacement currents associated with the insertion of alzheimer disease amyloid β-peptide into planar bilayer membranes. *Biophysical Journal*, 79(2):934–944, 2000.

[170] T. L. Lau, E. E. Ambroggio, D. J. Tew, R. Cappai, C. L. Masters, G. D. Fidelio, K. J. Barnham, and F. Separovic. Amyloid-beta peptide disruption of lipid membranes and the effect of metal ions. *Journal of Molecular Biology*, 356(3):759–770, 2006.

[171] F. Wang, O. Gnewou, S. Wang, T. Osinski, X. Zuo, E. H. Egelman, and V. P. Conticello. Deterministic chaos in the self-assembly of β sheet nanotubes from an amphipathic oligopeptide. *Matter*, 4(10):3217–3231, 2021.

[172] R. N. Lewis, Y.-P. Zhang, and R. N. McElhaney. Calorimetric and spectroscopic studies of the phase behavior and organization of lipid bilayer model membranes composed of binary mixtures of dimyristoylphosphatidylcholine and dimyristoylphosphatidylglycerol. *Biochimica et Biophysica Acta - Biomembranes*, 1668(2):203–214, 2005.

[173] R. Oliva, M. Chino, K. Pane, V. Pistorio, A. D. Santis, E. Pizzo, G. D'Errico, V. Pavone, A. Lombardi, P. D. Vecchio, E. Notomista, F. Nastri, and L. Petraccone. Exploring the role of unnatural amino acids in antimicrobial peptides. *Scientific Reports*, 8(1):8888, 2018.

[174] P. M. Macdonald and J. Seelig. Calcium binding to mixed phosphatidylglycerol-phosphatidylcholine bilayers as studied by deuterium nuclear magnetic resonance. *Biochemistry*, 26(5):1231–1240, 1987.

[175] D. E. Shaw, J. Grossman, J. A. Bank, B. Batson, J. A. Butts, J. C. Chao, M. M. Deneroff, R. O. Dror, A. Even, C. H. Fenton, A. Forte, J. Gagliardo, G. Gill, B. Greskamp, C. R. Ho, D. J. Ierardi, L. Iserovich, J. S. Kuskin, R. H. Larson, T. Layman, L.-S. Lee, A. K. Lerer, C. Li, D. Killebrew, K. M. Mackenzie, S. Y.-H. Mok, M. A. Moraes, R. Mueller, L. J. Nociolo, J. L. Peticolas, T. Quan, D. Ramot, J. K. Salmon, D. P. Scarpazza, U. B. Schafer, N. Siddique, C. W. Snyder, J. Spengler, P. T. P. Tang, M. Theobald, H. Toma, B. Towles, B. Vitale, S. C. Wang, and C. Young. Anton 2: raising the bar for performance and programmability in a special-purpose molecular dynamics supercomputer. *SC'14: Proceedings of the International Conference for High Performance Computing, Networking, Storage and Analysis*, 41–53, 2014.

[176] D. Frishman and P. Argos. Knowledge-based protein secondary structure assignment. *Proteins*, 23(4):566–579, 1995.

[177] C. Narayanan and C. L. Dias. Hydrophobic interactions and hydrogen bonds in β-sheet formation. *The Journal of Chemical Physics*, 139(11):09B640_1, 2013.

[178] Z. Su and C. L. Dias. Driving β-strands into fibrils. *The Journal of Physical Chemistry B*, 118(37):10830–10836, 2014.

[179] J. Seelig. Deuterium magnetic resonance: theory and application to lipid membranes. *Quarterly Reviews of Biophysics*, 10(3):353–418, 1977.

[180] P.-L. Chau and A. J. Hardwick. A new order parameter for tetrahedral configurations. *Molecular Physics*, 93(3):511–518, 1998.

[181] A. Hung and I. Yarovsky. Inhibition of peptide aggregation by lipids: insights from coarse-grained molecular simulations. *Journal of Molecular Graphics and Modelling*, 29(5):597–607, 2011.

[182] B. E. Brummel, A. R. Braun, and J. N. Sachs. Polyunsaturated chains in asymmetric lipids disorder raft mixtures and preferentially associate with α-synuclein. *Biochimica et Biophysica Acta - Biomembranes*, 1859(4):529–536, 2017.

[183] F. M. LaFerla, K. N. Green, and S. Oddo. Intracellular amyloid-β in alzheimer's disease. *Nature Reviews Neuroscience*, 8(7):499–509, 2007.

[184] K. A. Gyure, R. Durham, W. F. Stewart, J. E. Smialek, and J. C. Troncoso. Intraneuronal aβ-amyloid precedes development of amyloid plaques in down syndrome. *The Archives of Pathology & Laboratory Medicine*, 125(4):489–492, 2001.

[185] G. K. Gouras, J. Tsai, J. Naslund, B. Vincent, M. Edgar, F. Checler, J. P. Greenfield, V. Haroutunian, J. D. Buxbaum, H. Xu, P. Greengard, and N. R. Relkin. Intraneuronal aβ42 accumulation in human brain. *The American Journal of Pathology*, 156(1):15–20, 2000.

[186] S. Grudzielanek, V. Smirnovas, and R. Winter. The effects of various membrane physical–chemical properties on the aggregation kinetics of insulin. *Chemistry and Physics of Lipids*, 149(1):28–39, 2007.

[187] C. Morris, S. Cupples, T. W. Kent, E. A. Elbassal, E. P. Wojcikiewicz, P. Yi, and D. Du. N-terminal charged residues of amyloid-β peptide modulate amyloidogenesis and interaction with lipid membrane. *Chemistry – A European Journal*, 24(38):9494–9498, 2018.